NONLINEAR SUPPRESSION OF RANGE AMBIGUITY IN PULSE DOPPLER RADAR

DISSERTATION

Jon M. Anderson, Major, USAF

AFIT/DS/ENG/01-05

DEPARTMENT OF THE AIR FORCE
AIR UNIVERSITY

AIR FORCE INSTITUTE OF TECHNOLOGY

Wright-Patterson Air Force Base, Ohio

Report Documentation Page

Report Date 13 Dec 2001	**Report Type** Final	**Dates Covered (from... to)** -

Title and Subtitle Nonlinear Suppression of Range Ambiguity in Pulse Doppler Radar	**Contract Number**
	Grant Number
	Program Element Number
Author(s) Major Jon M. Anderson, USAF	**Project Number**
	Task Number
	Work Unit Number
Performing Organization Name(s) and Address(es) Air Force Institute of Technology Graduate School of Engineering and Management (AFIT/EN)	**Performing Organization Report Number** AFIT/DS/ENG/01-05
Sponsoring/Monitoring Agency Name(s) and Address(es) AFRL/SN ATTN: Dr. William M. Brown Wright-Patterrson AFB, OH 45433	**Sponsor/Monitor’s Acronym(s)**
	Sponsor/Monitor’s Report Number(s)
Distribution/Availability Statement Approved for public release, distribution unlimited	
Supplementary Notes	

Abstract

Coherent pulse train processing is most commonly used in airborne pulse Doppler radar, achieving adequate transmitter/receiver isolation and excellent resolution properties while inherently inducing ambiguities in Doppler and range. First introduced by Palermo in 1962 using two conjugate LFM pulses, the primary nonlinear suppression objective involves reducing range ambiguity, given the waveform is nominally unambiguous in Doppler, by using interpulse and intrapulse coding (pulse compression) to discriminate received ambiguous pulse responses. By introducing a nonlinear operation on compressed (undesired) pulse responses within individual channels, ambiguous energy levels are reduced in channel outputs. This research expands the NLS concept using discrete coding and processing. A general theory is developed showing how NLS accomplishes ambiguity surface volume removal without requiring orthogonal coding. Useful NLS code sets are generated using combinatorial, simulated annealing optimization techniques - a general algorithm is developed to extended family size, code length, and number of phases (polyphase coding). An adaptive reserved code thresholding scheme is introduced to efficiently and effectively track the matched filter response of a target field over a wide dynamic range, such as normally experienced in airborne radar systems. An evaluation model for characterizing NLS clutter suppression performance is developed - NLS performance is characterized using measured clutter data with analysis indicating the proposed technique performs relatively well even when large clutter cells exist.

Subject Terms

Radar, Pulse Compression, Radar Waveforms, Nonlinear Signal Processing, Radar Signal Processing, Radar Coding

Report Classification unclassified	**Classification of this page** unclassified
Classification of Abstract unclassified	**Limitation of Abstract** UU

Number of Pages

146

AFIT/DS/ENG/01-05

NONLINEAR SUPPRESSION OF RANGE AMBIGUITY IN PULSE DOPPLER RADAR

DISSERTATION

Presented to the Faculty
Graduate School of Engineering and Management
Air Force Institute of Technology
Air University
Air Education and Training Command
in Partial Fulfillment of the Requirements for the
Degree of Doctor of Philosophy

Jon M. Anderson, B.S.E.E., M.S.E.E.
Major, USAF

December 2001

APPROVED FOR PUBLIC RELEASE; DISTRIBUTION UNLIMITED.

AFIT/DS/ENG/01-05

NONLINEAR SUPPRESSION OF RANGE AMBIGUITY IN PULSE DOPPLER RADAR

Jon M. Anderson, B.S.E.E., M.S.E.E.
Major, USAF

Approved:

	Date
Michael A. Temple (Chairman)	5 Dec 01
Glen P. Perram (Dean's Representative)	5 Dec 01
William M. Brown (Member)	Dec 3, 2001
M. Pachter Meir Pachter (Member)	Dec 3, 2001
Mark E. Oxley Mark E. Oxley (Member)	Dec 3, 2001

Accepted:

6 Dec, 2001

Robert A. Calico, Jr. Date
Dean, Graduate School of Engineering and Management

Acknowledgements

I am in great debt to Dr. Michael Temple, my research advisor, who labored hard for two years to ensure I would accomplish my research goals. Special thanks go to Dr. William Brown, who introduced me to NLS and provided brilliant insights throughout. Dr. Mark Oxley and Dr. Meir Pachter also spent many hours helping me tackle theoretical issues, and I thank them as well. Thanks to Capt Todd Hale and Maj Jeff Hebert, fellow students, who both provided help at crucial times. Thanks to Dr. John Betts and Col Neal McCasland, who gave me important advise prior to starting my doctoral program.

This is the third time in almost two decades that the United States Air Force has provided an education – and I am deeply grateful.

I would never have attempted or finished a doctoral program without the support and love of my wife and children. Finally, many prayers were answered during the course of this research. Thanks to God for those many leaps of intuition that arrived when all seemed hopeless.

Table of Contents

List of Figures

List of Tables

Abstract

Coherent pulse train processing is most commonly used in airborne pulse Doppler radar, achieving adequate transmitter/receiver isolation and excellent resolution properties while inherently inducing ambiguities in both Doppler and range. As first introduced by Palermo in 1962 using two conjugate LFM pulses, the primary nonlinear suppression (NLS) objective involves reducing range ambiguity, given the waveform is nominally unambiguous in Doppler, by using interpulse and intrapulse coding (pulse compression) to discriminate the received ambiguous pulse responses. By introducing a nonlinear operation on compressed (undesired) pulse responses within individual channels, ambiguous energy levels are reduced in channel outputs. The proliferation of high-speed digital signal processing capability and discrete code development occurring since 1962, greatly improves the feasibility of implementing NLS using code sets of multiple codes. This research expands the NLS concept using discrete coding and processing. A general theory is developed showing how NLS accomplishes ambiguity surface volume removal without requiring orthogonal coding. Useful NLS code sets are generated using combinatorial, simulated annealing optimization techniques – a general algorithm is developed to extended family size, code length, and number of phases (polyphase coding). An adaptive reserved code thresholding scheme is introduced to efficiently and effectively track the matched filter response of a target field over a wide dynamic range, such as normally experienced in airborne radar systems. An evaluation model for characterizing NLS clutter suppression performance is developed – NLS performance is characterized using measured clutter data with analysis indicating the proposed technique performs relatively well even when large clutter cells exist.

NONLINEAR SUPPRESSION OF RANGE AMBIGUITY IN PULSE DOPPLER RADAR

1. Introduction

1.1 Radar Waveforms and Doppler/Range Ambiguity

Radar technology is broadly applied to many diverse applications, including everything from air traffic control, to ground mapping, to vehicular collision avoidance. The primary focus of this research is airborne pulse Doppler radar. The basic function of modern airborne radar systems is to detect targets of interest while estimating each target's position and velocity. Target characterization may be considered a four-dimensional problem, i.e., it includes the parametric estimation/measurement of four key parameters, including, range, velocity, azimuth angle, and elevation angle. Estimation and/or measurement accuracy of the spacial location angles is primarily determined by radar antenna characteristics. Range and velocity determination is primarily dependent upon the estimation/measurement accuracy of time delay and Doppler frequency, respectively. Time delay and Doppler frequency measurements are intimately related to fundamental radar waveform properties and are essentially independent of angular measurements [1:209]. Therefore, in the analysis of range and velocity measurements the angular dimensions are often conveniently ignored.

Perhaps the simplest radar waveform is the continuous wave (CW) waveform. In this case, the transmitter typically broadcasts a continuous sinusoid while receiving target and environmental returns on a separate receive antenna. The primary advantage of CW radar is unambiguous Doppler measurement, i.e., each target velocity produces a single unique Doppler frequency shift of the CW carrier. Thus, unambiguous Doppler measurement permits reliable target separation based solely on Doppler frequency. However, in CW radar target range measurements are entirely ambiguous, i.e., the continuous nature of the radar waveform does not permit accurate estimation of unique range information. If initial range is known, the radar may track range based on range-rate. However, initial range information is usually not available. Another CW radar disadvantage, perhaps even greater than the ambiguous range problem, is the need for separate transmit/receive antennas and problems associated with preventing transmitter leakage into the receiver. This normally prevents the use of CW radar on airborne platforms due to the increased size and weight associated with having multiple antennas.

Most modern radars employ a pulsed waveform. The primary advantage of pulsed radar over CW is that pulsing allows the transmitter and receiver to share the same antenna. Figure 1-1 illustrates the parameters associated with a typical pulsed radar waveform. The pulse duration, or *pulse width* (PW), is denoted as T_p and the *pulse repetition interval* (PRI) is denoted as T_r. From these fundamental waveform parameters, several other important parameters are derived.

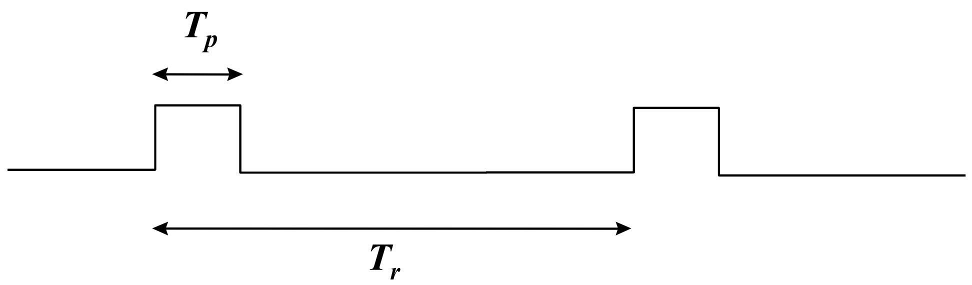

Figure 1-1. Fundamental Pulsed Radar Waveform Parameters

The *pulse repetition frequency* (PRF), denoted as f_r, is the inverse of the PRI

$$f_r = \frac{1}{T_r} \quad . \tag{1.1}$$

Pulsed radar waveforms are normally classified as Low-PRF, Medium-PRF, or High-PRF due to PRF impact on range and Doppler ambiguity. The waveform *duty factor*, denoted as d, is the ratio of PW to PRI

$$d = \frac{T_p}{T_r} \quad . \tag{1.2}$$

The *unambiguous range*, denoted as R_u, is the maximum two-way range that a pulse can travel before the next pulse is transmitted, and is dependent upon c, the speed of light.

$$R_u = \frac{c\,T_r}{2} \quad . \tag{1.3}$$

Figure 1-2 illustrates the relationship of unambiguous range to PRI. This scenario consists of two fixed targets, one unambiguous at a range $R_u/2$ and one ambiguous at range $R_u + 0.7R_u$. Identical radar pulses are transmitted every T_r seconds. Within the first PRI processing interval following pulse one transmission, only the return from Target 1 is received and its range is unambiguously determined. Within the second PRI processing interval, another return from Target 1, due to the second transmitted pulse, is received with exactly the same time delay as measured during the first PRI. Shortly thereafter within the second PRI processing interval, a return from Target 2 due to the first transmitted pulse is received. In this case, the apparent (erroneous/ambiguous) range of Target 2 is 0.7 R_u as determined during the second PRI. For this basic pulsed radar waveform having no intra- or interpulse coding, there is no means for the radar to effective resolve the range ambiguity.

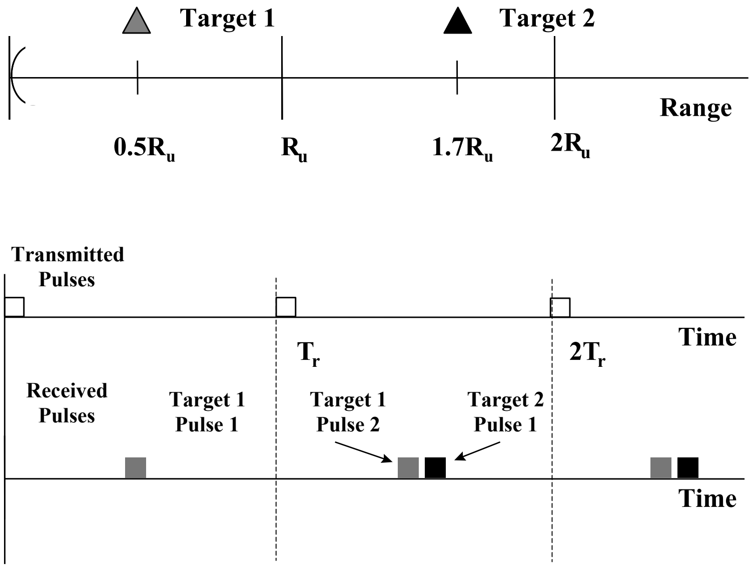

Figure 1-2. Impact of Pulse Repetition on Range Ambiguities

Low-PRF waveforms are commonly designed such that R_u exceeds the maximum detectable radar range, as determined by factors such as the transmitted power, antenna gain, and receiver sensitivity. The penalty incurred for achieving unambiguous range operation is a low duty cycle (corresponding to lower average power) and ambiguous Doppler. The lower average power may be mitigated by raising the peak transmitter power, often a more practical solution for ground-based systems than airborne radars. The Doppler ambiguity arises from the sampling nature of pulsed radars. The carrier frequency *Doppler shift*, denoted as f_d, as induced by a target having velocity v relative to the target

$$f_d = \frac{2v}{\lambda} \tag{1.4}$$

where λ is the carrier wavelength. For moving targets, the differential phase change between successive pulses, denoted as $\Delta\phi$, is given by

$$\Delta\phi = 2\pi\left(\frac{2\Delta R}{\lambda}\right) \tag{1.5}$$

where ΔR is the change in target range between successive pulses. When the phase change between pulses exceeds 2π, the Doppler measurement becomes ambiguous [2].

Clearly, the higher the radar PRF becomes the greater the range ambiguity. Note that as the radar PRF increases, the waveform approaches a CW signal and range becomes entirely ambiguous. However, high PRF radar waveforms are normally employed to ensure targets of interest are separable from clutter in the Doppler domain. This is normally required for airborne radar applications where the clutter return is spread in both Doppler and range.

Table 1-1. Summary of Waveform Ambiguity Relationships

	Low PRF	**Medium PRF**	**High PRF**	**CW**
Range	Unambiguous	Ambiguous	Ambiguous	Ambiguous
Doppler	Ambiguous	Ambiguous	Unambiguous	Unambiguous

Table 1-1 summarizes various range/Doppler ambiguity relationships. The actual PRF value that determines whether a waveform is classified as Low-, Medium- or High-PRF depends on the targets of interest, the carrier wavelength, the detectable range, and the nature of the clutter.

The most common method for resolving range and Doppler ambiguities involves using multiple PRFs. This has the effect of changing the apparent target range estimated by each pulse, or pulse burst, and allows for some ambiguity resolution in either Doppler or range, depending on the particular application.

1.2 Radar Waveform Fundamentals

Two important concepts that drive radar waveform design are resolution and the radar uncertainty relation. Resolution may be simply defined as the radar's ability to separate closely spaced targets. Separation may be in time delay, Doppler shift, or both. Resolution is closely related to the "narrowness" of signal characteristics in either the time or frequency domains. The concept of resolution is most easily illustrated with a simple radar pulse as illustrated in Figure 1-3. In this case, the pulse envelope has width T_p in the time domain and its corresponding frequency spectrum is found using Fourier Transform relations of Eq (A.2) and Eq (A.3).

One definition of bandwidth is the main spectral lobe width, which equals $2/T_p$ for the simple radar pulse of Figure 1-3. Thus, increasing pulse width reduces the bandwidth while decreasing pulse width increases the bandwidth. A simple statement of the *Radar Uncertainty Relation* is that the pulse width and bandwidth of a waveform may not be made arbitrarily small simultaneously [3:409].

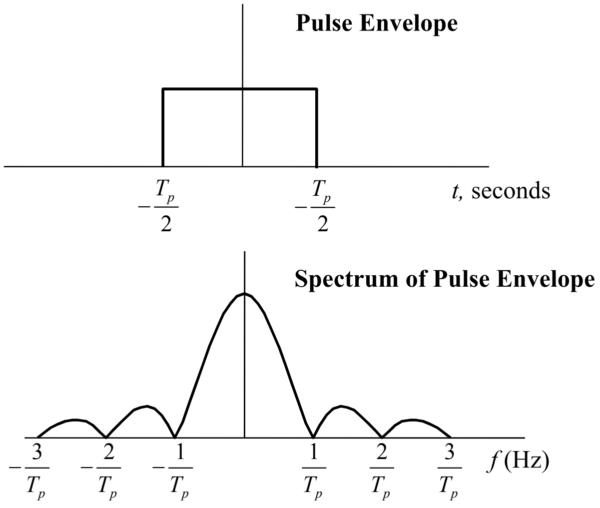

Figure 1-3. Pulse Envelope and its Magnitude Spectrum

The implication of the uncertainty relation is that increased resolution in the time domain results in decreased resolution in the frequency domain, and vice-versa. Range resolution is closely related to pulse width, such that the ability to resolve closely spaced targets in range requires a short pulse. As the pulse width is decreased, the amount of energy in the pulse is also decreased, thus reducing the radar detection range. This is usually overcome by utilizing a technique called *pulse compression*.

Pulse compression involves intentionally modulating a pulse to increase its bandwidth. While the pulse energy of a compressed pulse equals that of an unmodulated long pulse, the waveform resolution becomes that of a short pulse upon reception and demodulation. Many pulse compression modulation techniques may be employed, including, Linear Frequency Modulation (LFM), Binary Phase Shift Keying (BPSK), Frequency Shift Keying (FSK), and Polyphase coding. Traditional pulse compression techniques involve applying identical modulation to each pulse in a pulse train. For this research, *interpulse coding* is used extensively such that each pulse is uniquely modulated.

A coherently transmitted set of N identical pulses may be represented by the complex signal (see Section A.2)

$$\psi_t(t) = \sum_{n=0}^{N-1} A_t\, \mu(t - nT_r)\, e^{j2\pi f_0 t} \tag{1.6}$$

where A_t is a constant amplitude for each pulse, T_r is the pulse repetition period, and f_0 is the carrier frequency. The complex envelope $\mu(t)$ in Eq (1.6) is given by

$$\mu(t) = a(t)\, e^{j\phi(t)} \tag{1.7}$$

where $a(t)$ is the amplitude modulation and ϕ(t) is the phase modulation. The number of pulses N is dependent upon the antenna beam dwell time at a particular azimuth and elevation. The dwell time is normally divided into several coherent processing intervals (CPIs). The output of several CPIs may be noncoherently integrated prior to detection.

Assuming a constant velocity, non-fluctuating point target, the received waveform is given by

$$\psi_r(t) = \sum_{n=0}^{N-1} A_r\, \mu(t - \tau_d - nT_r)\, e^{j2\pi(f_0 + f_d)(t - \tau_d - nT_r)} \tag{1.8}$$

where amplitude A_r is found from the radar range equation, Eq (A.17) , τ_d is the target return time delay (resulting from two-way propagation), and f_d is the relative Doppler shift induced on the return by the target motion.

The pulse modulation function chosen is dependent upon many factors. The amplitude modulation $a(t)$ establishes the pulse envelope shape. Two prominent $a(t)$ examples are shown in Figure 1-4. The rectangular pulse function is given by

$$a(t) = rect\left(\frac{t}{T_p}\right) = \begin{cases} 1 & |t| \le \frac{T_p}{2} \\ 0 & |t| > \frac{T_p}{2} \end{cases} \tag{1.9}$$

where T_p is the pulse width. The Gaussian pulse function is given by

$$a(t) = e^{-\frac{1}{2}\left(\frac{t}{T_p}\right)^2} . \tag{1.10}$$

Pulse amplitude weighting is often used to control specific pulse train characteristics, but it is not considered here.

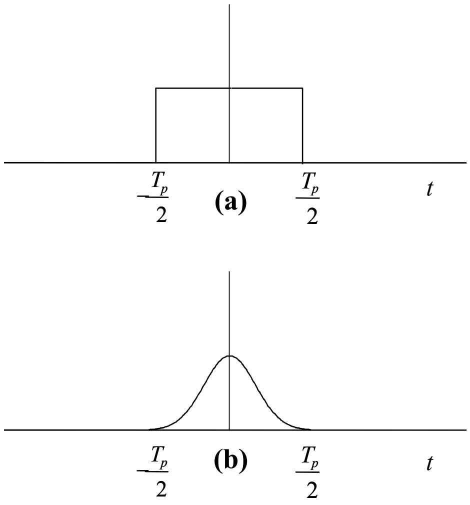

Figure 1-4. Rectangular (a) and Gaussian (b) Pulses

Phase modulation is normally used to perform pulse compression, where a long modulated pulse is transmitted with bandwidth W. Upon reception, the pulse is demodulated to form a shorter pulse having width $1/W$, thus obtaining the energy benefits of a long pulse and the resolution benefits of a short pulse.

Two prominent phase modulations include Linear Frequency Modulation (LFM) and binary phase shift keying (BPSK). For LFM, the phase function $\phi(t)$ is chosen to yield an instantaneous frequency that varies linearly with time.

$$f_{inst}(t) = \frac{d\,\phi(t)}{dt} = \pm bt\,. \tag{1.11}$$

This yields a phase modulation function

$$\phi(t) = bt^2 \tag{1.12}$$

$$\text{or } \phi(t) = -bt^2 \tag{1.13}$$

where b is chosen to obtain the required bandwidth. BPSK modulation is implemented by changing the carrier phase by π using a binary spreading code $c(t)$ with desirable properties:

$$\begin{gathered} \phi(t) = \begin{cases} 0 & c(t) = 1 \\ \pi & c(t) = -1 \end{cases} \\ c(t) = \pm 1\ . \end{gathered} \tag{1.14}$$

Note that spreading modulation $c(t)$ may also be applied to the amplitude modulation term yielding

$$\mu(t) = c(t)\,a(t) \tag{1.15}$$

since a sign change in $c(t)$ results in a phase shift of π. The spreading code $c(t)$ is composed of "chips" of length T_c and generally $T_c << T_p$.

In either case, the goal of pulse modulation is to increase the signal time-bandwidth product (*TB*). There are many ways to define signal time duration and bandwidth. A common method used in signal theory is to employ second moments, as in computing a random variable parameter [20:36] (also known as the radius of gyration [4:141]). This is often useful, since in many cases the time duration and bandwidth are both uncertain parameters.

The *root mean square (rms) signal duration* of $y(t)$, assuming a time origin of $t = 0$, is defined by the second moment of t with respect to the complex signal [20:37]

$$T_{rms}^2 = \frac{(2\pi)^2 \int_{-\infty}^{\infty} t^2 \left|y(t)\right|^2 dt}{\int_{-\infty}^{\infty} \left|y(t)\right|^2 dt}\ . \tag{1.16}$$

Likewise, the *rms bandwidth* of *M(f)* is defined by

$$W_{rms}^{2} = \frac{(2\pi)^2 \int_{-\infty}^{\infty} f^2 \left|M(f)\right|^2 df}{\int_{-\infty}^{\infty} \left|M(f)\right|^2 df} \quad . \tag{1.17}$$

Note that both quantities are normalized with respect to signal energy and that T_{rms} is defined in terms of the complex signal (including carrier), while W_{rms} is sufficiently defined in terms of the complex envelope energy density spectrum *M(f)* found from Eq (A.14).

An important relation between T_{rms} and W_{rms} establishes the lower limit on the time-bandwidth product [20:55] expressed as

$$T_{rms}\, W_{rms} \ \geq \ \pi \tag{1.18}$$

where equality holds when

$$a(t) = -e^{\frac{-k t^2}{2}} \quad . \tag{1.19}$$

Thus, the waveform achieving this lower limit is a constant-carrier Gaussian pulse.

In practice, it is common to approximate the time-bandwidth product by specifying the time duration and bandwidth in terms of pulse width (when the pulse width is known with certainty). In this case

$$W_p \approx \frac{1}{T_p} \Rightarrow W_p\, T_p = 1 \tag{1.20}$$

where W_p is the null-null bandwidth of a rectangular pulse of duration T_p. If the pulse is modulated a new quantity, called *pulse compression ratio* (PCR), is introduced and defined as the ratio of the transmitted pulse width to the compressed pulse width, or

$$PCR = \frac{T_p}{T_c} \quad . \tag{1.21}$$

The *modulation bandwidth* W_c is the null-null bandwidth of a rectangular pulse of duration $\mathrm{T_c}$

$$W_c \approx \frac{1}{T_c} \Rightarrow W_c T_c = 1 \, . \tag{1.22}$$

For modulation bandwidth W_c, where $W_c >> W_p$, the time-bandwidth product of the transmitted waveform may be approximated using

$$TB \approx W_c T_p = \frac{T_p}{T_c} = PCR \, . \tag{1.23}$$

Thus, the modulated pulse has duration T_p, a bandwidth of PCR/T_p, and a time-bandwidth product of PCR, facilitating a range resolution improvement of PCR.

1.3 The Ambiguity Function

The *ambiguity function (AF)* is widely used in radar waveform analysis. It may be defined as the complex-valued correlation between a waveform and a time-delayed, frequency-shifted replica of that waveform [5:1-1]. It may also be defined as the matched-filter response in delay (τ) and Doppler (ν) [3:411] and as a "correlative" time-frequency representation [6]. The ambiguity function $\chi(\tau,\nu)$ is mathematically defined in terms of a waveform's complex envelope (or complex envelope spectrum) $M(f)$ as [20:119]

$$\chi(\tau,\nu) \equiv \int_{-\infty}^{\infty} \mu(t)\,\mu^*(t-\tau)\,e^{j2\pi\nu t}\,dt \tag{1.24}$$

$$\chi(\tau,\nu) \equiv \int_{-\infty}^{\infty} M^*(f)\,M(f-\nu)\,e^{j2\pi f\tau}\,df \, . \tag{1.25}$$

Some authors actually define $|\chi(\tau,\nu)|^2$ as the ambiguity function. However, following [20:112], the term ambiguity function will be applied to the response function in general, with its actual form specified as needed.

The ambiguity function has several important properties. The maximum value of the ambiguity surface occurs at the origin and equals $(2E)^2$ per

$$|\,\chi(\tau,\nu)\,|^2 \le |\,\chi(0,0)\,|^2 = (2E)^2 \tag{1.26}$$

and has a symmetric modulus about the origin expressed as

$$|\,\chi(-\tau,-\nu)\,| = |\,\chi(\tau,\nu)\,| \, . \tag{1.27}$$

Along the delay (τ) axis, $\chi(\tau,\nu)$ represents the autocorrelation function, while along the Doppler (ν) axis, $\chi(\tau,\nu)$ is proportional to the spectrum of μ^2(t)

$$|\chi(\tau,\nu=0)|^2 = \left|\int_{-\infty}^{\infty} \mu(t)\,\mu^*(t-\tau)\,dt\right|^2 \tag{1.28}$$

$$|\chi(\tau=0,\nu)|^2 = \left|\int_{-\infty}^{\infty} |\mu(t)|^2\, e^{j2\pi\nu t}\, dt\right|^2 . \tag{1.29}$$

Finally, the volume V_{amb} under the ambiguity surface is constant and given by

$$V_{amb} = \int_{-\infty}^{\infty}\int_{-\infty}^{\infty} |\chi(\tau,\nu)|^2\, d\tau\, d\nu = |\chi(0,0)|^2 = (2E)^2 . \tag{1.30}$$

The ideal ambiguity function allows resolution of closely spaced targets in both delay and Doppler while inducing minimal "self-clutter", i.e., interference from sidelobes. Thus, the ideal ambiguity function, shown in Figure 1-5, is a two-dimensional Dirac delta function $\delta(\tau,\nu)$ centered at the origin.

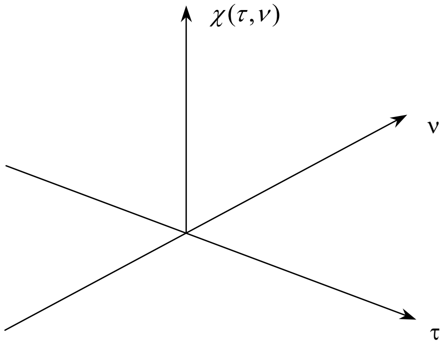

Figure 1-5. Ideal Ambiguity Function

However, the height and volume constraints of the ambiguity function per Eq (1.26) and Eq (1.30) make this ideal form unrealizable. An approximation, known as the "thumbtack" ambiguity surface, is shown Figure 1-6 [3:413]. The thumbtack has a narrow central spike and a low-level pedestal surrounding the spike; the pedestal contains the bulk of the ambiguity volume. Achieving a thumbtack-like ambiguity surface is the primary goal in radar waveform design.

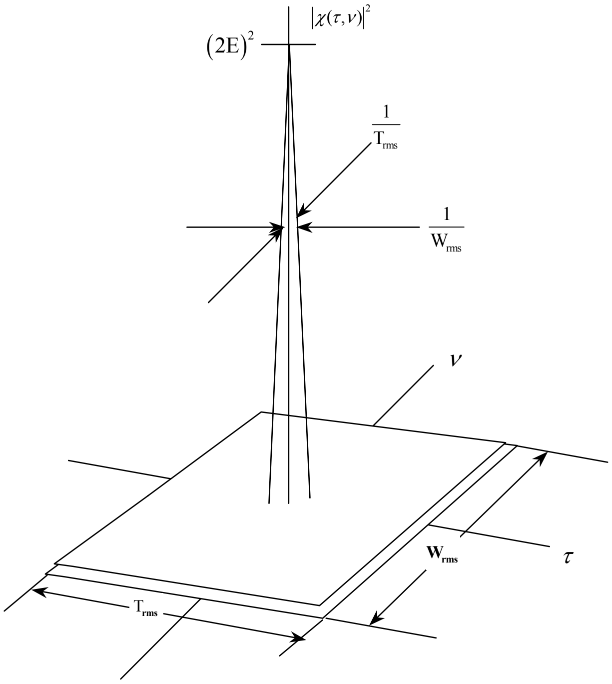

Figure 1-6. Thumbtack Ambiguity Surface

To gain insight into ambiguity function characteristics for a single rectangular, sinusoidal pulse, Figure 1-7 is provided and shows a two-dimensional projection of the ambiguity surface for a long and short pulse. Shaded areas represent the relatively large matched filter responses in the delay-Doppler plane, illustrating ambiguous regions that directly relate to the radar uncertainty relation. In this case, the longer pulse has narrower bandwidth and better Doppler resolution in Doppler while the shorter pulse provides better resolution along the delay axis.

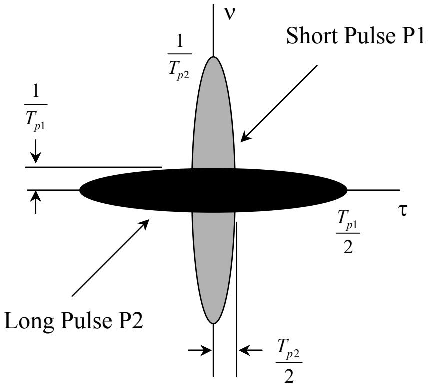

Figure 1-7. AF Projection for Single Unmodulated Pulses

Figure 1-8 shows the ambiguity projection for LFM pulse modulation. The quadratic LFM phase function results in a shearing of the ambiguity function parallel to the delay axis [20:123], i.e., the axis of the ellipse tilts at an angle to both the delay and Doppler axes. This results in Doppler-range cross coupling, which may be resolved using either a priori knowledge of range or Doppler, or multiple LFM modulations [2].

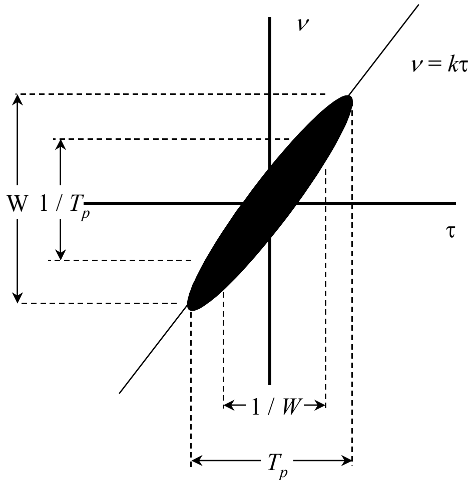

Figure 1-8. AF Projection for Single LFM Pulse Modulation

The most important waveform considered for this research is the coherent pulse train. As stated in Section 1.1, pulse train processing permits use of a long duration signal and provides receiver isolation. The long signal duration is achieved by transmitting a large number of coherent (continuous phase) pulses during each antenna dwell time and coherent processing of the returns. The ambiguity function of a uniform pulse train comprised of *N* pulses is given by [20:290] as

$$\begin{aligned}\chi_{pt}(\tau,\nu) &= \int_{-\infty}^{\infty} s(t)\, s^{*}(t-\tau)\, e^{j2\pi\nu t}\, dt \\ &= \sum_{n=0}^{N-1}\sum_{m=0}^{N-1} e^{j2\pi\nu n T_r}\, \chi_p\left(\tau-\left[n-m\right]T_r\,,\nu\right)\end{aligned} \tag{1.31}$$

which may be rewritten as

$$\chi_{pt}(\tau,\nu) = \frac{1}{N}\sum_{p=-(N-1)}^{N-1} e^{j\pi\nu(N-1+p)T_r}\, \chi_p(t-pT_r,\nu)\frac{\sin\left(\pi\nu\left[N-|p|\right]T_r\right)}{\sin\left(\pi\nu T_r\right)} \tag{1.32}$$

where $\chi_p(\tau,\nu)$ is the ambiguity function of the single pulse and all pulses in the train are identical. Thus, the pulse train ambiguity function consists of a weighted superposition of component signal ambiguity functions translated along the delay axis by multiples of the PRI. The induced range ambiguities due to pulse repetition (πnT_r factor in the above equation) are clearly evident in the resultant ambiguity surface. Along the Doppler axis, the signal effectively stretches (from one pulse to *N* pulses) which produces a narrowing of the central peak width from approximately $1/T_p$ to $1/(NT_r)$ as shown in Figure 1-9. The envelope of the single pulse ambiguity function is the dashed line; the solid line is the zero-delay cut of the uniform pulse train ambiguity surface.

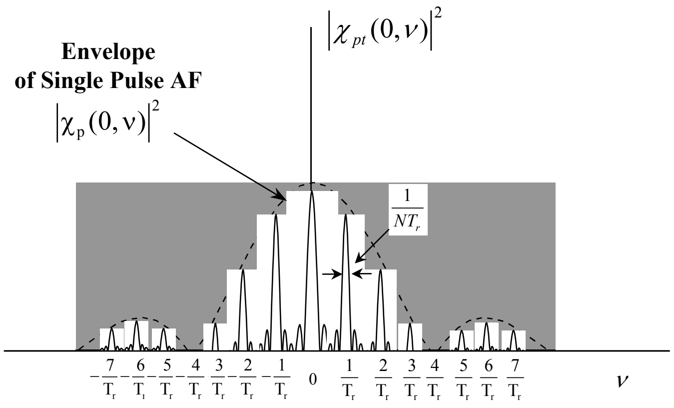

Figure 1-9, Ambiguity Along the Doppler Axis for Uniform Pulse Train [20:291]

The volume constraint of Eq (1.30) requires that the volume removed (redistributed) from under the single pulse ambiguity surface, due to the PRF of the uniform pulse train, must equal the volume of the secondary spikes produced. Since the central spike of the ambiguity function is the primary contributor to measurement accuracy, the volume redistribution improves performance by creating a "clearer" area around the central spike. As N becomes larger, the ambiguity function approaches the "bed of nails" form shown in Figure 1-10. If all targets of interest lie within the clear area around the central spike, the waveform is adequate for detection. However, targets of interest may have ranges greater than $cT_r/2$ and/or Doppler shifts greater than $1/T_r$. In this case, the range and Doppler ambiguities can cause strong target masking.

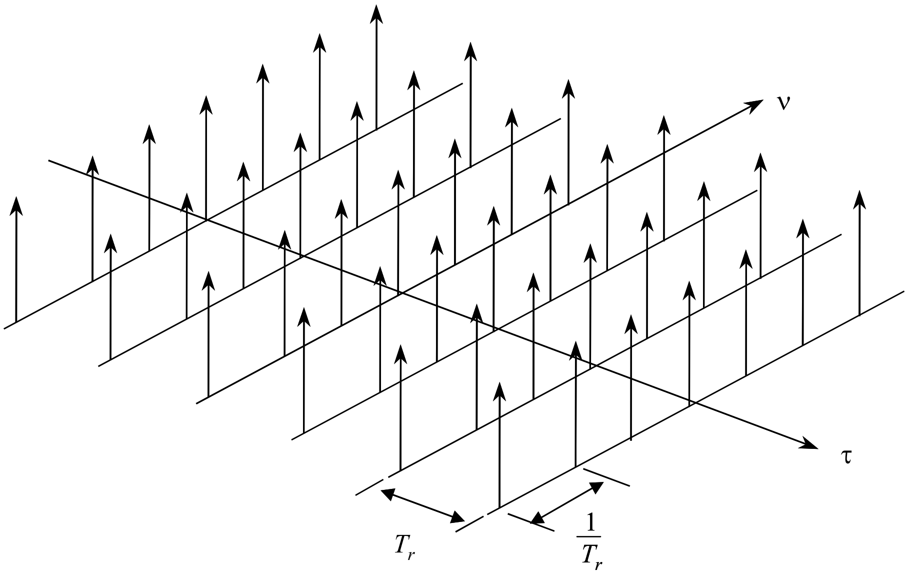

Figure 1-10. Bed of Spikes Ambiguity Surface

1.4 The Clutter Problem

Clutter may be defined as any response received from object(s) other than the target of interest. For radars attempting to detect moving targets in the air or on the ground, the ground return is generally the strongest source of clutter interference. Stationary ground-based radars normally employ Moving Target Indicator (MTI) techniques to eliminate clutter [1:232]. Since the radar and ground are both stationary in this scenario, an MTI radar can employ clutter cancellation techniques that effectively subtract the zero-Doppler components from successive pulses. This method has proven to be very efficient and has been applied to airborne radars for subtracting mainbeam clutter. The velocity of airborne platforms, combined with the radar antenna illumination pattern, induces various amounts of Doppler shift on ground returns, i.e., the ground return is spread in Doppler and range due to the radar antenna sidelobe characteristics. Figure 1-11 illustrates the geometry for an airborne intercept radar with velocity vector $\mathbf{v}_p$ attempting to detect another aircraft having velocity vector $\mathbf{v}_t$.

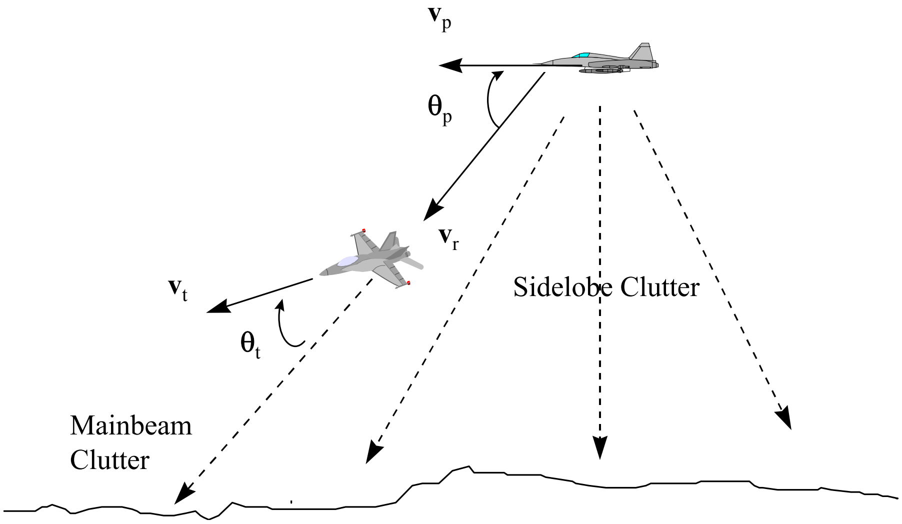

Figure 1-11. Airborne Radar Geometry

The relative target velocity with respect to the radar platform ($\mathbf{v}_r$) is given by Eq (1.33) and accounts for an induced Doppler shift given by Eq (1.34) [7]. In addition to the target return, the radar receives ground clutter returns from the mainbeam (in the target direction) and from the sidelobes (from all directions).

$$\mathbf{v}_r = \mathbf{v}_t \cos\theta_t + \mathbf{v}_p \cos\theta_p \tag{1.33}$$

$$f_d = \frac{2v_r}{\lambda} \ . \tag{1.34}$$

A general clutter Doppler spectrum for a single pulse radar is shown in Figure 1-12, where f_{dg} is the *maximum Doppler shift* induced by the ground, or the maximum Doppler shift due to sidelobe clutter that is above the receiver noise level. The strong peak at the carrier frequency (f_0) is a zero-Doppler term, called the altitude return, and is due to the ground located directly below the platform (this assumes of course that the platform is neither ascending or descending). As indicated, the altitude return is relative strong since it is generated from near-range clutter and a specular (versus diffuse) ground scattering response. The stronger mainbeam clutter response is primarily due to antenna gain in the scan direction (the ground scattering response is generally diffuse in the mainbeam direction). The fundamental clutter problem occurs when targets of interest possess Doppler returns that fall within the clutter spectrum. For this reason, airborne pulsed radars generally employ specific PRFs to ensure the spectrum has a sufficiently large "clutter-free" region for target detection.

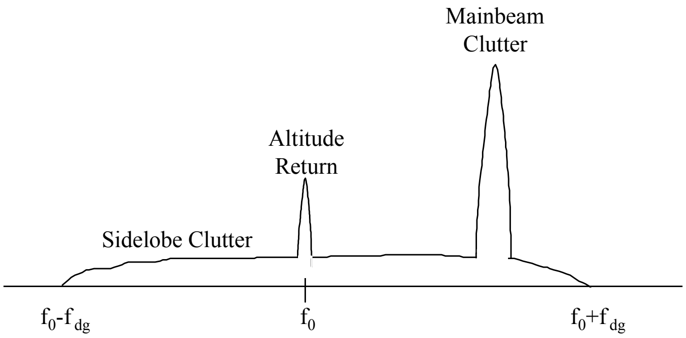

Figure 1-12. Doppler Spectrum for Single Pulse Airborne Radar

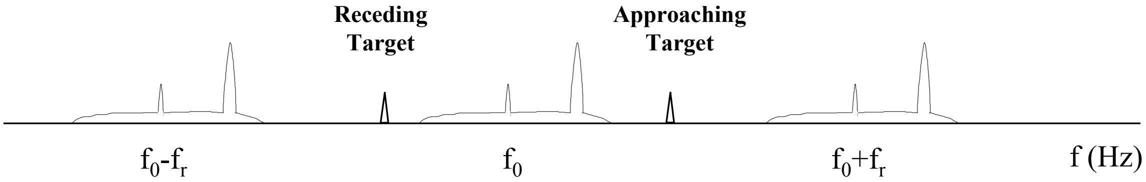

Figure 1-13. High-PRF Clutter Spectrum for Pulsed Radar

Figure 1-13 illustrates the clutter Doppler spectrum for a pulsed radar system and shows how the spectrum is periodic with a period equal to the PRF (f_r). As f_r increases, the clear region increases.

Although not explicitly shown, the periodic spectrum envelope is that of the single pulse spectrum; for a rectangular pulse the envelope spectral shape is a sinc(*f*) function.

From a Doppler only processing perspective, higher PRFs allow for larger clutter-free regions. However, higher PRFs produce highly ambiguous range situations and result in clutter fold-over, i.e., the clutter responses from multiple, successive range intervals are received simultaneously. Airborne radars typically resolve range ambiguities using FM ranging, PRF switching, or by adding lower PRF modes. In many cases, a medium PRF is a suitable compromise between range and Doppler ambiguities.

1.5 Existing Techniques for Resolving Range Ambiguities

There are three basic techniques for resolving range ambiguities: FM Ranging, Multiple PRFs (to include PRF switching), and pulse coding (or pulse diversity). Using multiple PRFs involves transmitting bursts of pulses and switching the PRF for each burst. Normally, three PRFs are used [2:273], but the concept is easily explained with two PRFs. Figure 1-14 illustrates two-PRF ranging [8:17.20], where the PRFs are selected to satisfy the following [8:17.21]

$$\begin{aligned} \text{PRF 1} &= \frac{n}{T_u} \\ \text{PRF 2} &= \frac{m}{T_u} \end{aligned} \tag{1.35}$$

where n and m are integers and T_u is a common sub-multiple of a given PRI. The true target range is determined from the coincidence of received pulses. Many techniques exist for selecting an appropriate set of multiple PRFs, including, the major-minor PRF method and the M:N method [2:274-277]. Likewise, one of many algorithms may be used to resolve the range ambiguities, including, the Chinese remainder theorem [8:17.20] and the residue look-up table algorithm [9].

The primary disadvantage of multiple PRFs is that coherent processing between multiple PRF bursts is not possible, reducing the overall CPI length. Thus, using multiple PRFs is less energy-efficient than a single PRF. Another problem is *ghosting*, i.e., false targets resulting from multiple targets and multiple PRFs. Advantages for using multiple PRFs include relatively simple implementation and good performance in mitigating *eclipsing*, i.e., target returns masked during pulse transmission (receiver blanking) are revealed when a different PRF is used.

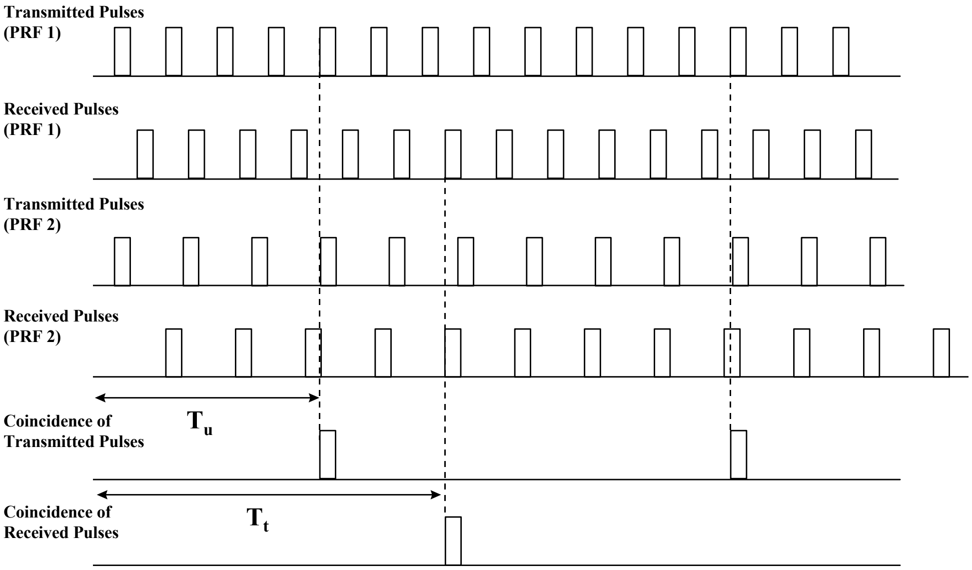

Figure 1-14. Two-PRF Ranging Illustration

Linear FM is often used in *range-while-search* (RWS) mode to implement FM ranging [2:95]. One example of this is implemented as follows: the processing dwell time is divided into two intervals, the first with no LFM and the second with LFM applied. The target Doppler shift is measured during the first interval. The return from the second interval will have a frequency shift proportional to range. The difference in frequency between the two intervals allows the range to be calculated, since the frequency shift is proportional to range [2:95]. Ghosting also occurs with LFM so that more than two intervals are often used. The basic LFM ranging limitations are achievable range resolution and additional clutter spreading.

Recent work sponsored by the National Weather Service has employed interpulse coding to resolve range ambiguities, similar to NLS processing in many respects. Sachidananda and Zrnic [10] applied a systematic code to a phase shifter, resulting in phase-coded pulses. “Second-trip” signals are recovered by first “cohering” (demodulating / matched filtering) the “first-trip” signal, an operation that simultaneously modulates the second-trip signal. The first-trip signal response is then removed with a notch filter and the second-trip signal is restored. By this technique, weaker signals (second-trip) overlaid in range with stronger signals (first-trip) may be recovered. This process is similar to NLS processing in that unwanted data is first suppressed after focusing and then the desired data is subsequently focused. The major difference is that pulse Doppler weather radars do not typically encounter the clutter Doppler spread that is so prevalent in military airborne radar systems.

1.6 Nonlinear Suppression (NLS)

1.6.1 The Nonlinear Suppression Concept

The radar nonlinear suppression technique was first introduced in a paper by Palermo, Leith, and Horgen [11] – an optical processor, analog LFM modulations, and a saturating nonlinearity were used to successfully demonstrate the NLS concept with real clutter data. However, the processing cost at that time severely limited the practicality of the technique. The current proliferation of extremely powerful digital signal processing (DSP) components warrants further investigation into the feasibility of implementing NLS at this time.

Pulse compression techniques using identically coded pulses are commonly applied in airborne radar applications. It is intuitively satisfying to consider the idea of uniquely coding individual pulses (interpulse coding) such that components of received ambiguous target returns may be uniquely identified as being from individually transmitted pulses. Figure 1-15 shows an example where two unique LFM pulse codes are used, $u_0(t)$ and $u_1(t)$, such that the FM modulation slope for u_0 is orthogonal to the FM modulation slope for u_1. In theory, the fact that pulses have been distinctively “tagged” should reduce the ambiguous range by a factor of two; given the pulses are interleaved in the pulse train, each series of uniquely coded pulses has a PRI equal to twice the overall PRI.

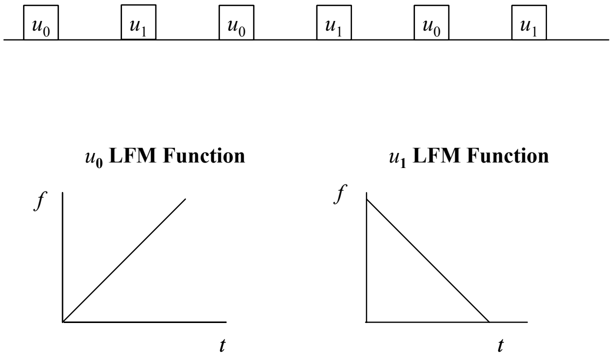

Figure 1-15. Interpulse Coding With Linear FM Waveforms

The composite received waveform $s(t)$ is applied to a receiver containing two matched filters (one for each unique pulse code), as shown in Figure 1-16, to produce two channel outputs, $y_0(t)$ and $y_1(t)$. When a u_0 response is received in Channel 0, the pulse response is compressed (focused). However, when u_1 responses arrive in Channel 0, they are dispersed (defocused) by the matched filter due to the conjugate code relationship – if the codes were perfectly orthogonal there would be no output response in this case. However, due to imperfect code characteristics perfect defocusing does not occur and the u_1 inputs may still produce a significant $y_0(t)$ output such that target detection occurs.

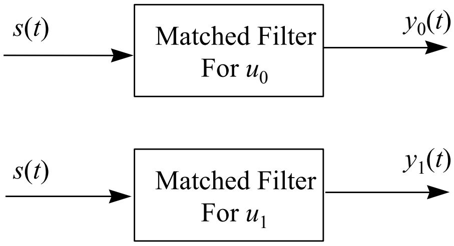

Figure 1-16. Matched Filter Channels for Phase Coded Pulses

The innovative idea introduced by Palermo in 1962 included the addition of a suppression operation to the traditional matched filter channels. Consider the example in the previous section, but with additional processing as shown in Figure 1-17.

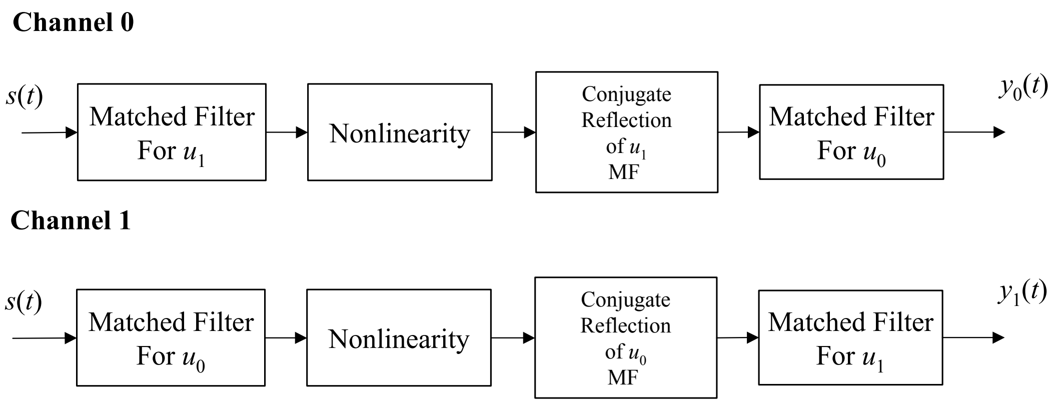

Figure 1-17. Basic Nonlinear Suppression Processing – Two Channel Case

In Channel 0, the received target return is first applied to a matched filter that "focuses" the undesired u_1 pulse responses – undesired here because the goal in this channel is to produce an output $y_0(t)$ that is only influence by u_0 pulse responses. The nonlinearity then suppresses all signal amplitudes above some predetermined or adaptive threshold level. Figure 1-18 shows two nonlinear functions used in NLS. The first, used by Palermo, Leith, and Horgen, is the hard limiter, which is represented by the function

$$\Gamma_\alpha(\sigma) = \begin{cases} \text{sign}(\sigma)\cdot\alpha & \text{if } |\sigma| > \alpha \\ \sigma & \text{otherwise} \end{cases} \tag{1.36}$$

where alpha is a positive, real threshold. The second nonlinear function, used in this work, is the hole-punch function, given by

$$\Gamma_\alpha(\sigma) = \begin{cases} 0 & \text{if } |\sigma| > \alpha \\ \sigma & \text{otherwise .} \end{cases} \tag{1.37}$$

For complex signal processing, the threshold may be independently applied to the in-phase (I) and quadrature (Q) channels.

The signal is then passed through the conjugate u_1 matched filter (defocuses the remains of the u_1 response) and is applied to a matched filter for u_0. The output $y_0(t)$ consists of components from u_0 pulse responses plus a small amount of residual content from u_1 pulse responses; the unwanted pulse responses in Channel 0 have been suppressed. Channel 1 is the complement of Channel 0, where the u_0 pulses are suppressed. The resultant effect of the NLS receiver is that each channel has an effective PRI equal to twice the original PRI, hence twice the unambiguous range. NLS was further extended in [12], where four Gold codes were used to demonstrate the concept for point targets with ranges up to $4R_u$.

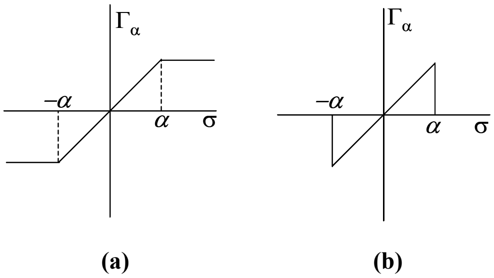

(a) **(b)**

Figure 1-18. Nonlinearities Used in NLS (a) Hard Limiter (b) Hole-Punch

1.6.2 Research Objectives

The primary goal of this research is to lay a solid foundation for future NLS research by accomplishing five objectives. The first objective is to resurrect and update the NLS concept first introduced in 1962 by implementing with discrete coding and discrete processing. The second objective is to develop a NLS theory that is consistent with other research. Most of the related work has been focused on pulse diversity, primarily to improve the distribution of volume on the ambiguity surface. The NLS technique proposed here is unique in its use of a suppression operator and its relationship to pulse diversity. Both are addressed here.

The third objective is to determine an effective and efficient means for determining a viable thresholding technique for the nonlinear suppression operation. Since NLS performance is highly dependent upon correct threshold determination, a reliable method for obtaining the threshold is required.

The fourth objective is to identify and evaluate suitable discrete codes for NLS applications. One of the chief limitations of the original NLS demonstration that used analog LFM waveform coding is that the number of available codes is limited to two. Thus, only ambiguity reduction by a factor of two is achievable. Large families of well-known discrete codes have been employed in the communications field. These codes are examined for applicability to the radar NLS problem and some new codes are investigated as well.

The fifth objective is to evaluate radar NLS performance using real clutter. Since it is not feasible to perform flight tests using an NLS compatible radar system, existing measured data is artificially formatted and coded for NLS processing. Given the limitations inherent with using existing clutter data, the goal of this objective is to provide "proof-of-concept" test results to ensure the proposed NLS architecture can suppress distributed clutter to some degree. In this case, analog LFM NLS results are used as a benchmark for declaring the potential effectiveness of discrete code implementations.

1.7 Organization

Chapter 2 provides a review of past research on pulse diversity and introduces the newly developed ideal suppression operator. An approximation to the ideal suppression operator for NLS applications is established in a theorem. NLS thresholding is discussed, with two main techniques introduced and evaluated. Chapter 3 provides a review of widely used radar codes and introduces some well-known discrete codes used in communications. The Welch and Sarwate bounds for discrete codes are presented. An evaluation of well-known binary codes is conducted, along with new codes developed using combinatorial optimization. The theory of analog Brown codes, currently under development, is introduced for completeness. Chapter 4 presents an NLS evaluation model for the hole-punch nonlinearity and NLS results are analyzed using limited measured clutter data. Chapter 5 summarizes the research results and provides recommendations for future research. Finally, two appendices are included, one to define matched filtering and the correlation functions widely used in this work and one providing a comprehensive compilation of data generated and analyzed as part of the research.

2. *Theory of Ambiguity Suppression*

2.1 Diverse Pulse Trains

Waveform diversity takes many forms, including PRI diversity, frequency diversity, amplitude diversity, and phase diversity. Without applying some restrictions, a diverse pulse train may be made arbitrarily complicated. Here, the definition of a diverse pulse train is restricted such that all pulses $u_n(t)$ have equal amplitude and the PRI is constant. Only the phase function $\phi_n(t)$ varies as indicated in,

$$u_n(t) = a(t)\, e^{j\phi_n(t)} \tag{2.1}$$

$$s(t) = \sum_{n=0}^{N-1} u_n(t - nT_r) = \sum_{n=0}^{N-1} a(t - nT_r)\, e^{j\phi_n(t - nT_r)} \tag{2.2}$$

where $u_n(t)$ is a unit amplitude pulse function with effective duration T_p, $a(t)$ is an amplitude modulation function, N is the number of pulses, and T_r is the PRI. All pulses functions $u_n(t)$ have equal, finite energy. Since all pulses in a pulse train are sequentially transmitted, they form an ordered set P, consisting of N members.

$$P = \left\{ u_0,\, u_1,\, ...,\, u_{N-1} \right\} \tag{2.3}$$

$$\int_{-\infty}^{\infty} \left| u_n(t) \right|^2 dt = E < \infty \quad \forall \;\; n \in \left\{ 0, 1, ..., N-1 \right\} \tag{2.4}$$

$$Span(P) \subset L_2\left(\mathbb{R}, \mathbb{C}\right) \tag{2.5}$$

where $L_2(\mathbb{R}, \mathbb{C})$ is the space of complex Lebesque square-integrable functions of real numbers.

$$L_2(\mathbb{R}, \mathbb{C}) = \left\{ f : \mathbb{R} \rightarrow \mathbb{C} \mid f \text{ is a finite energy function defined on all of } \mathbb{R} \right\} \tag{2.6}$$

Some functions are restricted to subspaces of $L_2(\mathbb{R}, \mathbb{C})$:

$$L_2(\mathbb{R}, \mathbb{R}) = \left\{ f : \mathbb{R} \rightarrow \mathbb{R} \mid f \text{ is a finite energy function defined on all of } \mathbb{R} \right\} \tag{2.7}$$

$$L_2(\mathbb{R}, \mathbb{R}^+) = \left\{ f : \mathbb{R} \rightarrow \mathbb{R}^+ \mid f \text{ is a finite energy function defined on all of } \mathbb{R} \right\} \tag{2.8}$$

Generally, the independent variable for all functions is time (t).

If the amplitude modulation is Gaussian, the pulse functions are not strictly time limited, but have effective duration given by Eq (1.16). Rectangular pulses are time-limited, so that the span of P is a subspace of $L_2(-T_p, T_p)$. Two pulse functions u_n and u_m are *orthogonal* if they satisfy

$$\int_{-\infty}^{\infty} u_n(t)u_m(t)\,dt = \begin{cases} 0 & \text{if } n \neq m \\ E & \text{if } n = m \end{cases} \qquad (2.9)$$

where E is the energy of each pulse function.

For more than four decades, pulse diversity has been principally studied as a means of reducing *self-clutter*, i.e., the undesired volume located throughout the range-Doppler ambiguity plane. Many researchers have sought a means of optimizing the ambiguity surface by using pulse diversity. Their objective has been volume reduction under specific regions of the ambiguity surface using only coding. A somewhat promising coding technique that has periodically recurred in radar literature is based on *complementary sequences*. First introduced by Golay in 1961 [13], complementary code pairs exhibit the property that the sum of their autocorrelation functions is identically zero except for the zero-shift term. Later extensions include *quaternary codes* for pulsed radar (Welti codes) and *complementary sets*, both of which possess desirable correlation characteristics beyond pair wise considerations [14].

Sivaswamy [14] introduced *subcomplementary sequences* in 1978, which are complementary sequences applied to the repetition of a basic waveform. For example, a series of identical linear FM pulses of length T_c, each multiplied by +1 or –1 according to a complementary code set, are concatenated together to form a larger pulse of length T_p as shown in Figure 2-1. A binary complementary pair is illustrated here with the elemental linear FM pulse implied. Sivaswamy formed complementary sequences using Hadamard matrices having well-known/established orthogonality properties.

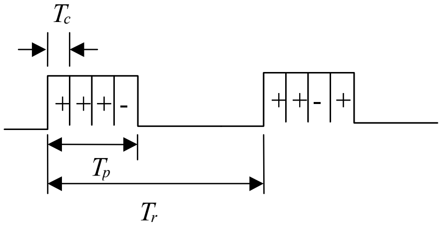

Figure 2-1. Subcomplementary Pair

Sivaswamy indicates that by forming receiver channels to process subcomplementary sequences, self-clutter on the ambiguity surface will cancel for all shifts greater than T_c, effectively removing volume under the ambiguity surface using cancellation properties of complementary sequences. However, Sivaswamy's claim is controversial and has not gone uncontested. For example, Zeoli [15] shows how Sivaswamy's results are invalid and no volume removal is obtained; rather, the volume thought to be removed is actually redistributed in Doppler.

Gerlach and Kretschmer [16, 17] exploit orthogonal matrices and complementary sets to form diverse pulse trains for suppressing range ambiguities. However, unlike Sivaswamy's work, they restrict their application to stationary targets and clutter. Thus, cancellation only takes place along the zero Doppler axis of the ambiguity plane.

In 1998, Guey and Bell [18] developed a general theory for diverse pulse coding. By considering the ambiguity function as a point-spread function for delay-Doppler imaging, and idealizing the radar system such that all pulses are transmitted simultaneously and processed independently, they established bounds for self-clutter suppression.

Theorem 1 (Guey-Bell) [18: 1508]. *For a set of signals* $\{u_0(t), u_1(t), \ldots, u_{M-1}(t)\}$ *with total energy given by*

$$E_T = \sum_{m=0}^{M-1} \int_{-\infty}^{\infty} \left| u_m(t) \right|^2 dt \tag{2.10}$$

and composite ambiguity function of

$$\chi_c(\tau,\nu) = \sum_{m=0}^{M-1} \chi_m(\tau,\nu) \tag{2.11}$$

where

$$\chi_m(\tau,\nu) = \int_{-\infty}^{\infty} u_m(t) u_m^*(t-\tau) e^{j2\pi\nu t}\, dt \tag{2.12}$$

defining the volume V_C *under their associated composite ambiguity function as*

$$V_C = \int_{-\infty}^{\infty}\int_{-\infty}^{\infty} \left| \sum_{m=0}^{M-1} \chi_m(\tau,\nu) \right|^2 d\tau d\nu \tag{2.13}$$

then, volume V_C *satisfies*

$$\frac{E_T^2}{M} \le V_C \le E_T^2 \ . \tag{2.14}$$

Furthermore, the minimum is achieved when {$u_0(t)$, $u_1(t)$, ..., $u_{M-1}(t)$} is a set of equal-energy orthogonal signals.

Hlawatsch [6:181] subsequently proved the Guey-Bell Theorem using the ambiguity function of a linear signal space. Both Guey-Bell and Hlawatsch assume an idealized radar system is used such that each $u_m(t)$ is independently transmitted, received, and processed before forming the composite ambiguity function. The time multiplexing inherent in the diverse pulse train of Eq (2.2) results in "range-walk" [6:178] as caused by target (and clutter) motion. If orthogonal phase coding is used to achieve the lower bound of Eq (2.14), Doppler compensation is required prior to forming the composite ambiguity function [18:1520].

Orthogonal codes, such as obtained from Hadamard matrices, are extremely sensitive to time and frequency variation and their use is usually restricted to systems capable of achieving high levels of synchronization. For example, the IS-95 digital cellular standard uses an orthogonal Walsh covering on the forward link (base-to-mobile) to enable multiple access capability [19:539]. Where near perfect synchronization is impractical, as with the mobile-to-base link of cellular systems, codes are chosen with good cross-correlation (dispersion) properties to enhance multiple access performance. Except for limited target environments, such as the stationary clutter scenario used by Gerlach and Kretschmer [17], the return from a diverse pulse train is inherently asynchronous and it is very unlikely that coding alone can achieve acceptable ambiguity suppression [15]. For this reason, this work introduces a suppression operator that, when combined with non-orthogonal diverse coding, results in a composite ambiguity function with volume approaching the Guey-Bell lower bound of Eq (2.14).

It is instructive to compare ambiguity functions of the uniform (Section 1.3) and diverse pulse trains. The uniform pulse train ambiguity function is repeated here as

$$\begin{aligned} \chi_s(\tau,\nu) &= \int_{-\infty}^{\infty} s(t)\, s^*(t-\tau)\, e^{j2\pi\nu t}\, dt \\ &= \sum_{n=0}^{N-1}\sum_{m=0}^{N-1} e^{j2\pi\nu n T_r}\, \chi_0\big(\tau-[n-m]T_r\,,\nu\big) \ . \end{aligned} \tag{2.15}$$

The reoccurring pulse ambiguity function χ_0 at multiples of T_r is evident in Eq (2.15), as is the Doppler sampling effect induced by the $\exp(j2\pi\nu n T_r)$ term. It is desirable to suppress these "surfaces" centered at $\tau \neq 0$ which may be accomplished using a two-fold process. First, pulse diversity may be introduced to reduce the pulse train periodicity. Most importantly, this diversity makes each pulse distinct. For the diverse pulse train of Eq (2.2), the ambiguity function is

$$\begin{aligned}\chi_s(\tau,\nu) &= \sum_{n=0}^{N-1} e^{j2\pi\nu nT_r}\chi_n(\tau,\nu) \\ &+ \sum_{n=1}^{N-1}\sum_{m=0}^{N-1} e^{j2\pi\nu mT_r}\,\chi_{m,m+n}(\tau+nT_r,\nu) \\ &+ \sum_{n=1}^{N-1}\sum_{m=0}^{N-1} e^{j2\pi\nu(m+n)T_r}\,\chi_{m+n,m}(\tau-nT_r,\nu)\ .\end{aligned} \tag{2.16}$$

The separation of auto-ambiguity terms, only appearing at $\tau = 0$, and cross-ambiguity terms, appearing at multiples of T_r, is the most distinctive feature of the diverse-pulse ambiguity function. This separation allows immediate identification of cross-ambiguity terms that represent range ambiguities that need to be suppressed.

The first summation term in Eq (2.16) represents a superposition of component ambiguity functions weighted by phase factor $\exp(j2\pi\nu nT_r)$. Per Guey and Bell, this is called the "weighted composite ambiguity function" and denoted $\tilde{\chi}_c(\tau,\nu)$.

$$\tilde{\chi}_c(\tau,\nu) = \sum_{n=0}^{N-1} e^{j2\pi\nu nT_r}\,\chi_n(\tau,\nu)\quad . \tag{2.17}$$

It is reasonable to assume all pulses have equal energy with the same effective duration and bandwidth. In this case, $\tilde{\chi}_c(\tau,\nu)$ can be approximated as [20:328]

$$\tilde{\chi}_c(\tau,\nu) \cong \chi_n(\tau,\nu)\sum_{n=0}^{N-1} e^{j2\pi\nu nT_r}\quad . \tag{2.18}$$

Equation (2.18) shows that near the origin ($\tau = 0$, $\nu = 0$), waveform coding does not affect the fine structure of the ambiguity surface when compared to the uniform pulse train. As Rihaczek [20:328] points out, the spreading of ambiguous surfaces resulting from cross-ambiguity terms of Eq (2.16) is a similar effect produced by PRI staggering. Since the later technique is much more easily implemented, the benefit of using pulse diversity to reduce pulse train periodicity appears questionable. However, as demonstrated in Section 1.2, the ability to distinguish pulses from one another when using pulse diversity allows greater suppression of range ambiguities.

2.2 The Ideal Suppression Operator

Given the diverse pulse train of Eq (2.2) with an ambiguity function expressed by Eq (2.16), the question arises: how can the undesirable cross-ambiguity terms be totally suppressed while retaining the desirable auto-ambiguity term? If the cross-ambiguity terms of Eq (2.16) can be suppressed, the system output merely becomes the weighted composite ambiguity function of Eq (2.17). A conventional radar receiver employing matched filter detection may be considered optimal (in terms of output signal-to-noise ratio) when operating over an additive white Gaussian noise channel. Normally, the ambiguity function is interpreted as the matched filter response to a received waveform with variable time-delay and Doppler. To suppress range ambiguities induced by diverse pulse train processing, the basic matched filter receiver structure is expanded to include a suppression operation. Consequently, the "suppressed ambiguity function", denoted by χ_s', is defined as the suppression receiver response and varies as a function of received signal time-delay and Doppler; ideally, the desired response is the auto-ambiguity term of Eq (2.16) with the cross-ambiguity terms totally suppressed. Therefore, the *suppressed ambiguity function* is simply the weighted composite ambiguity function

$$\begin{aligned}\chi_s'(\tau,\nu) &= \tilde{\chi}_c(\tau,\nu) \\ &= \sum_{n=0}^{N-1} e^{j2\pi\nu nT_r}\,\chi_n(\tau,\nu) \\ &= \sum_{n=0}^{N-1}\int_{-\infty}^{\infty} u_n\left(t-nT_r\right)u_n^*\left(t-\tau-nT_r\right)e^{j2\pi\nu t}\,dt \quad .\end{aligned} \tag{2.19}$$

To achieve this response, the "ideal suppression operator" (ISO) Λ_n is introduced [21], with the primary property that if

$$s(t) = \sum_{k=0}^{N-1} a_k\, u_k(t-\tau_k) \tag{2.20}$$

then

$$\left[\,\Lambda_n s\,\right](t) = a_n\, u_n(t-\tau_n)\,. \tag{2.21}$$

Applying Eq (2.21) to Eq (2.19) yields

$$\chi_s'(\tau,\nu) = \sum_{n=0}^{N-1}\int_{-\infty}^{\infty}\left[\Lambda_n s\;\right](t)\left[\Lambda_n s^*\right](t-\tau)\,e^{j2\pi\nu t}\,dt \tag{2.22}$$

where the ideal suppression operator has been applied to pulse train $s(t)$ to yield the individual pulse functions u_n .

The delay associated with each pulse may be expressed using the operator D_k

$$\left[D_k u_k\right](t) = u_k(t-\tau_k) \tag{2.23}$$

so that Eq (2.20) may be rewritten as

$$s(t) = \sum_{k=0}^{N-1} a_k \left[D_k u_k\right](t) . \tag{2.24}$$

Definition 1 (Ideal Suppression Operator). *Let s(t) be a linear combination of N non-orthogonal complex pulse functions $u_k(t)$ from an ordered set $P = \{u_0, u_1, \ldots u_{N-1}\}$ each weighted by a complex constant a_k and with delay operator D_k*

$$s(t) = \left[\sum_{k=0}^{N-1} a_k \, D_k \, u_k\right](t) \quad . \tag{2.25}$$

For each n ∈ {0,1…,*N*-1}, *the n^{th} ideal suppression operator (ISO), Λ_n, is defined such that Λ_n "selects" u_n from s*

$$\left[\Lambda_n s\right](t) = \left[\Lambda_n \sum_{k=0}^{N-1} a_k \, D_k \, u_k\right](t) = a_n \, u_n(t-\tau_n) . \tag{2.26}$$

From the ISO definition, the following properties may be established

(1) Λ_n is a *linear operator* on L_2 ($\Lambda_n : L_2 \to L_2$). Let

$$\begin{aligned} s_1(t) &= \sum_{j=0}^{N-1} a_j \, u_j(t-\tau_j) \\ s_2(t) &= \sum_{k=0}^{N-1} b_k \, u_k(t-\delta_k) \quad . \end{aligned} \tag{2.27}$$

Note that the delay values may be different for each pulse train. Define delay operators D_k and Δ_k by

$$\begin{aligned} \left[D_k \, u_k\right](t) &= u_k(t-\tau_k) \\ \left[\Delta_k \, u_k\right](t) &= u_k(t-\delta_k) \quad . \end{aligned} \tag{2.28}$$

Let $c_1, c_2 \in \mathbb{C}$. Then

$$\begin{aligned}
\left\{ \Lambda_n \left[c_1 s_1 + c_2 s_2 \right] \right\}(t) &= \Lambda_n \left[c_1 \sum_{j=0}^{N-1} a_j D_j u_j + c_2 \sum_{k=0}^{N-1} b_k \Delta_k u_k \right](t) \\
&= \Lambda_n \left[\sum_{j=0}^{N-1} c_1 a_j D_j u_j + \sum_{k=0}^{N-1} c_2 b_k \Delta_k u_k \right](t) \\
&= \left[c_1 a_n D_n u_n + c_2 b_n \Delta_n u_n \right](t) \\
&= c_1 a_n u_n(t-\tau_n) + c_2 b_n u_n(t-\delta_n) \\
&= c_1 \left[\Lambda_n s_1 \right](t) + c_2 \left[\Lambda_n s_2 \right](t) \ .
\end{aligned} \tag{2.29}$$

Thus, the ISO is linear on *P*.

(2) Λ_n is *idempotent*. That is, Λ_n is a projector.

$$\begin{aligned}
\left[\Lambda_n^2 s \right](t) &= \left[\Lambda_n \Lambda_n s \right](t) \\
&= \left[\Lambda_n a_n D_n u_n \right](t) \\
&= a_n u_n(t-\tau_n) \\
&= \left[\Lambda_n s \right](t) \ .
\end{aligned} \tag{2.30}$$

From this property, it is evident that Λ_n is a projector and $\left[\Lambda_n s \right]$ is a projection from the span of *P* to the one-dimensional space spanned by u_n.

A receiver architecture for forming the weighted composite ambiguity function is shown in Figure 2-2. In this figure, and all subsequent figures, an element with a single-line border represents the convolution operator, and double-lined elements represent direct operators. The h_0, h_1, . . . h_{M-1} convolution operators in the figure represent matched filters designed for optimal response to each of the distinctly encoded pulses of the pulse diverse waveform. The matched filter is defined by Eq (A.40) in Appendix A. Summing the matched filter outputs forms the desired weighted composite ambiguity function. The matched filter inputs are the result of applying an ISO and a delay operator with delay nT_r, where *n* corresponds to the pulse function. As will become apparent with Nonlinear Suppression (NLS), the process of applying the ISO and subsequent matched filtering, may be considered equivalent to designing a "channel" specifically tailored for optimally processing the single pulse response that is *not* being suppressed.

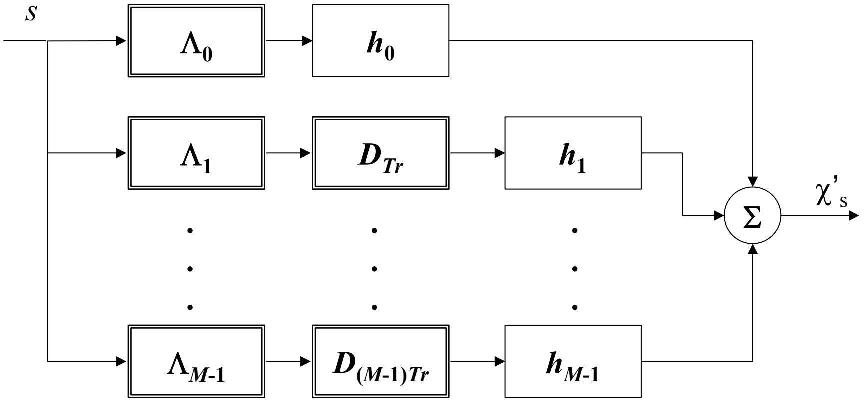

Figure 2-2. Receiver Architecture for Forming the Weighted Composite Ambiguity Function

2.3 *Nonlinear Suppression Operator*

The ideal suppression operator is a useful concept for introducing the general idea of suppression operators. By assuming ideal suppression, limits on range ambiguity removal/suppression can be established. It is also shown that introduction of the ISO achieves the lower bound on achievable ambiguity volume.

However, there is no existing technique for implementing a linear projection such as the ISO for a non-orthogonal pulse set when the time-delay and Doppler are unknown. In fact, these are the typical parameters to be estimated. A common receiver structure for either detecting targets and/or estimating the time-delay and Doppler uses using a bank of matched filters. In this case, each matched filter in the bank is "tuned" to a specific combination of time-delay and Doppler.

For the case involving a non-ideal suppression operator Λ_n, i.e., the cross-ambiguity terms in Eq (2.16) are not entirely suppressed, the resultant non-ideal suppression operation may be expressed as

$$\left[\Lambda_n s\right](t) = \left[\Lambda_n u_n\right](t) + \sum_{\substack{m=0 \\ m\neq n}}^{N-1}\left[\Lambda_n u_m\right](t) \quad . \tag{2.31}$$

The first term in Eq (2.31) represents distortion of u_n caused by the non-ideal suppression operator and the second term is the residual ambiguity. Each of these factors is addressed in detail in Section 2.3.3. The NLS technique proposed and developed under this work may be considered an approximate implementation for ideal suppression. As shown in the next section, NLS performance asymptotically approaches ideal suppression performance as the integrated sidelobe levels of autocorrelation function of the pulses in the diverse pulse train approach zero.

2.3.1 Nonlinear Suppression Fundamentals

Due to NLS complexity, it is helpful to define two nonlinear operations that form the basic elements of NLS receiver channels.

The first nonlinear operation is the hole punch operator, which is basic nonlinearity used in this work to perform suppression.

Definition 2 (Hole Punch Operator). *Let s be a complex function,* $s \in L_2(\mathbb{R},\mathbb{C})$*, and let* α *be a real, positive function,* $\alpha \in L_2(\mathbb{R},\mathbb{R}^+)$ *. The Hole Punch Operator is defined as the nonlinear* operator Γ_α *that attenuates all values of s(t) with magnitude greater than* $\alpha(t)$ *to zero*

$$\left[\Gamma_\alpha\, s\right](t) = \begin{cases} 0 & \text{if } \left|s(t)\right| > \alpha(t) \\ s(t) & \text{otherwise} \end{cases} . \tag{2.32}$$

The real function α is known as the *threshold*, and is determined uniquely every time the hole punch operator is applied.

Definition 3 (Elemental Suppression Operator). *Let u be a complex pulse function,,* $u \in L_2(\mathbb{R},\mathbb{C})$ *,and let h be the filter matched to complex pulse function u*

$$h(t) = u^*(-t) . \tag{2.33}$$

The matched filter h is uniquely determined by u, and $h \in L_2(\mathbb{R},\mathbb{C})$ *. Let s be a complex function,* $s \in L_2(\mathbb{R},\mathbb{C})$ *. Define the Elemental Suppression Operator* $\Theta_u : L_1(\mathbb{R},\mathbb{C}) \cap L_2(\mathbb{R},\mathbb{C}) \to L_1(\mathbb{R},\mathbb{C}) \cap L_2(\mathbb{R},\mathbb{C})$ *by*

$$\left[\Theta_u\, s\right](t) = \left[\Gamma_\alpha (s * h) * u\right](t) \,. \tag{2.34}$$

The elemental suppression operator, Θ_u, is uniquely determined by the pulse function *u*. Since the pulse train consists of the summation of multiple pulse functions u_n, the notation used to distinguish elemental suppression operators is $\Theta_m = \Theta_{u_m}$.

$$\left[\Theta_m s\right](t) = \left[\Theta_{u_m} s\right](t) = \left[\Gamma_\alpha(s * h_m) * u_m\right](t) \ . \tag{2.35}$$

Figure 2-3 graphically depicts the elemental suppression operator.

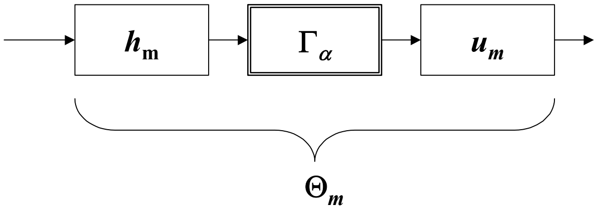

Figure 2-3. Elemental Suppression Operator

The elemental suppression operator is the core element of every NLS channel. Its purpose is to 1) "focus" the desired received pulse component while spreading other pulses in time, 2) "hole-punch" the focused data which should have much greater amplitude than the average, and 3) reverse the time-spread response of other pulses. Ideally, each NLS channel uses an elemental suppression operator to suppress all undesired pulses without significantly attenuating the desired pulse associated with that channel.

Although thresholding is discussed in detail in Section 2.3.4, the concept of the dispersed envelope threshold is introduced here to illustrate how NLS approximates the ISO performance. To illustrate how thresholds may be determined, consider the situation depicted in Figure 2-4. Here, a length 255 binary phase coded waveform is used and three point target returns are received from ranges of $R_u/4$, $3R_u/2$, and $11R_u/4$. Each target response is coded with one of three distinct phase codes, u_3, u_2, and u_1, respectively. When filtered by h_1, a filter matched to u_1, the filter output consists of cross-correlation components from targets #1 and #2 plus an autocorrelation component due to u_1 from target #3. Thus, the target #3 response is "focused" while responses from targets #1 and #2 are simultaneous "defocused." To suppress the focused response from target #3, a threshold is set such that the dispersed responses are not suppressed while the peak autocorrelation response is suppressed. For the case illustrated in Figure 2-4, either constant threshold α_1 (dot-dashed line) or variable threshold α_2 (dashed line) will work effectively, i.e., applying the nonlinear hole punch operation of Eq 2-16 suppresses the focused peak. Any threshold lying above the envelope of the dispersed codes and below any focused peaks is called the *dispersed envelope threshold* (DET). Although the DET may not be optimal in all cases, it intuitively has the least destructive effect on the desired signal (since it only suppresses focused pulse responses). It also provides some advantages in developing a useful theory relating NLS to ideal suppression.

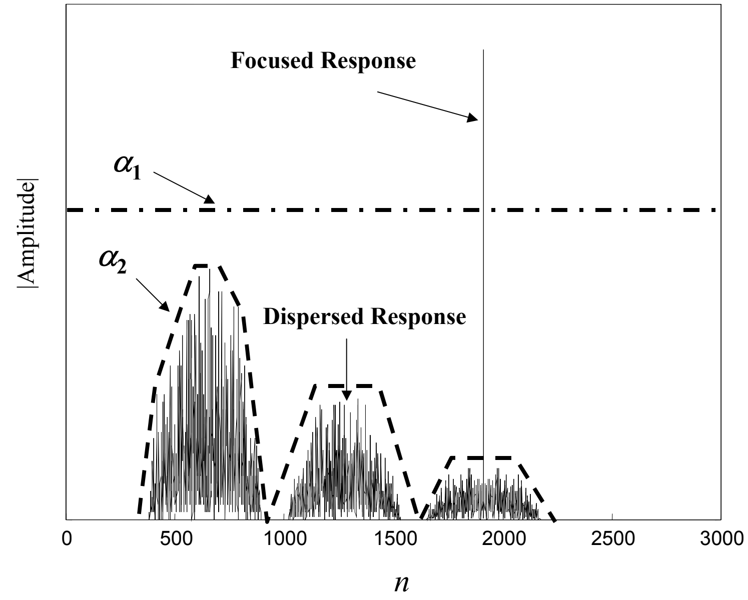

Figure 2-4. Dispersed Envelope Threshold Selection

When a diverse pulse train as defined by Eq (2.2) is applied to a matched filter h_m, which is matched to pulse code u_m, the response will consist of both a *focused response* and a *dispersed response*. Since matched filtering is equivalent to correlation, the focused (autocorrelation) response occurs when $n = m$

$$u_n(t) * h_m(t) = u_n(t) * h_n(t) = R_{nn}^*(t) \ . \tag{2.36}$$

The dispersed (crosscorrelation) response occurs when $n \neq m$

$$u_n(t) * h_m(t) = R_{nm}^*(t) \ . \tag{2.37}$$

Using these terms, the dispersed envelope threshold may be defined.

Definition 4 (Dispersed Envelope Threshold). *Let s be a signal consisting of a superposition of uniquely coded pulses from the ordered set P={u_0,u_1, ..., u_{N-1}}, with arbitrary time delay and amplitude.*

$$s(t) = \sum_{n=0}^{N-1} \left[a_n D_n u_n\right](t) \, . \tag{2.38}$$

Let h_m be the matched filter for pulse code u_m. Define the Dispersed Envelope Threshold (DET) as the real, positive function α, $\alpha \in L_2(\mathbb{R},\mathbb{R}^+)$, with the properties

$$\alpha(t) \geq \left| \sum_{\substack{n=0 \\ n\neq m}}^{N-1} \left[a_n D_n u_n * h_m \right](t) \right| \quad \forall t \tag{2.39}$$

$$\alpha(t) < \max_{-\infty < t < \infty} \left| \left[a_m D_m u_m * h_m \right](t) \right| \quad \forall t \ . \tag{2.40}$$

Thus the value dispersed envelope threshold exceeds the dispersed response for all t and is less than the focused response for all t (α_2 in Figure 2-4*).*

While the DET definition does not indicate how to generate it (presuming target locations unknown), it does help define what is required to achieve a particular operating condition. Under ideal DET conditions, only the unwanted focused pulse responses are suppressed by the nonlinearity while the desired dispersed pulse responses remain unaffected. Section 2.3.4 provides information on dispersed envelope selection for the special case of point targets.

2.3.2 Nonlinear Suppression Receiver Channel Structure

Each NLS receiver channel is formed using a sequence of elemental suppression operators followed by a matched filter for that particular channel. Figure 2-5 is an NLS receiver for Channel 0 which suppresses all pulse responses except for those due to code u_0. As indicated, the sequence of elemental suppression operators approximates the ideal suppression operator Λ_0.

The ordering of elemental suppression operators within an NLS receiver channel is determined based on the following. Since the power returned from each target is a function of range (R) and varies as $1/R^4$, the target response with the greatest amplitude is assumed to correspond to the most recently transmitted pulse. This is not always true since targets with larger radar cross-sections at longer ranges may produce the stronger returns. However, given target parameters are generally unknown, the ordering of suppression based on range is the best use of available information. By suppressing larger responses first, the cross-correlation levels are reduced in subsequent processing stages. This may be most significant when targets are overlaid in range. Note that the NLS channel structure does remain constant for every PRI. In fact, elemental ordering must be reconfigured for every PRI based on the most recently transmitted pulse. The channel configuration presented in Figure 2-5 assumes u_0 was the most recently transmitted pulse.

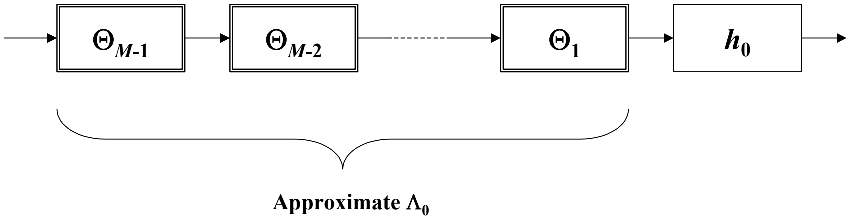

Figure 2-5. NLS Receiver Channel Structure, Channel 0

Definition 5 (Nonlinear Suppression Channel). *Let* $u_0, u_1, \ldots, u_{M-1}$ *be a sequence of transmitted pulses. Let* u_q *be the most recently transmitted pulse. The Nonlinear Suppression Channel for pulse n is defined as a sequence of elemental suppression operators* $\Theta_q, \Theta_{q-1}, \ldots \Theta_0, \Theta_{M-1}, \ldots, \Theta_{n+1}, \Theta_{n-1}, \ldots, \Theta_{q+1}$, *excluding* Θ_n, *sequentially applied to the input signal and subsequently followed by matched filter* h_n.

Figure 2-6 illustrates the NLS multi-channel receiver structure for the case when u_0 is the most recently transmitted pulse. The suppressed channel outputs may be utilized in a number of ways. For example, by adding delay operators as depicted in Figure 2-2, the weighted composite ambiguity function may be formed and Doppler processing may be applied for integration. For point targets, this operation will successfully resolve range ambiguities if the level of suppression is sufficient (a function of the pulse time-bandwidth product). In most practical applications, the number of codes (M) will be much lower than the number of transmitted pulses in a CPI (N). Doppler processing may be performed prior to the NLS operation on a block of N/M pulses to reduce the clutter cell size; NLS processing will subsequently follow.

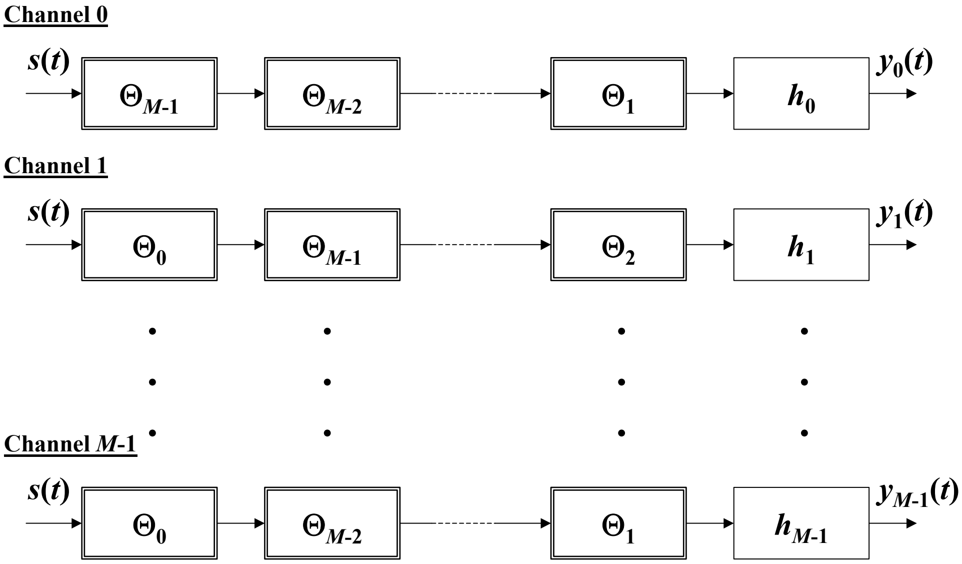

Figure 2-6. NLS Multi-Channel Receiver Structure

2.3.3 Distortion and Residual Ambiguity Effects

When suppression is not ideal, as with NLS, Eq (2.31) applies and may be analyzed to determine distortion and residual ambiguity effects. It is instructive to first consider the two-pulse case ($M = 2$). Let u_0 and u_1 be pulse functions with autocorrelation functions $R_{00}(\tau)$ and $R_{11}(\tau)$, and cross-correlation function $R_{01}(\tau)$. Let $s(t) = u_0(t) + u_1(t - T_r)$ be the input signal to the two channel NLS receiver.

If DET is used, as given by Definition 4, only the autocorrelation peak is suppressed. Let $Q_{nn}(\tau)$ be the result of suppression when DET is employed

Definition 6 (Suppressed Autocorrelation Function). *Let $R_{nn}(\tau)$ be the autocorrelation of u_n. The Suppressed Autocorrelation Function $Q_{nn}(\tau)$ is defined as the result of the hole-punch operator applied to the convolution of u_n and its matched filter h_n when a dispersed envelope threshold is used. That is, $Q_{nn}(\tau)$ is equal to zero for $|\tau| \le \tau_m$, where τ_m is the location of the mainlobe null and equal to $R_{nn}(\tau)$ for all other values of τ*

$$Q_{nn}(\tau) = \left[\Gamma_\alpha\left(u_n * h_n\right)\right](\tau) = \begin{cases} 0 & \text{if } |\tau| \le \tau_m \\ R_{nn}(\tau) & \text{otherwise} \end{cases} . \tag{2.41}$$

From (A.25) the autocorrelation function of pulse functions with duration T_p is nonzero only for values of τ in the closed interval $[-T_p, T_p]$. Since all pulse functions of interest are bounded and piecewise continuous, the autocorrelation function, $R_{nn}(\tau)$, is also bounded and piecewise continuous. From Definition 6, it is clear that the suppressed autocorrelation function, $Q_{nn}(\tau)$, is bounded and piecewise continuous on the closed interval $[-T_p, T_p]$, with a two discontinuities at $\tau = \pm\, \tau_m$. Therefore, $Q_{nn}(\tau)$ is Riemann-integrable on $[-T_p, T_p]$. Since $Q_{nn}(\tau)$ only contains autocorrelation sidelobes, the Integrated Sidelobe Level (ISL) of $R_{nn}(\tau)$ can be defined as the integral of the modulus squared of $Q_{nn}(\tau)$, divided by the peak response squared. The ISL is a common metric for assessing pulse code performance [22:537] and plays an important role in assessing the NLS performance of this work.

Definition 7 (Integrated Sidelobe Level). *Let $u_n(t)$ be a discrete complex pulse function of duration T, with autocorrelation function $R_{nn}(\tau)$ and suppressed autocorrelation function $Q_{nn}(\tau)$. The Integrated Sidelobe Level (ISL) of u_n is defined as the integral of $|Q_{nn}(\tau)|^2$ divided by the square of the peak response*

$$ISL(u_n) = \frac{\int_{-T}^{T} |Q_{nn}(\tau)|^2 \, d\tau}{R_{nn}^2(\tau = 0)} \tag{2.42}$$

Using Eq (A.45), the Channel 0 output is given by

$$\begin{aligned} y_0(t) &= \Big[\Big(\Gamma_\alpha\big[u_0 * h_1 \;+\; D_{T_r} u_1 * h_1\big]\Big) * u_1 * h_0\Big](t) \\ &= u_0(t) * h_1(t) * u_1(t) * h_0(t) \;+\; Q_{11}^*(t - T_r) * u_1(t) * h_0(t) \\ &= u_0(t) * u_1^*(-t) * u_1(t) * u_0^*(-t) \;+\; Q_{11}^*(t - T_r) * u_1(t) * u_0^*(-t) \\ &= R_{00}^*(t) * R_{11}^*(t) \;+\; Q_{11}^*(t - T_r) * R_{10}^*(t) \;\; . \end{aligned} \tag{2.43}$$

Using Eq (A.46), the Channel 1 output is given by

$$\begin{aligned} y_1(t) &= \Big[\Big(\Gamma_\alpha\big[\, u_0 * h_0 + D_{T_r} u_1 * h_0 \,\big]\Big) * u_0 * h_1\Big](t) \\ &= u_1(t - T_r) * h_0(t) * u_0(t) * h_1(t) \; + Q_{00}^* \; (t) * u_0(t) * h_1(t) \\ &= u_1(t - T_r) * u_0^*(-t) * u_0(t) * u_1^*(-t) \; + Q_{00}^* \; (t) * u_0(t) * u_1^*(-t) \\ &= R_{11}^*(t - T_r) * R_{00}^*(t) \; + Q_{00}^* \; (t_r) * R_{01}^*(t) \;\; . \end{aligned} \tag{2.44}$$

For each of these equations, the first term of the final expression represents the distorted autocorrelation function of the desired pulse, and the second term is the residual ambiguity.

Extension beyond two pulses requires implementation of a multi-channel receiver structure as shown in Figure 2-6. To illustrate, consider the case when $M = 4$ as shown in Figure 2-7. For this analysis, assume the received waveform is given by

$$s(t) = u_0(t) + u_1(t-T_r) + u_2(t-2T_r) + u_3(t-3T_r) \ . \tag{2.45}$$

Since all pulses are equal amplitude in this case, the order of processing is unimportant.

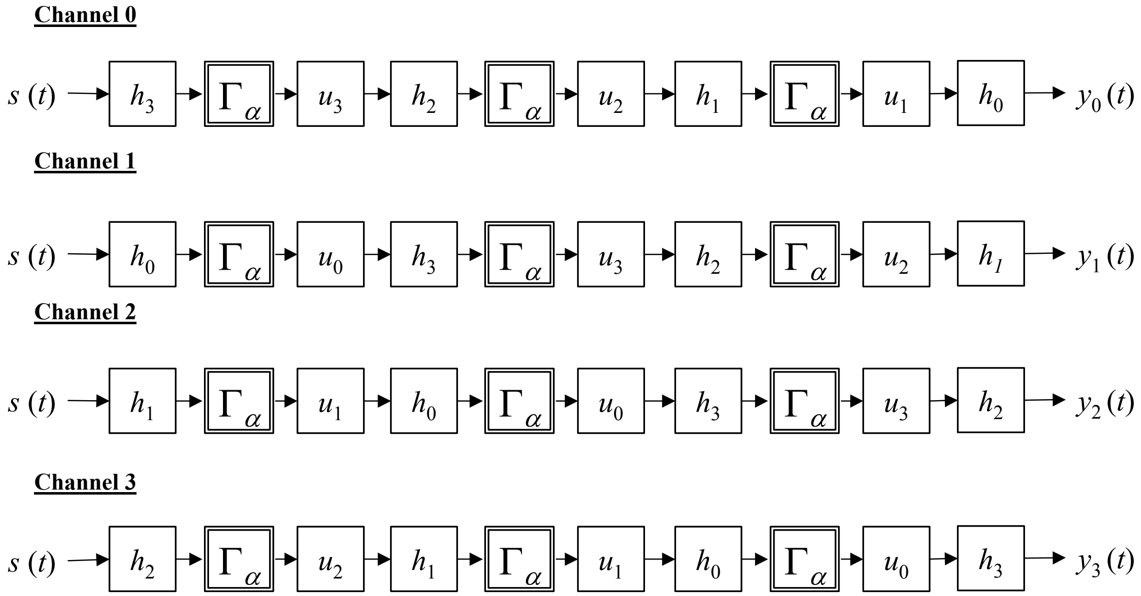

Figure 2-7. Four-Channel NLS Processor

Assuming DET, the Channel 0 output is given by

$$y_0(t) = \left[h_0 * u_1 * \Gamma_\alpha\left(h_1 * u_2 * \Gamma_\alpha\left[h_2 * u_3 * \Gamma_\alpha\left(h_3 * s\right)\right]\right)\right](t) \ . \tag{2.46}$$

Note that although the hole punch operator Γ_α is repeatedly applied, each occurrence of it uses a unique α that is assumed to be DET. Let the delay operator D_n be given by

$$\left[D_n \, a\right](t) = a(t - nT_r) \text{ for any signal } s \tag{2.47}$$

then

$$s(t) = \left[u_0 + D_1 u_1 + D_2 u_2 + D_3 u_3\right](t) \ . \tag{2.48}$$

When the ideal DET is used, the hole punch operator only suppresses the focused response, while leaving the dispersed response intact. Employing the definitions of the suppressed autocorrelation function and the hole-punch nonlinearity, the result of applying the hole punch to a pulse function is given by

$$\left[\Gamma_\alpha u_n h_m\right](t) = \begin{cases} R^*_{nm}(t) & \text{if } n \neq m \\ Q^*_{nn}(t) & \text{if } n = m \ . \end{cases} \tag{2.49}$$

Beginning with the first hole punch operator and working through Eq (2.46), results in

$$\Gamma_\alpha\left(h_3 * s\right) = h_3 * u_0 \ + \ h_3 * D_1 u_1 \ + \ h_3 * D_2 u_2 \ + \ D_3 Q^*_{33} \tag{2.50}$$

$$\begin{aligned} \Gamma_\alpha\left[h_2 * u_3 * \Gamma_\alpha\left(h_3 * s\right)\right] &= h_2 * u_3 * h_3 * \left(u_0 + D_1 u_1\right) \\ &\quad + \ u_3 * \left(h_3 * D_2 Q^*_{22} + h_2 * D_3 Q^*_{33}\right) \end{aligned} \tag{2.51}$$

$$\begin{aligned} \Gamma_\alpha\left(h_1 * u_2 * \Gamma_\alpha\left[h_2 * u_3 * \Gamma_\alpha\left(h_3 * s\right)\right]\right) &= h_1 * u_2 * h_2 * u_3 * h_3 * u_0 \\ &\quad + \ u_2 * h_2 * u_3 * h_3 * D_1 Q^*_{11} \\ &\quad + \ h_1 * u_2 * u_3 * h_3 * D_2 Q^*_{22} \\ &\quad + \ h_1 * u_2 * u_3 * h_2 * D_3 Q^*_{33} \end{aligned} \tag{2.52}$$

$$\begin{aligned} h_0 * u_1 * \Gamma_\alpha\left(h_1 * u_2 * \Gamma_\alpha\left[h_2 * u_3 * \Gamma_\alpha\left(h_3 * s\right)\right]\right) &= h_0 * u_1 * h_1 * u_2 * h_2 * u_3 * h_3 * u_0 \\ &\quad + \ h_0 * u_1 * u_2 * h_2 * u_3 * h_3 * D_1 Q^*_{11} \\ &\quad + \ h_0 * u_1 * h_1 * u_2 * u_3 * h_3 * D_2 Q^*_{22} \\ &\quad + \ h_0 * u_1 * h_1 * u_2 * u_3 * h_2 * D_3 Q^*_{33} \\ &= R^*_{00} * R^*_{11} * R^*_{22} * R^*_{33} \\ &\quad + \ R^*_{10} * R^*_{22} * R^*_{33} * D_1 Q^*_{11} \\ &\quad + \ R^*_{20} * R^*_{11} * R^*_{33} * D_2 Q^*_{22} \\ &\quad + \ R^*_{30} * R^*_{11} * R^*_{22} * D_3 Q^*_{33} \end{aligned} \tag{2.53}$$

$$\begin{aligned} y_0(t) &= R^*_{00}(t) * R^*_{11}(t) * R^*_{22}(t) * R^*_{33}(t) \ + \ R^*_{10}(t) * R^*_{22}(t) * R^*_{33}(t) * Q^*_{11}(t - T_r) \\ &\quad + \ R^*_{20}(t) * R^*_{11}(t) * R^*_{33}(t) * Q^*_{22}(t - 2T_r) \ + \ R^*_{30}(t) * R^*_{11}(t) * R^*_{22}(t) * Q^*_{33}(t - 3T_r) \ . \end{aligned} \tag{2.54}$$

Applying the same procedure to each NLS channel results in

$$\begin{aligned} y_1(t) &= R^*_{00}(t) * R^*_{11}(t - T_r) * R^*_{22}(t) * R^*_{33}(t) \ + \ R^*_{01}(t) * R^*_{22}(t) * R^*_{33}(t) * Q^*_{00}(t) \\ &\quad + \ R^*_{21}(t) * R^*_{00}(t) * R^*_{33}(t) * Q^*_{22}(t - 2T_r) \ + \ R^*_{31}(t) * R^*_{00}(t) * R^*_{22}(t) * Q^*_{33}(t - 3T_r) \end{aligned} \tag{2.55}$$

$$\begin{aligned} y_2(t) &= R^*_{00}(t) * R^*_{11}(t) * R^*_{22}(t - 2T_r) * R^*_{33}(t) \ + \ R^*_{02}(t) * R^*_{11}(t) * R^*_{33}(t) * Q^*_{00}(t) \\ &\quad + \ R^*_{12}(t) * R^*_{00}(t) * R^*_{33}(t) * Q^*_{11}(t - T_r) \ + \ R^*_{32}(t) * R^*_{00}(t) * R^*_{11}(t) * Q^*_{33}(t - 3T_r) \end{aligned} \tag{2.56}$$

$$\begin{aligned} y_3(t) &= R^*_{00}(t) * R^*_{11}(t) * R^*_{22}(t) * R^*_{33}(t - 3T_r) \ + \ R^*_{03}(t) * R^*_{11}(t) * R^*_{22}(t) * Q^*_{00}(t) \\ &\quad + \ R^*_{13}(t) * R^*_{00}(t) * R^*_{22}(t) * Q^*_{11}(t - T_r) \ + \ R^*_{23}(t) * R^*_{00}(t) * R^*_{11}(t) * Q^*_{22}(t - 2T_r) \ . \end{aligned} \tag{2.57}$$

The first term in NLS channel outputs of Eqs (2.54) thru (2.57) reveal the distortion induced by NLS and the remaining terms represent the residual ambiguity when DET is applied. The general form for N codes may be stated as follows. Let Π denote repeated convolution (a deviation from its normal symbolic use for multiplication). Let diverse pulse train $s(t)$ consist of N pulses and have the form specified in Eq (2.2). Each NLS channel output $y_n(t)$ is then given by

$$y_n(t) = R_{nn}^*(t-nT_r) * \prod_{\substack{m=0 \\ m\neq n}}^{N-1} R_{mm}^*(t) + \sum_{\substack{k=0 \\ k\neq n}}^{N-1} Q_{kk}^*(t-kT_r) * R_{kn}^*(t) * \prod_{\substack{m=0 \\ m\neq n \\ m\neq k}}^{N-2} R_{mm}^*(t) \ . \tag{2.58}$$

As presented in the next chapter, most codes considered for this work are discrete and it is useful to consider a discrete form of Eq (2.58). Assume the pulse repetition period T_r is an integer multiple of the sampling period T_s, i.e., $T_r = r\,T_s$. As shown in Appendix A, the normalized discrete correlation function θ_{mm} of Eq (A.39) may be used to represent the correlation function when pulses are discretely coded. For the discrete case, define $\mathbf{\Phi}_{mm}$ as the discrete form of the suppressed autocorrelation function Q_{mm} of Eq (2.41)

$$\Phi_{mm}(l) = \left[\Gamma_\alpha\left(u_m * h_n\right)\right](l) = \begin{cases} 0 & \text{if } l = 0 \\ \theta_{mm}(l) & \text{otherwise} \ . \end{cases} \tag{2.59}$$

The ISL for discrete pulses may also be defined using either the aperiodic correlation function or the normalized aperiodic correlation function

$$ISL(u_n) = \frac{\displaystyle\sum_{\substack{l=N-1 \\ l\neq 0}}^{N-1} \left| C_{nn}(l) \right|^2}{\left| C_{nn}(0) \right|^2} = \sum_{\substack{l=N-1 \\ l\neq 0}}^{N-1} \left| \theta_{nn}(l) \right|^2 = \sum_{l=N-1}^{N-1} \left| \Phi_{nn}(l) \right|^2 \ . \tag{2.60}$$

For code sequences of length N, the discrete form of Eq (2.58) becomes

$$y_m[n] = \theta_{mm}^*[n-mr] * \prod_{\substack{j=0 \\ j\neq m}}^{N-1} \theta_{jj}^*[n] + \sum_{\substack{k=0 \\ k\neq m}}^{N-1} \Phi_{kk}^*[n-kr] * \theta_{km}^*[n] * \prod_{\substack{j=0 \\ j\neq m \\ j\neq k}}^{L-2} \theta_{jj}^*[n] \ . \tag{2.61}$$

The elemental suppression operator Θ_m, from Definition 3, may be expressed in terms of the suppressed autocorrelation function when the threshold is DET. Using $s(t)$ of the form

$$s(t) = \sum_{n=0}^{N-1} u_n(t-nT_r) = \sum_{n=0}^{N-1} \left[D_n\, u_n\right](t) \tag{2.62}$$

and inserting into Eq (2.34) while applying Definition 6

$$\begin{aligned}\left[\Theta_m\, s\right](t) &= \left[\Gamma_\alpha\left(\sum_{n=0}^{N-1} D_n u_n * h_m\right)\right](t) * u_m(t) \\ &= Q^*_{mm}(t - mT_r) * u_m(t) + \sum_{\substack{n=0 \\ n \neq m}}^{N-1} R^*_{mm}(t) * u_n(t - nT_r) \;\; . . \qquad (2.63)\end{aligned}$$

In discrete form

$$s[n] = \sum_{k=0}^{N-1} u_k[n - kr] = \sum_{k=0}^{N-1} \left(D_k u_k\right)[n] \qquad (2.64)$$

$$\begin{aligned}\left(\Theta_m s\right)[n] &= \left(\left[\Gamma_\alpha\left(\sum_{k=0}^{N-1} D_k u_k * h_m\right)\right] * u_m\right)[n] \\ &= \Phi^*_{mm}[n - mr] * u_m[n] + \sum_{\substack{k=0 \\ k \neq m}}^{N-1} \theta^*_{mm}[n] * u_k[n - kr] \;\; . . \qquad (2.65)\end{aligned}$$

Each NLS channel repeatedly applies the elemental suppression operator *N*-1 times, resulting in Eq (2.58) for continuous signals and Eq (2.61) for discrete signals. From the discrete form, it is now shown that by applying NLS using a set of perfect codes (codes with zero autocorrelation sidelobes) results in ideal suppression performance for each channel.

Lemma 1. *The limit of the normalized autocorrelation function as the ISL approaches zero is the unit impulse function.*

Proof: For discrete pulses, the normalized autocorrelation function may be written as the sum of the suppressed autocorrelation function and the unit impulse function

$$\theta_{nn}(l) = \Phi_{nn}(l) + \delta(l) \qquad (2.66)$$

where the unit impulse function is defined as [23:30]

$$\delta(l) = \begin{cases} 1 & \text{if } l = 0 \\ 0 & \text{otherwise} \end{cases} \; . \qquad (2.67)$$

From Definition 7 and Eq (2.60), $ISL(u_n)$ is the summation of the modulus squared of the suppressed autocorrelation function, $\Phi_{nn}(l)$. Therefore, the $ISL(u_n)$ approaches zero as the summation of $|\Phi_{nn}(l)|^2$ approaches zero. Since this is a summation of positive terms, the $ISL(u_n)$ can only approach zero as the individual terms $\Phi_{nn}(l)$ approach zero.

Applying the limit as $ISL(u_n)$ approaches zero to Eq (2.66)

$$\begin{aligned}\lim_{ISL(u_n)\to 0}\theta_{nn}(l) &= \lim_{ISL(u_n)\to 0}\left[\Phi_{nn}(l) + \delta(l)\right] \\ &= \lim_{ISL(u_n)\to 0}\Phi_{nn}(l) + \delta(l) \\ &= \delta(l)\ .\end{aligned} \tag{2.68}$$

☐

Lemma 2. *Let s[n] be a pulse train consisting of a set of discrete complex pulse functions* $u_0[n]$, $u_1[n-r]$, *...,* $u_{M-1}[n-(M-1)r]$ *of length N, as defined by Eq*(2.64). *Then the limit of the elemental suppression operator* Θ_m *as the ISL of* u_n *approaches zero, when the thresholding is DET, is given by*

$$\lim_{ISL(u_m)\to 0}\left(\Theta_m s\right)[n] = \sum_{\substack{k=0\\k\neq m}}^{N-1} u_k[n-kr]\ . \tag{2.69}$$

<u>Proof</u>: From Eq (2.65), the output of the elemental suppression operator is

$$\left(\Theta_m s\right)[n] = \Phi^*_{mm}[n-mr]*u_m[n] + \sum_{\substack{k=0\\k\neq m}}^{N-1}\theta^*_{mm}[n]*u_k[n-kr]\ . \tag{2.70}$$

As $ISL(u_m)$ approaches zero, the summation terms of Eq (2.60) must also approach zero, since all terms are positive. Therefore, the first term of Eq (2.70) approaches zero as $ISL(u_m)$ approaches zero, that is

$$\lim_{ISL(u_m)\to 0}\Phi^*_{mm}[n-mr]*u_m[n] = 0\ . \tag{2.71}$$

By Lemma 1, the autocorrelation $\theta_{mm}[n]$ approaches the delta function as $ISL(u_m)$ approaches zero. From the sifting property of the unit impulse function, convolution with a unit impulse function is the identity operation [23:109], so that the second term becomes, in the limit

$$\lim_{ISL(u_m)\to 0}\sum_{\substack{k=0\\k\neq m}}^{N-1}\theta^*_{mm}[n]*u_k[n-kr] = \sum_{\substack{k=0\\k\neq m}}^{N-1}u_k[n-kr]\ . \tag{2.72}$$

Combining results of Eq (2.71) with Eq (2.72) yields Eq (2.69). ☐

Theorem 2 (Main Nonlinear Suppression Theorem). *Let s[n] be a pulse train consisting of a set of discrete complex pulse functions* $u_0[n]$, $u_1[n]$, *...,* $u_{M-1}[n]$ *of length N as defined by Eq*(2.64). *Let* $y_m[n]$ *be the* m^{th} *nonlinear suppression channel output, with dispersed envelope thresholding used for each* *elemental suppression operator, as given by Eq* (2.61). *As the integrated sidelobe level of each pulse function approaches zero, the m^{th} nonlinear suppression channel operation approaches the ideal suppression operation Λ_m. That is, for each m and for all n*

$$\begin{aligned} \lim_{\substack{ISL(u_k)\to 0 \\ k\in[0,M-1]}} y_m[n] &= \left(\Lambda_m s\right)[n] * u_m^*[-n] \\ &= \theta_{mm}^*[n] \ . \end{aligned} \tag{2.73}$$

<u>Proof</u>: From Eq (2.61) , $y_m[n]$ is the m^{th} NLS channel output, which is repeated here

$$y_m[n] = \theta_{mm}^*[n-mr] * \prod_{\substack{j=0 \\ j\neq m}}^{N-1} \theta_{jj}^*[n] + \sum_{\substack{k=0 \\ k\neq m}}^{N-1} \Phi_{kk}^*[n-kr] * \theta_{km}^*[n] * \prod_{\substack{j=0 \\ j\neq m \\ j\neq k}}^{L-2} \theta_{jj}^*[n] \ .$$

The NLS channel output is formed from repeated application of the elemental suppression operator Θ_k. The first term of Eq (2.61) approaches the unit impulse function as $ISL(u_k)$ approaches zero for all k (Lemma 1). The second term of Eq (2.61) approaches zero as $ISL(u_k)$ approaches zero for all k (Lemma 2). Therefore, for each $m \in \{0,1,...M-1\}$ and for all n

$$\begin{aligned} \lim_{\substack{ISL(u_k)\to 0 \\ k\in[0,M-1]}} y_m[n] &= \delta[n-mr] \\ &= \theta_{mm}^*[n-mr] \\ &= u_m[n-mr] * u_m^*[-n] \\ &= \left(\Lambda_m u_m\right)[n-mr] * u_m^*[-n] \ . \end{aligned} \tag{2.74}$$

Therefore, as $ISL(u_k)$ approaches zero for all k, the m^{th} NLS channel performance approaches ISO performance with the addition of a convolutional $u_m^*[-n]$ term. ☐

Theorem 2 clearly shows how NLS performance approaches ISO performance when coding is properly chosen. Also, since the codes are generally assumed to be non-orthogonal, NLS performance approaches the lower bound of Theorem 1. The subsurface at the origin of the diverse pulse train ambiguity function, Eq (2.16), has a volume equal to E_T^2/N [20:292], the lower bound of Theorem 1. Since the ISO suppresses all subsurfaces removed from the origin, due to the cross-ambiguity terms, the ISO achieves lower bound performance.

The Guey-Bell Theorem is based on an idealized radar system using independent receiver outputs that are coherently combined. An important distinction between coherent pulse train processing and the idealized radar system is the signal duration. If waveforms transmitted with the idealized radar system are pulse functions, the total time duration is the pulse width, T_p, as compared to total time duration NT_r for the coherent pulse train. The longer time duration of the coherent pulse train results in finer Doppler resolution, plus the inherent ambiguities of pulse repetition. The total volume is distributed under the various subsurfaces throughout the delay-Doppler plane. In contrast, the idealized radar system results in a single surface (as opposed to subsurfaces, or "spikes") without ambiguity. For this case, orthogonal coding can provide cancellation of certain regions of this surface. If orthogonal coding is possible with a coherent pulse train, the cross-ambiguity terms will cancel, leaving only the central subsurface at the origin with volume E_T^2/N. Thus, the Guey-Bell theorem is valid for coherent pulse train processing, although it is difficult to achieve good orthogonal coding performance when the delay and Doppler are unknown. It has been shown that NLS processing produces similar results when the condition of Theorem 2 is met.

Under dispersed envelope assumptions, NLS performance is only dependent on pulse autocorrelation functions and is not affected by cross-correlation characteristics. This result is significant since it is normally difficult to simultaneously achieve good autocorrelation and cross-correlation characteristics for a given set of codes (see Chapter 3). However, as shown in the following section, cross-correlation characteristics are an important consideration when trying to achieve DET conditions.

2.3.4 Thresholding

Dispersed envelope thresholding was defined in Section 2.3.1 as the threshold providing maximum suppression of autocorrelation peaks without suppressing responses below dispersed pulse levels. Because target parameters are unknown, the DET must be adaptive and based on received data for the current processing interval. Specifically, before applying the nonlinearity, the processor must determine a threshold value for each sample based upon the matched filter output prior to suppression.

Visual inspection of Figure 2-4 indicates the DET ideally tracks the envelope of the absolute value of the data. By definition, the dispersed envelope threshold always equals or exceeds the data except where a peak response occurs. To achieve this, two fundamental approaches are considered. The first approach is based on averaging and the second approach utilizes a reserved (non-transmitted) code to form a matched filter designed to "train" the NLS thresholding process.

2.3.4.1 Scaled Average Threshold

For a point target, a compressed pulse consists of a large peak, equal to some constant value *A* multiplied by the code length. Data values in the neighborhood of the peak are less than or equal to *A* multiplied by the peak autocorrelation sidelobe. For a "good" code, the sidelobe level is much less than the peak value. By averaging the absolute value of the data over some interval of length greater than one, the threshold value is guaranteed to be less than the peak. To ensure the threshold remains above the dispersed data level, i.e., above the code cross-correlation response(s), the average must be scaled, either over the entire data set or for each subinterval of interest. The main parameters for scaled average thresholding are the scaling constant, the averaging interval length, and the interval length over which the threshold is constant. Three basic approaches encapsulate the different ways these parameters may be varied

1) Constant Threshold. Averaging over all samples in a block of data (normally one PRI) and scaling the result produces a constant threshold. For N total samples, the constant threshold is given by

$$\alpha_C = \frac{a}{N}\sum_{n=0}^{N-1} |\, y[n] \,| \tag{2.75}$$

where a is the scaling constant and $y[n]$ is the output of the first matched filter in an NLS element.

2) Locally Constant Threshold. Instead of averaging over the entire PRI, the averaging may be done over a subinterval I_k of the PRI interval I_N. Let K be the length of the subinterval, chosen such that N/K is an integer. The locally constant threshold is given by

$$\alpha_k[n] = \frac{a}{K}\sum_{n \in I_k} |\, y[n] \,| \tag{2.76}$$

where a is the scaling constant.

3) Local Average Threshold. The average may be taken over an interval surrounding each sample n, and the entire threshold scaled by a single constant a. This method is a form of data smoothing where past and future values are used to compute the threshold for each data point. Typically, a smoothing operation is optimal for a specific form of interfering noise, e.g., additive white Gaussian noise. For NLS processing, the thresholding problem is not one of parameter estimation in the presence of noise. Rather, the problem involves estimating the data envelope while

excluding autocorrelation peaks. Letting $2b + 1$ the number of averaging samples, the local average threshold is given by

$$\alpha_L[n] = \frac{a}{(2b+1)} \sum_{k=n-b}^{n+b} |\, y[k] \,| \ . \tag{2.77}$$

where near the beginning and end of sequence $y[n]$ the average is taken over less than $2b+1$ total values.

The received data generally represents a superposition of ambiguous and unambiguous responses from a target field consisting of point targets and continuously distributed clutter. To gain insight into how well each of the three thresholding schemes perform, a target field consisting of only point targets was first considered. Consider a scenario where $R_1 = 0.25R_u$ and $R_2 = 1.75R_u$ are the ranges of two point targets with equal RCS. Choosing a PRI of $T_r = 4T_p$, for the given target ranges, ensures averaging is only done over nonzero data. Let the first target return be coded with $u_0[n]$ and the second target return be coded with $u_1[n]$. Initially, the target returns are assumed to have equal amplitude. Let $s[n]$ be the received data when both targets are present and $s_r[n]$ be the received data when only the first target is present. Apply both sequences to the filter matched to $u_1[n]$

$$\begin{aligned} y[n] &= s[n] * h_1[n] \\ y_r[n] &= s_u[n] * h_1[n] \ . \end{aligned} \tag{2.78}$$

Next, apply the hole-punch operator to y[n], which will suppress the first target. Then perform convolution of both $y[n]$ and $y_r[n]$ with $u_1[n]$. Finally, apply both $y[n]$ and $y_r[n]$ to the filter matched to $u_0[n]$. Let $y_s[n]$ be the result of the suppression operation and $y_c[n]$ be the "clean" data

$$y_s[n] = u_1[n] * h_0[n] * (\Gamma_\alpha y)[n] \tag{2.79}$$

$$y_c[n] = u_1[n] * h_0[n] * y_r[n] \ . \tag{2.80}$$

The mean-square error (MSE) of $y_s[n]$ compared to reference $y_c[n]$ is determined from

$$\bar{\varepsilon}^2 = \frac{\frac{1}{N}\sum_{n=0}^{N-1} \left| \beta y_s[n] - C_1 - y_c[n] + C_2 \right|^2}{\frac{1}{N}\sum_{n=0}^{N-1} \left| y_c[n] \right|^2} \tag{2.81}$$

where β is a scaling constant and C_1 and C_2 are bias constants. The constants are adjusted until the MSE is minimized, to eliminate non-zero bias and scaling factors.

To determine the performance of each thresholding scheme, and to find the parameters producing best performance, the above procedure is used while varying 1) a to determine the constant threshold value, 2) a and K to determine the locally constant threshold value, and 3) a and b to determine the local average threshold value. Five arbitrary binary code sets are used, with properties as summarized in Table 2-1. The PSL, ISL, and PCCL metrics are defined in Eq (3.1) through Eq (3.3).

Table 2-1. Code Properties for Minimum MSE Threshold Analysis

Code Length (*N*)	**PSL (dB)**	**Max ISL (dB)**	**PCCL (dB)**
63	-16.9	-4.7	-10.0
127	-20.5	-5.1	-21
255	-19.2	-1.1	-17.5
511	-22.3	-0.7	-20.0
1023	-24.2	-0.6	-22.6

Threshold estimation results are listed in Table 2-2. Estimated thresholds are plotted for a $TB = 127$ (Figure 2-8 through Figure 2-10) along with the output of the first matched filter. The minimum mean square error (MMSE) between the suppressed data and the distorted clean data is an indicator of how well the ambiguous energy was suppressed. A value of one indicates little to no suppression, while a value of zero indicates maximum suppression (the suppressed data and the clean data are identical).

Table 2-2. Minimum MSE Threshold Parametric Estimation Results

Code Length	**Constant Threshold**		**Locally Constant Threshold**			**Local Average Threshold**		
	MMSE	***a***	**MMSE**	***a***	***K***	**MMSE**	***a***	***b***
63	0..2477	5.9	0.23618	5.1	23	0.2477	4	2
127	0.17171	5.2	0.15381	2.6	19	0.15705	3.5	9
255	0.32301	4.1	0.29862	2.5	13	0.28941	2.6	2
511	0.30727	4.5	0.30397	3.8	16	0.30247	3.9	8
1023	0.32168	4.5	0.31243	3.4	30	0.31283	2.6	1

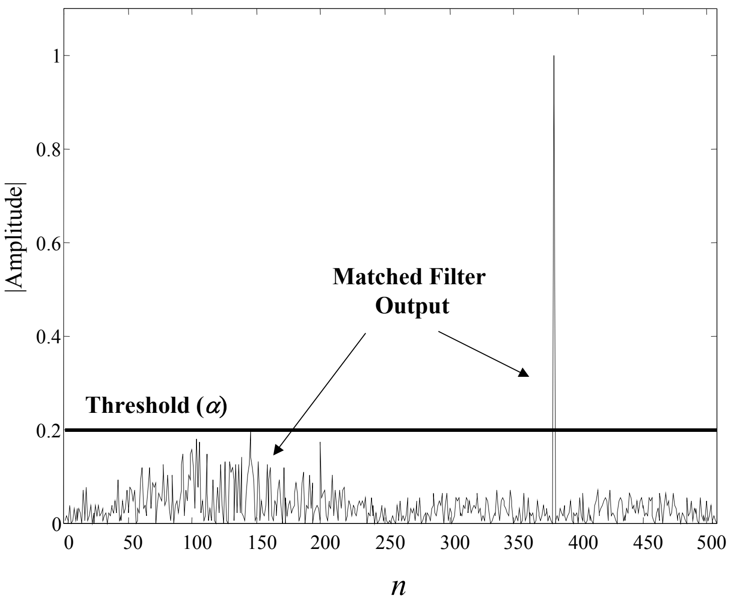

Figure 2-8. Constant Threshold, *TB* = 127, *a* = 5.2

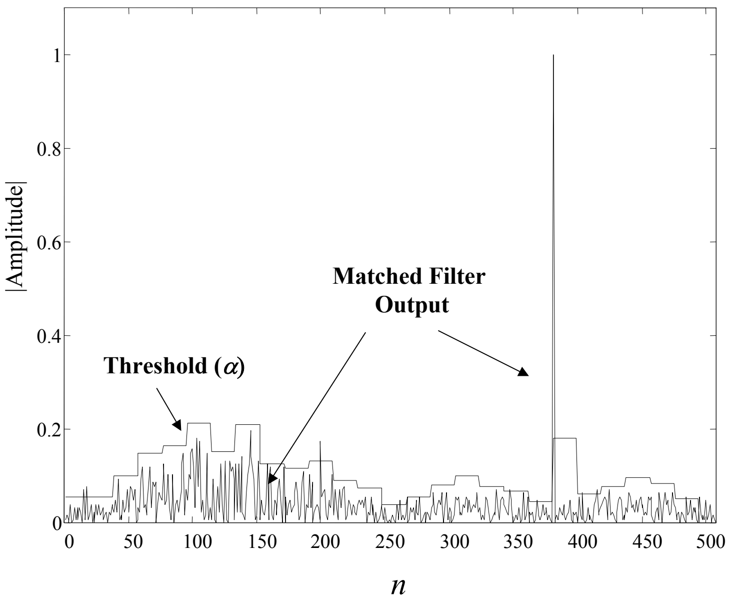

Figure 2-9. Locally Constant Threshold, *TB* = 127, *a* = 2.6, *K* = 19

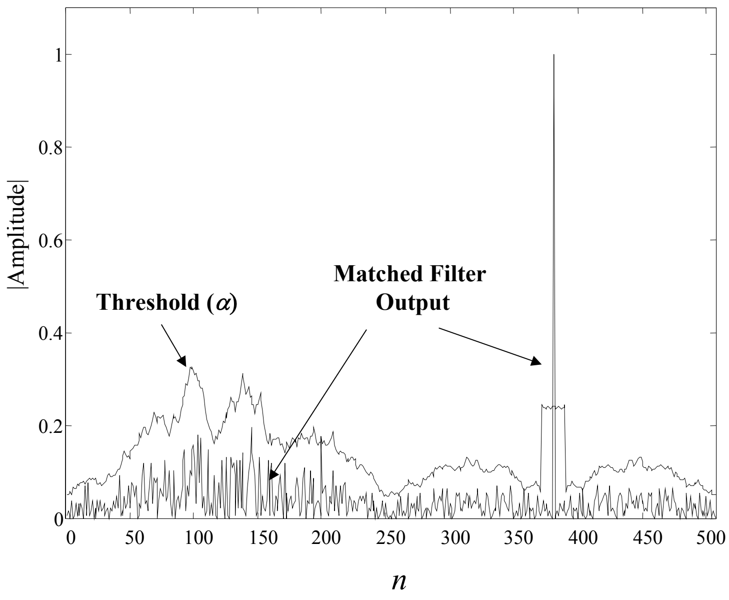

Figure 2-10. Local Average Threshold, *TB* = 127, *a* = 3.5, *b* = 9

Parameters a, b, and K in Table 2-2 do not follow a perceivable trend. Thus, there is no apparent rule for choosing them. To further analyze the threshold determination problem, the effects of range propagation loss are added to the MMSE characterization procedure. The amplitude of the target returns with range propagation loss included is found from

$$\frac{A_1}{A_2} = \sqrt{\frac{2P_1}{2P_2}} = \sqrt{\frac{\sigma_1 R_2^4}{\sigma_2 R_1^4}} = \sqrt{\frac{\sigma_1}{\sigma_2}}\left(\frac{R_2}{R_1}\right)^2 . \tag{2.82}$$

If the amplitude response of the first target ($R_1 = 0.25R_u$) is unity, and assuming unity RCS for both targets ($\sigma_1 = \sigma_2 = 1$), then the amplitude response of the second target ($R_2 = 1.75R_u$) is

$$A_2 = \sqrt{\frac{\sigma_2}{\sigma_1}}\left(\frac{R_1}{R_2}\right)^2 = \left(\frac{0.25}{1.75}\right)^2 = 0.0204 . \tag{2.83}$$

Table 2-3 Minimum MSE Threshold Parametric Estimation Results, With Range Propagation Loss

Code Length	**Constant Threshold**		**Locally Constant Threshold**			**Local Average Threshold**		
	MMSE	***a***	**MMSE**	***a***	***K***	**MMSE**	***a***	***b***
63	0.067643	8.7	0.000133	5.2	23	0.000143	4	2
127	0.000407	8.3	0.00000	3.3	5	0.000000	3.5	9
255	0.000599	7.8	0.000201	3.6	9	0.000204	3.6	2
511	0.000559	8.7	0.000178	3.7	6	0.000176	3.9	8
1023	0.000529	8.6	0.000193	4.2	11	0.000194	4.3	5

Threshold MMSE results including range propagation loss are summarized in and illustrated in Figure 2-11 through Figure 2-13. Comparing Table 2-2 to Table 2-3 reveals a much smaller MMSE for all cases. The weaker target contributes much less energy to the overall average, producing the smaller MSE. The scaling constants are generally larger. The averaging intervals are smaller for the locally constant threshold.

A major flaw with the constant thresholding approach is revealed in Figure 2-11. The contribution of the second target to the overall average, as taken over the entire PRI, is insignificant, i.e., the constant threshold value yielding MMSE is far greater than the peak response of the second target, preventing its suppression. Given the dependence of radar target return on range, the constant threshold is not a good candidate for NLS.

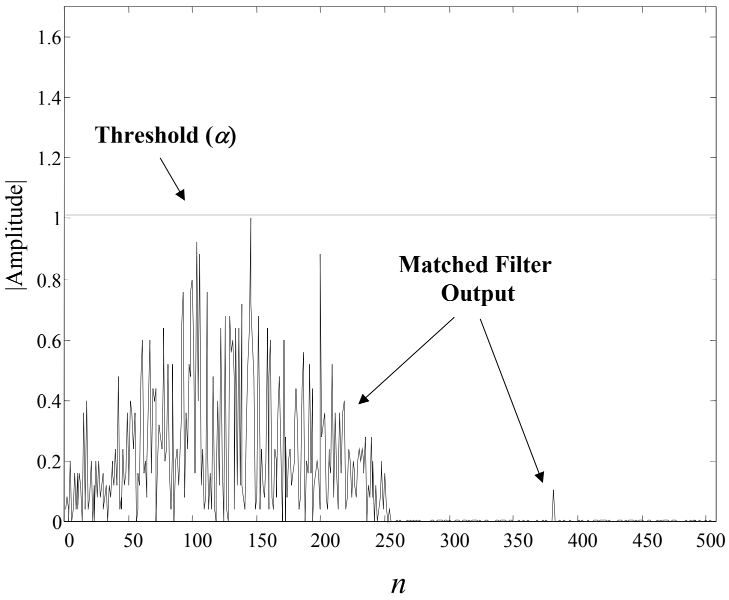

Figure 2-11. Range Propagation Loss, Constant Threshold, *TB* = 127, *a* = 8.3

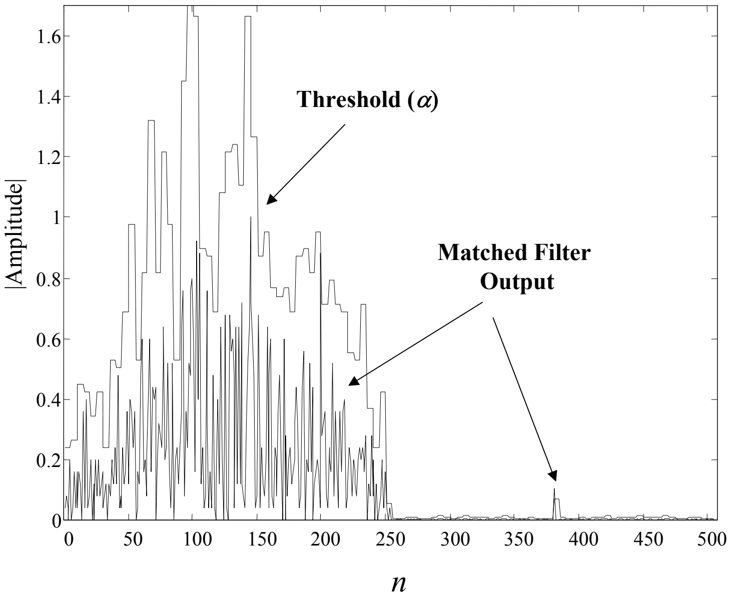

Figure 2-12. Range Propagation Loss, Locally Constant Threshold, *TB* = 127, *a* = 3.3, *K* = 5

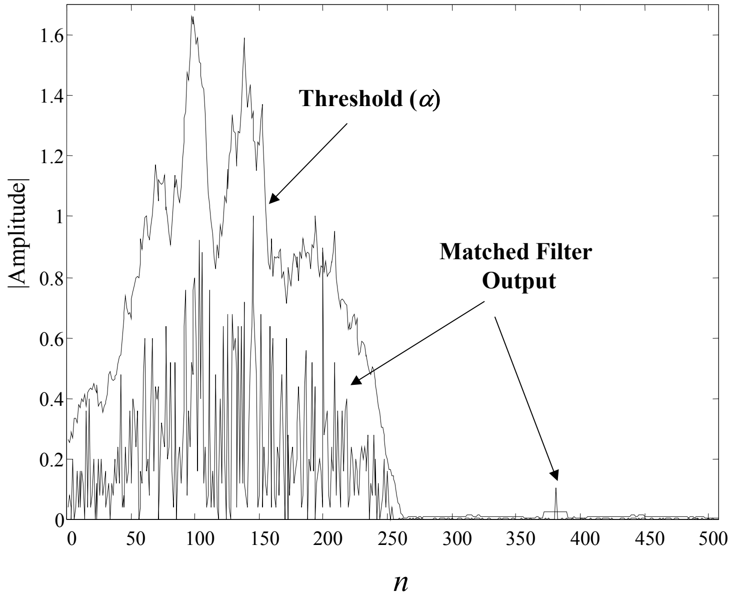

Figure 2-13. Range Propagation Loss, Local Average Threshold, *TB* = 127, *a* = 3.5, *b* = 9

The threshold near the weak target (which is compressed) is shown for the local average threshold (Figure 2-14) and the locally constant threshold (Figure 2-15). While both thresholds are below the peak, the locally constant threshold is higher than the local average threshold. This may be attributed to the smaller averaging interval ($K = 5$ vs. $b = 9$).

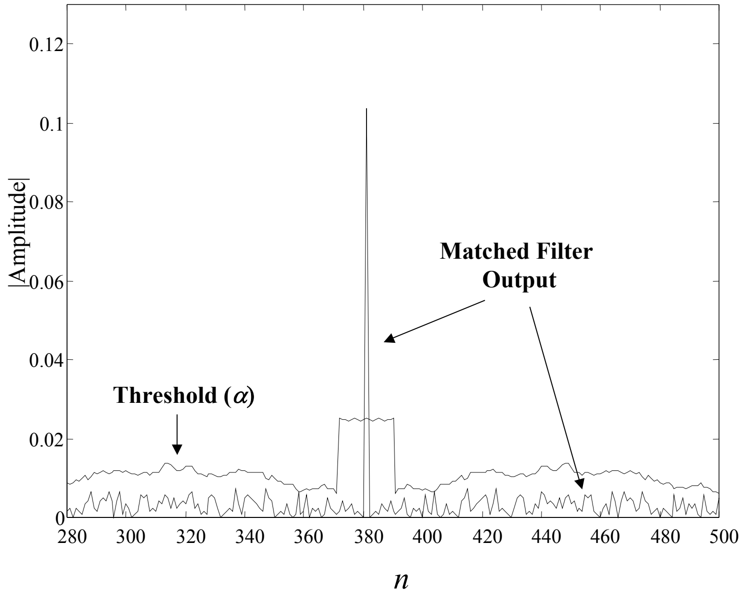

Figure 2-14. Local Average Threshold in Vicinity of Weak Target, *TB* = 127, *a* = 3.5, *b* = 9

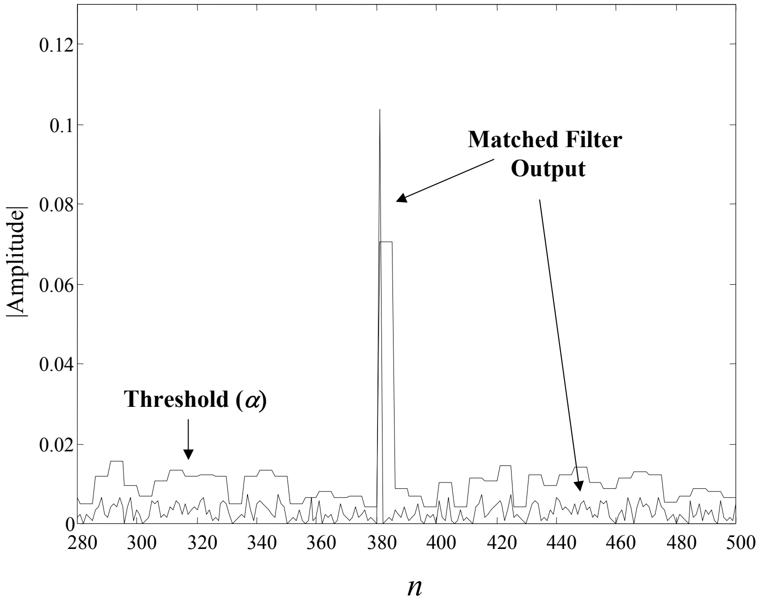

Figure 2-15. Locally Constant Threshold in Vicinity of Weak Target, *TB* = 127, *a* = 3.3, *K* = 5

To assess the impact of different parameters on locally constant threshold performance, it is helpful to fix one parameter and determine MSE performance as the other is varied. Figure 2-16 shows the locally constant threshold MSE for *TB* = 127, fixed subinterval length *K*, and varying scaling constant *a*. The MSE rapidly approaches zero as *a* increases with the error being greatest for lower threshold values. Finding the correct *a* is not a trivial task. One means for computing *a* is by estimating the data variance. In a clutter-limited environment, this requires some assumptions about the probability distribution of the clutter. A second method is to employ feedback in a manner similar to automatic gain control. Both of these methods may require extensive data processing and were not explored as part of this work. As shown in Section 2.3.4.2, a computationally simple approach for providing comparable threshold estimation performance as the averaging methods is readily available.

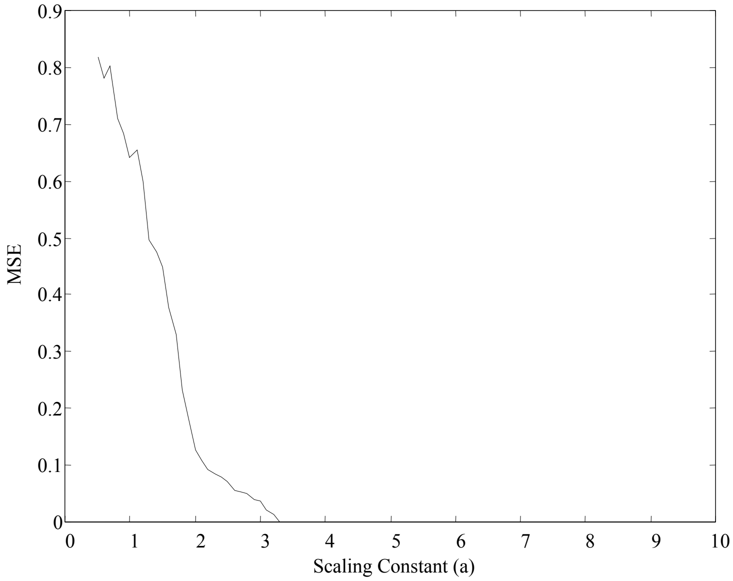

Figure 2-16. MSE vs. Scaling Constant *a* for Locally Constant Threshold, *TB* = 127, *K* = 5

The data in Figure 2-17 is the result of fixing *a* and varying *K*. The MSE generally increases with increasing *K* but many local minima and maxima occur. Figure 2-18 shows the same results for *K* = 0:10. The MMSE occurs for *K* = 5. Both figures clearly illustrate that the subinterval length should be small – on the order of a few samples. To suppress autocorrelation peaks, averaging three to five samples should be enough to set the threshold below the peak, assuming the scaling constant is set sufficiently high.

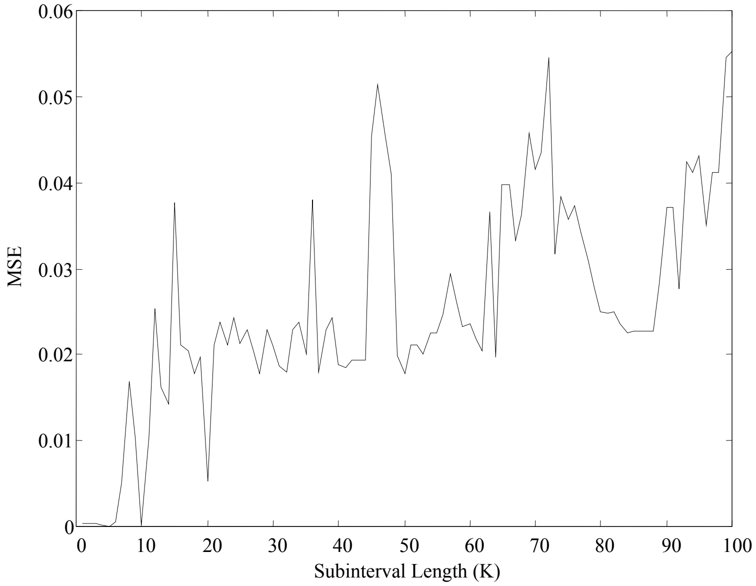

Figure 2-17. MSE vs. Subinterval Length *K* for Locally Constant Threshold, *TB* = 127, *a* = 3.3

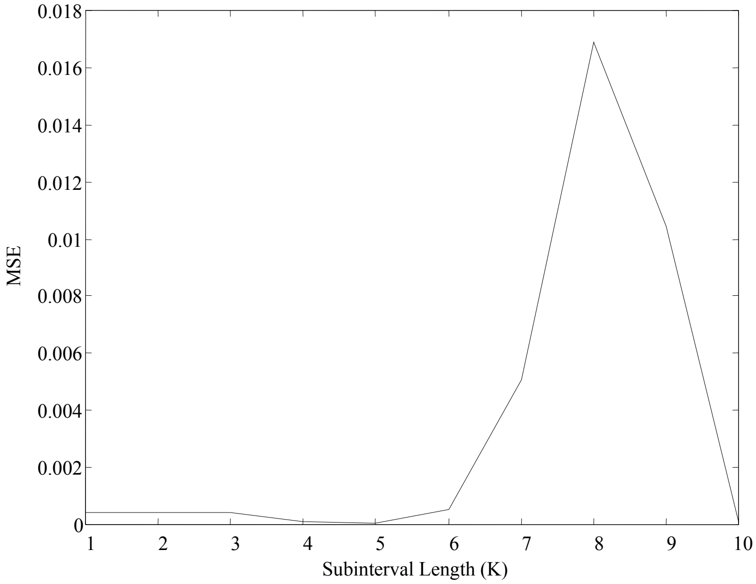

Figure 2-18. MSE vs. Subinterval Length *K* for Locally Constant Threshold *TB* = 127, *a* = 3.3, *K* = 0:10

2.3.4.2 Reserved Code Adaptive Thresholding

The reserved code adaptive thresholding exploits the crosscorrelation properties of good code families. Since the DET value is set above the maximum crosscorrelation level and ideally remains well below the autocorrelation peak, an alternative approach to data averaging involves threshold estimation based solely on code crosscorrelation characteristics. Unfortunately, the received data may contain responses from all transmitted pulse codes and any filter matched to one specific code may contain one or more autocorrelation peaks in its output.

The proposed adaptive thresholding solution involves reserving one code (from the family of pulse codes transmitted) to determine threshold characteristics. Given a set of M codes with good auto/cross-correlation properties, one of the codes may be reserved (not transmitted) and used for adaptively "training" the thresholding process. For example, if $M = 5$ only four codes are used to encode the transmitted waveform. For each NLS element, two matched filters are formed, as shown in Figure 2-19. The first filter is matched to the m^{th} pulse code being suppressed, resulting in compressed pulses for that code. The second filter is matched to the r^{th} (5^{th} in this case) reserved code and its output only consists of dispersed data, i.e., no autocorrelation peaks are possible/ present since the fifth code was not transmitted. If crosscorrelation levels and properties are consistent for all code pairs of the set, the adaptive threshold determined from the r^{th} matched filter will closely track the output of the first matched filter, except where autocorrelation peaks occur. By dividing the received data into intervals, as with locally constant thresholding approach, the threshold level in each interval may be determined as the maximum value of the second matched filter over that interval.

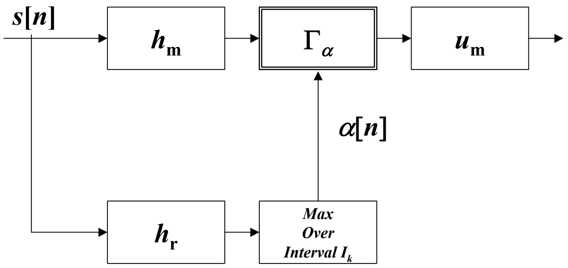

Figure 2-19. Reserved Code Adaptive Thresholding

Figure 2-20 shows results for reserved code thresholding using the previous example. In this case, the MMSE was 0.0181 for a subinterval length of $K = 54$ and for $TB = 127$, which is somewhat greater than the best results obtained with the local average thresholding method. However, the computational advantage of the reserved code technique is clear. By fixing the subinterval length, the only processing requirements are matched filtering and maximum value determination over every interval of interest. Determination of an optimal scaling constant is not required, as with the three averaging methods. The primary disadvantage lies in the inherent dependence of auto-/cross-correlation properties on the number of codes in the set. Increasing the number of required codes by one, as required for holding one in reserve, generally results in larger auto-/cross-correlation sidelobe levels, as will be shown in Chapter 3.

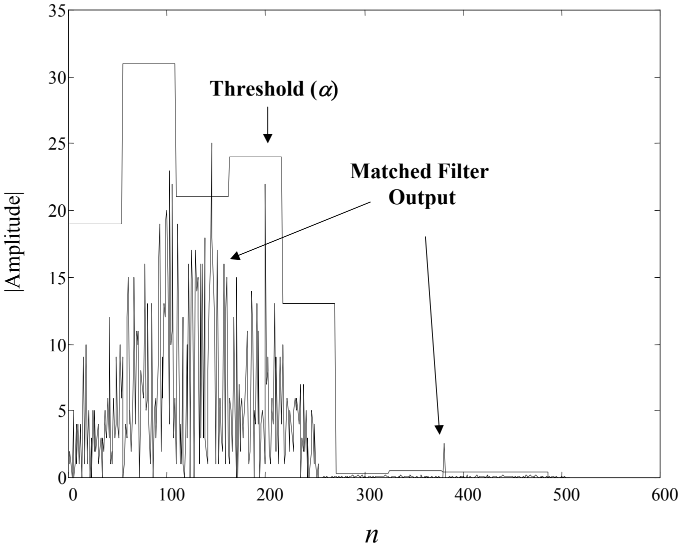

Figure 2-20. MMSE Reserved Code Threshold

The suitable length of the subinterval is dependent upon the probability that the actual crosscorrelation between two codes will exceed the threshold. In Figure 2-21, the estimated probability of threshold crossing is shown for three transmitted codes and one reserved code, *TB* = 127, by counting the number of threshold crossings for each crosscorrelation as a function of the subinterval length. Since the output of the matched filter has duration 2*TB*, dividing the number of crossings by 2*TB* provides an estimate of the probability that the threshold will be crossed. As shown in Figure 2-22, the MSE closely tracks the probability of threshold crossing, decreasing with increasing *K*. Unlike the averaging approaches, the performance improves for larger values of *K*.

Since the threshold yielding the MMSE for each case appears to be a dispersed envelope threshold, which closely follows the dispersed-code level, it is conjectured that in the point target case the DET is optimal, given the optimality criteria is based on MSE.

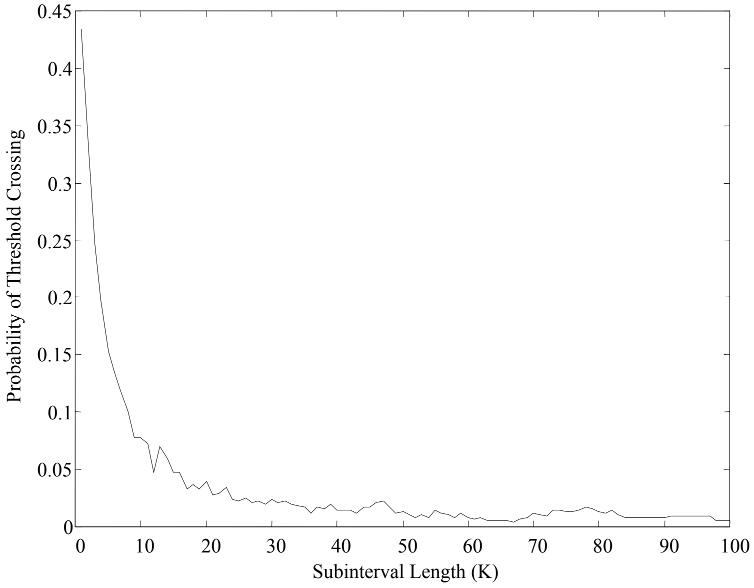

Figure 2-21. Estimated Probability of Threshold Crossing for Reserved Code Threshold, *TB* = 127

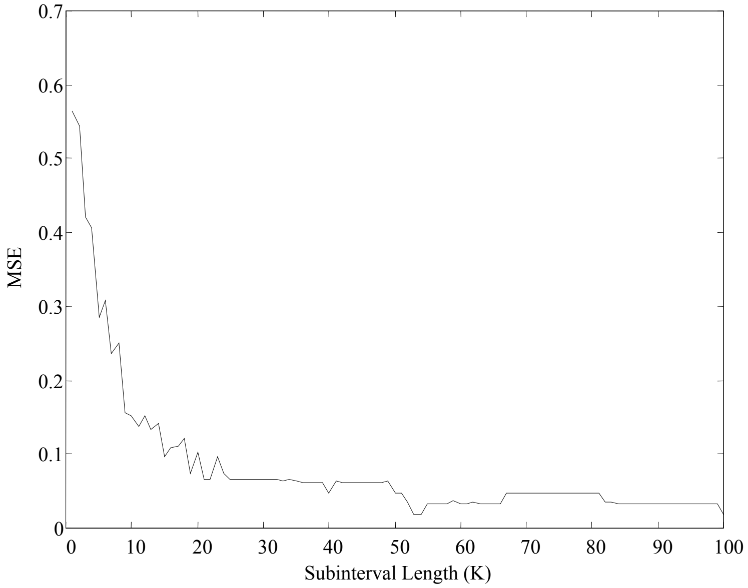

Figure 2-22. MSE vs. Subinterval Length, Reserved Code Thresholding, *TB* = 127

3. Pulse Code Selection

The radar range equation illustrates the dependence of detectable range on received energy. Much of the rapid advancement in radar performance during World War II was the result of improvements in the peak power of transmitter tubes, while short pulses were used to provide sufficient range resolution [24:746]. However, achievable peak power levels were limited and increasing the average power required wider pulse widths, resulting in poorer range resolution [25:10].

An early solution, as first proposed during WWII, was to increase the pulse bandwidth by linearly sweeping the carrier [26]. This technique became known as chirp or Linear Frequency Modulation (LFM). However, this technique was impractical at that time due to the incoherent nature of existing transmitter tubes. The general technique of increasing pulse bandwidth to improve range resolution while transmitting the pulse for a longer time duration (and hence more energy) is known as pulse compression.

Most radar pulse coding is done for the sole purpose of achieving the benefits provided by pulse compression. Exceptions include the use of frequency modulation for ranging applications, e.g., continuous wave and high PRF radar, and the use of coded pulse trains to increase Doppler resolution. Optimal coding is based on criterion such as measurement errors, detection performance, and false alarm probability. These criteria have traditionally placed certain restrictions on code selection. Consequently, the diverse pulse coding techniques investigated as part of this research are rarely found in radar literature – the repeated use of a single pulse code has met most optimality requirements for traditional applications and identically coded pulse trains have been used to demonstrate greatly enhanced Doppler processing.

For the NLS work of this research, diverse pulse coding techniques are required to ensure target responses from individual pulses are distinguishable from one another. This inherently requires the generation of code families possessing good auto- and cross-correlation properties. As will be shown, such properties are often mutually exclusive. With the exception of Brown codes, the emphasis in this chapter is on discrete code generation and performance characterization. Digital signal processing capabilities and the relative ease by which NLS concepts can be tested with discrete coding techniques provided the primary impetus for the discrete code investigation.

The metrics commonly used to quantify the suitability of a particular code (or code family) for radar applications are the Peak Autocorrelation Sidelobe Level (PSL), Integrated Autocorrelation Sidelobe Level (ISL), and Peak Crosscorrelation Level (PCCL) [22:537,32:754]. The ISL was introduced in Chapter 2. These metrics are usually stated in decibels, and normalized by the square of the peak response. The discrete aperiodic correlation function, C_{mn}, is defined by Eq (A.35).

$$ISL = 10\log\left\{ \frac{\sum\limits_{\substack{l=N-1 \\ l\neq 0}}^{N-1} \left|C_{mm}(l)\right|^2}{\left|C_{mm}(0)\right|^2} \right\} . \tag{3.1}$$

$$PSL = 10\log\left\{ \frac{\max\left\{\left|C_{mm}(l)\right|^2 ,\ \left|l\right| \in [1, N-1]\right\}}{\left|C_{mm}(0)\right|^2} \right\} . \tag{3.2}$$

$$PCCL = 10\log\left\{ \frac{\max\left\{\left|C_{mn}(l)\right|^2 ,\ m\neq n\right\}}{\max\left\{ \left|C_{mm}(0)\right|^2 ,\left|C_{nn}(0)\right|^2 \right\}} \right\} . \tag{3.3}$$

For discrete codes, the unnormalized maximum autocorrelation and crosscorrelation levels are also useful, as will be shown in Section 3.2 when correlation bounds for discrete codes are introduced.

3.1 Types of Radar Codes

3.1.1 Frequency Modulation Coding

Frequency modulation may be either linear (LFM) or nonlinear (NLFM). LFM is perhaps the simplest and most widely used pulse compression technique. An LFM pulse may be either actively generated using a linearly swept oscillator or passively generated using dispersive delay devices. Highly reliable dispersive devices are readily available, and may provide very high compression ratios. Examples include ultrasonic delay lines, waveguides operated near cutoff, and optical devices [22: 589].

The autocorrelation function of an LFM pulse is shown in Figure 3-1. As indicated, the Peak Sidelobe Level (PSL) is approximately –13 dB, which can be further reduced using spectral shaping and/or sidelobe weighting. However, these reduction techniques typically result in degraded range resolution, lower S/N, or both. The range-Doppler coupling of LFM was demonstrated in Figure 1-8, which may be resolved using either a priori knowledge of range or Doppler or multiple LFM modulations [2]. However, the range-Doppler coupling results in a relative high Doppler tolerance. Doppler shifts result in a corresponding time shift while the SNR is only moderately degraded.

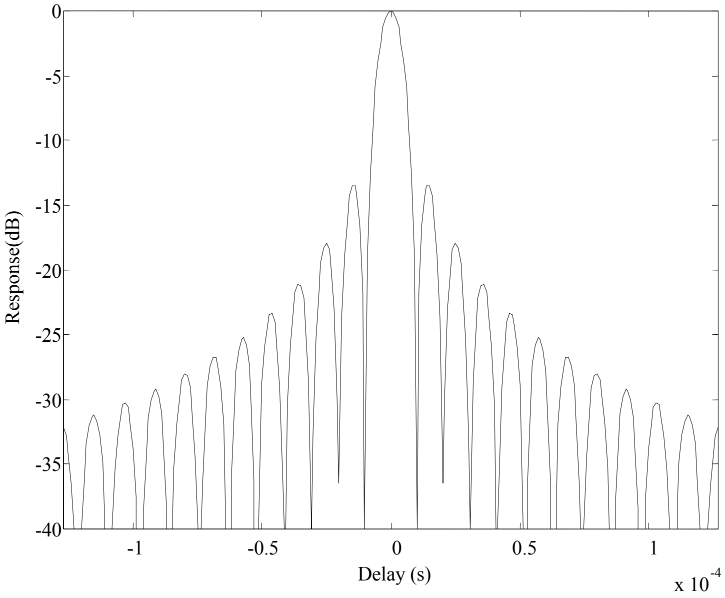

Figure 3-1. Autocorrelation of LFM Pulse for *TB* = 127

The original NLS implementation of Palermo, Leith, and Horgen was demonstrated utilizing two LFM waveforms with conjugate phase functions. The principle disadvantage of using LFM waveforms for NLS coding is that only two functions exist which have equivalent *TB* for a fixed pulse length. However, if the requirement is to suppress only one ambiguous range interval, LFM is a relatively simple and effective choice.

3.1.2 Binary Phase Coding

Binary phase (biphase) coding is limited to applying one of two discrete phase shift values, typically 0 or π, to a fundamental waveform. Binary sequences have been extensively researched and their performance characteristics are well understood. This is particularly true in the communications area where they currently play an important role in spread spectrum communications. The three most commonly used biphase codes for radar applications are the Barker, Minimum Peak Sidelobe (MPS), and pseudorandom codes.

Barker codes, as listed in Table 3-1, are representative of perfect codes having autocorrelation sidelobes with a magnitude of 1 or 0. Here, perfect simply implies a two-valued characteristic. There are no known Barker codes having a length greater than 13 which severely limits their use to low compression ratio applications.

Table 3-1. Known Barker Codes [22:538]

Length	Code Elements	PSL (dB)	ISL (dB)
1	+		
2	+ –, + +	-6.0	-3.0
3	+ + –	-9.5	-6.5
4	+ + – +, + + + –	-12.0	-6.0
5	+ + + – +	-14.0	-8.0
7	+ + + – – + –	-16.9	-9.1
11	+ + + – – – + – – + –	-20.8	-10.8
13	+ + + + + – – + + – + – +	-22.3	-11.5

MPS codes result from exhaustive computer searches that are seeking to find codes having the lowest possible autocorrelation sidelobes – there are no crosscorrelation constraints considered in determining MPS codes. To date, the maximum code length discovered for an MPS code is 69 [27]. Since MPS codes are not specifically designed to minimize crosscorrelation, they are not well suitable for NLS applications. However, their performance does provide an indication of achievable autocorrelation sidelobes limits for a given code length (less than 69).

Pseudorandom codes are widely used in digital communications. They are easily generated using various linear feedback shift register (LFSR) configurations and are well-suited for creating large code sets in real-time. The periodic autocorrelation and crosscorrelation functions of pseudorandom codes are well understood. However, their aperiodic crosscorrelation properties have not been extensively explored. As shown in the following sections, the properties obtained through periodic crosscorrelation that make pseudorandom codes desirable for multiple access communications, do not carry over into aperiodic crosscorrelation applications such as NLS processing and pulsed radar applications in general.

Nearly all pseudorandom codes are derived from Maximal Length Sequences (m-sequences), which are LFSR configurations operating to yield a maximum possible code period of $2^r - 1$ where r is the total number of register stages. M-sequences possess many interesting properties with the most useful being that the periodic autocorrelation function is two-valued, i.e., it is either 1 or $-1/N$ where N is the code period [28: 599]. Like Barker sequences, m-sequences represent perfect codes except that Barker codes are perfect for aperiodic correlation and m-sequences are perfect for periodic correlation.

Certain pairs of m-sequences are called preferred pairs. Preferred pairs are code pairs that yield a three-value periodic crosscorrelation function. Gold codes, a popular family of codes used for communication and navigation, are derived using preferred pairs of m-sequences. The chief advantage of Gold codes is the large number of codes in a set of given length ($N + 2$), and the three-value periodic crosscorrelation function [28:605].

3.1.3 Polyphase Coding

Polyphase codes are discrete codes used to yield possible waveform phase shift values of $2\pi k/N$, $k = 0, 1, \ldots N$, as opposed to binary codes which are limited to two phase values. Most polyphase coding is derived from LFM and yields waveforms with quadratic phase function. Like LFM, they have relatively high Doppler tolerance (compared to biphase codes) and good autocorrelation sidelobe properties [22:559].

For $\alpha = e^{j2\pi/N}$ and any positive integer N, Eqs (3.4) through (3.8) represent the best-known polyphase codes [29].

A. <u>Frank Sequence:</u>
$$f(km+n+1) = e^{j2\pi k(n/m)}, 0 \le i,\ n < m \text{ and } N = m^2 . \quad (3.4)$$

B. <u>Chu Sequence:</u>
$$c(k+1) = \begin{cases} \alpha^{k^2/2+ki} & N \text{ Even} \\ \alpha^{k(k+1)/2+qk} & N \text{ Odd} \end{cases} \quad \text{and q} \in \text{Integers} . \quad (3.5)$$

<u>*C. P3 and P4 Codes:*</u>

$$P3(k+1) = \alpha^{k^2/2} \ , \ 0 \le k \le N \ , \tag{3.6}$$

$$P4(k+1) = \alpha^{(k^2-kN)/2} \ , \ 0 \le k \le N \ . \tag{3.7}$$

D. <u>*Golumb Sequence:*</u>

$$g(k+1) = \alpha^{k(k+1)/2} \ , \ 0 \le k \le N \ . \tag{3.8}$$

The Chu, P3, P4, and Golumb sequences all possess the same absolute aperiodic autocorrelation function; they are equivalent except for a linear phase transformation [29:1001]. Like other radar codes, polyphase codes are specifically designed to yield optimal autocorrelation properties and no family of polyphase codes with optimal crosscorrelation properties are known.

3.2 Correlation Bounds

The best achievable code performance for NLS application may be determined using lower bounds of the aperiodic correlation function. Welch [30] and Sarwate [31] have determined these bounds for discrete, complex sequences. The aperiodic correlation function is defined in Eq (A.35).

Theorem 3 (Welch Bound) [30:398]. *Let P be a set of M pulse functions of length N. Define the Maximum Aperiodic Autocorrelation Sidelobe, C_a, as*

$$C_a = \max\left\{ \left|C_{nn}(l)\right| : u_n \in P \, , 1 \le l \le N-1 \right\} \tag{3.9}$$

and define the Maximum Aperiodic Crosscorrelation Level, C_c, as

$$C_c = \max\left\{ \left|C_{nm}(l)\right| : u_n \, , u_m \in P \, , n \ne m \, , 1-N \le l \le N-1 \right\} \ . \tag{3.10}$$

The Maximum Correlation value, C_{max}, of any two sequences in P is bounded by

$$\frac{C_{\max}^2}{N} = \max\left\{ \frac{C_a^2}{N} , \frac{C_c^2}{N} \right\} \ge \frac{N(M-1)}{(2NM-M-1)} \ . \tag{3.11}$$

Theorem 4 (Sarwate Bound) [31:723]. *Given definitions of Theorem 3, and for any set of M sequences of period N satisfying $C_{nn}(0) = N$ for all $n \in P$*

$$\frac{(2N-1)}{N}\left(\frac{C_c^2}{N}\right)+\frac{2(N-1)}{N(M-1)}\left(\frac{C_a^2}{N}\right) \geq 1 \ . \tag{3.12}$$

The Sarwate bound is more general than the Welch bound, since the latter provides a lower limit on the maximum level of any correlation, while the former establishes a concrete relationship between autocorrelation sidelobes and crosscorrelation levels. Welch and Sarwate bounds are plotted in Figure 3-2. The x-axis is the maximum aperiodic crosscorrelation level and the y-axis is the maximum aperiodic autocorrelation level. By calculating the maximum aperiodic correlation values C_a and C_c, the properties of any code set may be plotted as a point in two-dimensional space. The Welch bound is the shaded square area in the lower left-hand corner and provides a lower bound for the maximum of both correlation functions. The Sarwate bound is the straight line derived from the equation

$$\frac{\left(\frac{C_c^2}{N}\right)}{N/(2N-1)}+\frac{\left(\frac{C_a^2}{N}\right)}{N(M-1)/(2N-2)} = 1 \ . \tag{3.13}$$

Per Theorem 4, the point $\left(C_c^2/N, C_a^2/N\right)$ cannot lie below the Sarwate bound. The point where the Welch bound square touches the Sarwate bound line is the point at which both the maximum autocorrelation and maximum crosscorrelation are equal and optimum (for NLS application).

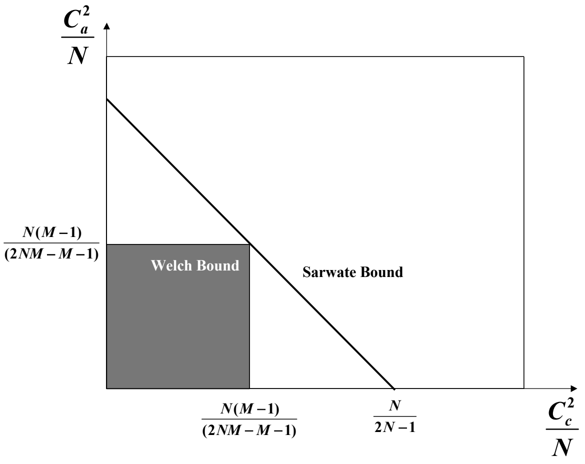

Figure 3-2. Sarwate and Welch Bounds [31:723]

The Sarwate bound establishes the qualitative principle that a code family with good aperiodic autocorrelation characteristics will have relatively poor aperiodic crosscorrelation characteristics. Likewise, a code family with good aperiodic crosscorrelation characteristics will have relatively poor aperiodic autocorrelation characteristics [31:720]. This relationship effectively limits the usefulness of known radar codes for NLS applications since such codes are normally optimized for autocorrelation properties.

3.3 Results for Well-Known Binary Codes

As a starting point for determining good code families for NLS applications, the aperiodic correlation characteristics of m-sequences and Gold codes were examined. Code lengths of $N = 31$, 63, 127, and 255 were evaluated using $M = 2$, 3, 4, and 5 codes. Although these particular code lengths may not provide sufficient time-bandwidth products for operational applications, their performance provides useful insight into comparative code performance that may be readily extended to larger code lengths.

3.3.1 M-Sequence Performance

M-sequence results are summarized in Table 3-2. These results are for illustrative purposes only and may not be indicative of best achievable code performance. In this case, initial shift register values were randomly chosen and only a few select polynomials were tested. As indicated by the C_a autocorrelation metric, autocorrelation properties do not vary significantly with the number of codes. This indicates the autocorrelation properties are nearly uniform and quite good. As indicated by the C_c crosscorrelation metric, crosscorrelation properties appear highly dependent upon code selection.

Table 3-2. M-Sequence Aperiodic Correlation Properties

Code Length (*N*)	Number of Codes (*M*)	C_a	C_c	PSL (dB)	ISL (dB)	PCCL (dB)
31	2	4	9	-17.8	-6.1	-10.7
31	3	5	10	-15.8	-9.8	-4.3
63	2	9	20	-16.9	-3.5	-10.0
63	3	9	20	-16.9	-4.5	-10.0
63	4	9	20	-16.9	-4.5	-10.0
127	2	10	23	-22.1	-5.0	-14.8
127	3	11	23	-21.2	-4.1	-14.8
127	4	11	44	-21.2	-5.6	-9.2
127	5	11	44	-21.2	-4.7	-6.2
255	2	18	37	-23.0	-4.5	-16.8
255	3	18	46	-23.0	-4.8	-14.9
255	4	18	55	-23.0	-4.7	-13.3
255	5	18	96	-23.0	-4.5	-8.5

3.3.2 Gold Code Performance

Gold Code results are summarized in Table 3-3. These results were obtained using randomly chosen codes from a family of ($N + 2$) codes. Comparison with m-sequence results shows that the code properties are generally much poorer, especially when comparing the autocorrelation properties. Also, much larger integrated sidelobe levels are indicated which will likely produce larger amounts of residual ambiguity (per Theorem 2).

Table 3-3. Gold Sequence Aperiodic Correlation Properties

Code Length (*N*)	Number of Codes (*M*)	C_a	C_c	PSL (dB)	ISL (dB)	PCCL (dB)
31	2	16	20	-5.7	3.8	-3.8
31	3	16	20	-5.7	4.0	-3.8
31	4	12	16	-8.2	0.7	-5.7
31	5	12	16	-8.2	0.7	-5.7
127	2	44	60	-9.2	7.5	-6.5
127	3	52	76	-7.8	8.7	-4.4
127	4	44	76	-9.2	8.7	-4.5
127	5	56	84	-7.1	8.6	-3.6

3.4 *Combinatorial Optimization*

Pseudorandom codes initially appeared promising for NLS application due to their wide use in multiple access communications. However, their aperiodic correlation properties do not mimic the periodic correlation properties that have made them attractive for communication applications. A few researchers have considered the need for diverse-pulse radar waveforms for multi-user ranging [32] and for low probability of intercept (LPI) signals [33]. Since no deterministic methods are known for generating good code sets with desirable aperiodic correlation characteristics, search algorithms have been employed to find codes with performance nearing the Sarwate bound. However, when considering M binary codes of length N, an exhaustive search algorithm must consider 2^N possibilities taken M at a time to search all possible codes, a task which is impractical for even modest code lengths [34].

Griep [32] and Deng [33] use a code selection approach based on simulated annealing (SA), a form of combinatorial optimization. Griep developed 4-phase polyphase codes along with optimum filters for code lengths up to 40, and for four users. Deng only developed binary codes. In this work, SA codes were generated for up to five “users” (range intervals for NLS), up to code lengths of 1023, and from 2 to 48 phases. Table 3-4 compares some results from this work (NLS) with Deng and Griep. For this particular code length, the NLS code is superior to the other codes. Other significant code lengths are unavailable from Griep, and further comparison with Deng shows similar results. Computational advantage is one reason behind this, since Griep published in 1995 and Deng in 1996.

Table 3-4. Caparison of Code Results with Griep[32] and Deng[33] for *TB* = 31

	Code	**PSL (dB)**	**PCCL (dB)**
NLS	48-Phase Length 31	-18.9	-16.9
Deng	Binary Length 31	-15.8	-11.8
Griep	4-Phase Length 31	-18.4	-11.9

Code selection via SA is based on physical annealing, i.e., a disordered material is cooled from a high to a low temperature state, seeking the low energy ground state [35]. In a similar fashion, the aperiodic auto- and crosscorrelation sidelobe levels can form an energy state that can be minimized.

3.4.1 Simulated Annealing (SA) Algorithm

Simulated annealing was first introduced by Kirkpatrick, Gelatt, and Vecchi at IBM in 1983, with the principle application being optimal computer design [36]. They expanded the Metropolis algorithm, invented in 1953, to a broader class of problems. The Metropolis algorithm works as follows [37:445]:

1. A description of possible system configurations is made. For coding this may be an N x M matrix of code elements.
2. A generator of random changes is required and presents various options to the system. In a matrix of binary codes, this may be a sign reversal of a random code element.
3. An energy function E is evaluated with the overall objective of the algorithm being the minimization of E.
4. A control parameter T (analogous to physical temperature) and an annealing schedule are used to control the rate of "cooling."
5. At every state change, new energy E_2 is compared to previous energy E_1. If, $E_1 < E_2$ the state change is accepted. Otherwise, the state change is conditionally accepted with probability (based on Boltzmann's Equation)

$$p = e^{-(E_2 - E_1)/kT} \quad . \tag{3.14}$$

To find good codes for NLS applications, the following composite energy function was used

$$E = w_1 C_a + w_2 C_c \tag{3.15}$$

where C_a and C_c are the maximum autocorrelation and crosscorrelation values, respectively, and w_1 and w_2 are weights for assigning a relative level of importance to each correlation during the minimization process.

For this work, the annealing schedule, initial temperature, and equilibrium determination were empirically determined. In the initial "hot" state, the energy fluctuates rapidly, preventing the system from falsely stabilizing at a local minimum. As the temperature is lowered, fewer and fewer acceptances of higher energy values occur.

For demonstration purposes, SA results for random binary and polyphase codes are presented in the next section. The algorithm developed is easily adaptable to permit polyphase code generation; rather than using a matrix of only ones and minus ones, the polyphase matrix simply consists of integers between zero and K, where K is the number of desired phase values. Experimentation shows that the complex computation required for the energy function of Eq 3.12, as well as the increase in the number of possible values of each code element from two to K, greatly increases the required computation time to convergence on an acceptable solution.

3.4.2 Simulated Annealing Results

Simulated annealing results for binary codes are summarized in Table 3-5. Table 3-6 summarizes the maximum autocorrelation level and maximum crosscorrelation for all three binary codes. A visual representation of code performance is shown in Figure 3-3 through Figure 3-6, and based on Figure 3-2. Maximum correlation properties of each code are plotted in the normalized (C_c^2/N, C_a^2/N) coordinate space. In all cases, circles (○) represent SA codes, squares (□) represent m-sequences, and triangles (Δ) represent Gold codes. Each plot is for one value of M (number of codes) and all values of N (code length) computed in the previous sections, i.e., $N = 31$, 63, 127 and 255. The Sarwate bound is plotted in the lower left corner.

In some cases, Gold code markers do not even appear on the plots, giving a clear indication of how poor their relative performance is. Generally, m-sequences possess equal or better autocorrelation properties than SA derived codes. However, as indicated by data in the figures, the SA derived code performance is closer to the Sarwate bound. The SA-codes have superior cross-correlation performance for all code lengths, as demonstrated by the small values of C_c in Table 3-6.

Table 3-5. SA Generated Binary Codes: Aperiodic Correlation Properties

Code Length (N)	Number of Codes (M)	C_a	C_c	PSL (dB)	ISL (dB)	PCCL (dB)
31	2	5	7	-15.8	-3.5	-15.8
31	3	6	8	-14.3	-2.1	-11.8
31	4	7	8	-12.9	-2.2	-11.8
31	5	6	10	-14.2	-2.3	-9.8
63	2	10	10	-16.0	-1.8	-16.0
63	3	9	12	-16.9	-3.3	-14.4
63	4	9	14	-16.9	-2.0	-13.1
63	5	9	14	-16.9	-2.1	-13.1
127	2	13	16	-19.8	-3.3	-18.0
127	3	14	18	-19.2	-2.6	-17.0
127	4	13	21	-19.8	-2.9	-15.6
127	5	15	21	-18.6	-2.3	-15.6
255	2	22	22	-21.3	-1.16	-21.3
255	3	26	30	-19.8	-0.7	-18.6

Table 3-6. Comparison of Maximum Autocorrelation (C_a) and Maximum Crosscorrelation (C_c) Values for SA Generated Codes , M-Sequences, and Gold Codes

		SA		*m*-sequence		Gold	
Code Length (*N*)	**Number of Codes (*M*)**	C_a	C_c	C_a	C_c	C_a	C_c
31	2	5	7	4	9	16	20
31	3	6	8	5	10	16	20
31	4	7	8	N/A	N/A	12	16
31	5	6	10	N/A	N/A	12	16
63	2	10	10	9	20	N/A	N/A
63	3	9	12	9	20	N/A	N/A
63	4	9	14	9	20	N/A	N/A
63	5	9	14	N/A	N/A	N/A	N/A
127	2	13	16	10	23	44	60
127	3	14	18	11	23	52	76
127	4	13	21	11	44	44	76
127	5	15	21	11	44	56	84
255	2	22	22	18	37	N/A	N/A
255	3	26	30	18	46	N/A	N/A

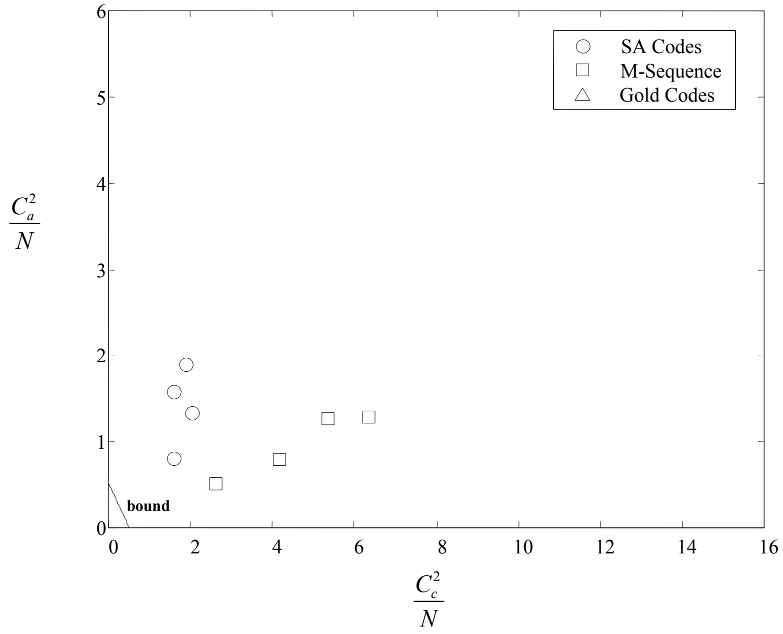

Figure 3-3. Maximum Aperiodic Correlation Results for $M = 2$ Codes. The Sarwate Bound Appears in the Lower Left-Hand Corner

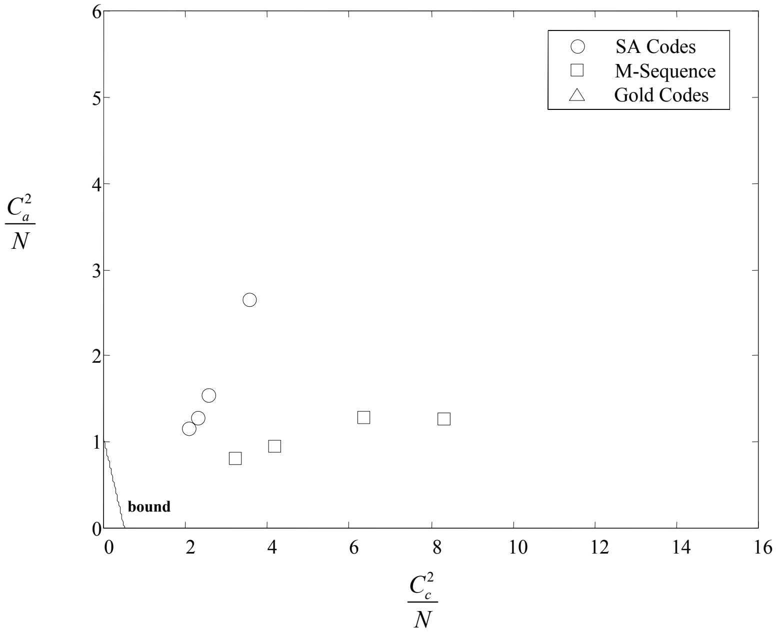

Figure 3-4. Maximum Aperiodic Correlation Results for *M* = 3 Codes. The Sarwate Bound Appears in the Lower Left-Hand Corner

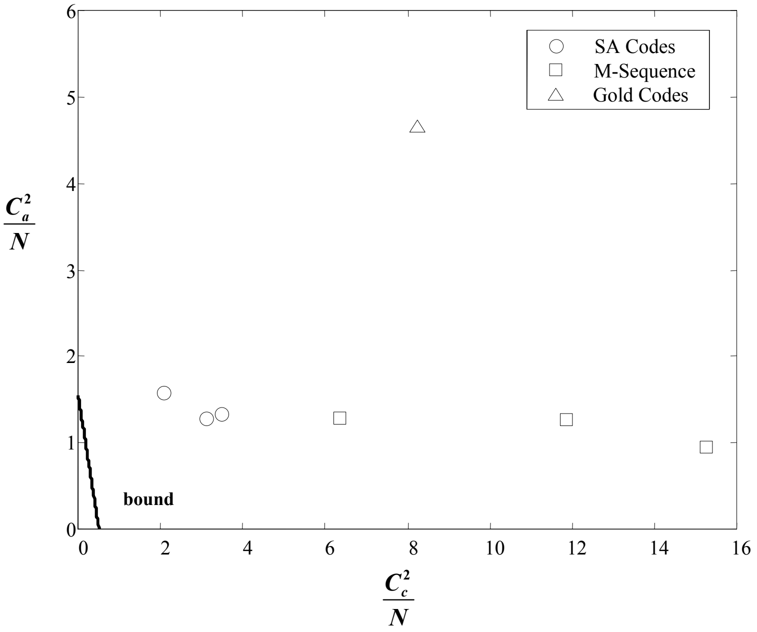

Figure 3-5. Maximum Aperiodic Correlation Results for *M* = 4 Codes. The Sarwate Bound Appears in the Lower Left-Hand Corner

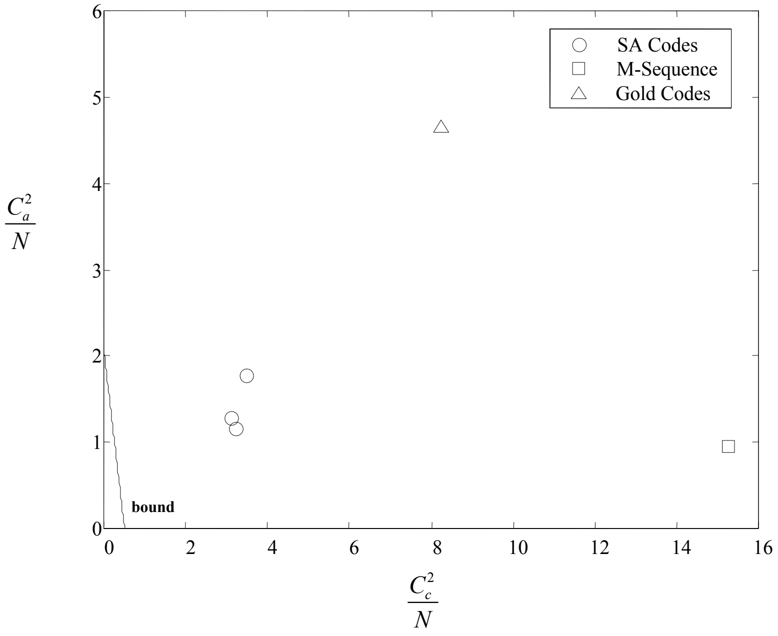

Figure 3-6. Maximum Aperiodic Correlation Results for *M* = 5 Codes. The Sarwate Bound Appears in the Lower Left-Hand Corner

Although better binary SA codes are likely possible, simply by employing more computer time, polyphase coding is more likely to yield performance closer to the Sarwate bound since it was derived for complex sequences. This is illustrated in Figure 3-7 where 4, 8, 16, 32, and 48-phase correlation maximums are plotted for comparison with binary SA and m-sequence codes. All data is for codes of length 31 with two codes per set. Clearly, the polyphase code performance moves closer to the Sarwate bound as the number of phase values increase. This provides strong evidence that the SA approach may yield near-optimum codes for NLS applications.

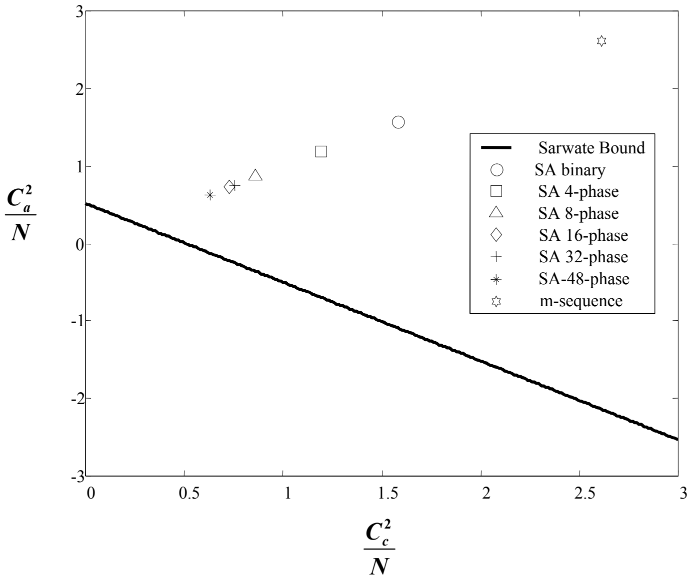

Figure 3-7. Polyphase Coding: Maximum Aperiodic Correlation Results for *M* = 2 Codes and *TB* = 31. The Sarwate Bound Is Line On the Lower Left

3.5 *Mutually Dispersive Brown Codes*

Although not considered as an integral part of this research, the theory behind mutually dispersive Brown coding is presented for completeness. Brown [38] has developed a mutually dispersive coding theory for generating optimal codes for NLS applications. Brown's approach for optimizing code selection is two-fold. First, the optimum autocorrelation function is found using calculus of variations to minimize the root-mean-square time duration of Eq (1.16). This process optimally yields a cosine taper, similar to techniques used in antenna sidelobe reduction.

Secondly, the crosscorrelation properties of code families are optimized by defining phase-rate functions, obtained by taking the derivative of corresponding phase modulation functions in the frequency domain. The phase-rate functions are optimized by finding *M* "hermits" in *M*-dimensional space, i.e., equidistant locations in the *M*-Dimensional solution space having maximum separation distance. The hermit locations and an orthogonal basis are subsequently used to develop a set of optimal phase-rate functions for obtaining a set of mutually dispersive codes. The corresponding time domain codes are obtained by integrating the phase-rate functions and applying an inverse Fourier transform.

Brown has designed generalized chirp (LFM) codes having linear frequency modulation over a specific range, but are nonlinear in general. Practical implementation of Brown's mutually dispersive codes is currently under investigation, with the technique possibly allowing for deterministic selection of optimal codes for future NLS applications.

4. Performance of Nonlinear Suppression in Real Clutter

4.1 Nonlinear Suppression of Ground Clutter

General ground clutter characteristics for airborne radar applications were presented in Chapter 1. This chapter examines the effectiveness of NLS in suppressing ambiguous clutter. For most airborne radar systems, ground clutter, rather than noise, is the limiting factor in target detection. Most modern radar research, e.g., space-time adaptive processing (STAP), is concerned with improving clutter suppression. NLS is not envisioned as replacement for such techniques. Rather, the primary role of NLS is viewed as one of augmentation and effectiveness enhancement. In a high or medium PRF systems, where range ambiguities may be significant or severe, the NLS technique proposed here is expected to complement other clutter suppression techniques, further improving their performance by suppressing ambiguous clutter responses.

Effective NLS performance requires discrimination of compressed pulse responses from dispersed pulse responses within each elemental suppression operation. If for example, the clutter return is Gaussian distributed, perhaps due to the central limit theorem, the matched filter output is also Gaussian since matched filtering is inherently a linear operation. In this case, the compressed (focused) signal will be devoid of distinct "spikes" and subsequent hole punching will be ineffective. Even for high range resolution radar, where the backscatter coefficient may have non-Gaussian distribution, such as a lognormal or Weibull distribution, the superposition of pulse responses from a large number of clutter cells may yet yield Gaussian clutter.

The backscatter coefficient, though often modeled using a distribution function, is highly dependent upon many environmental factors, including, the homogeneity or nonhomogeneity of the medium, the angle of incidence, the surface roughness, the surface moisture, the vegetation type, the presence of ice or snow, and the presence of strong point scatterers [39:21-33].

Ayasli [40] shows that even for a simple backscatter model such as the constant-γ model, propagation effects alone can explain the large spread in observed clutter strength and variations with respect to frequency. Propagation effects result from the earth's curvature and refraction, surface roughness, and multipath [41]. Ulaby [39:25-26], when demonstrating the angular dependence of the backscatter coefficient for a random surface, divides the plot of backscatter vs. incidence angle into three regions: the quasi-specular region, the plateau region and the shadow region, with the latter being the least understood.

Propagation effects may largely account for the nature of real clutter. Given typical engagement geometry for an airborne radar system, mainbeam clutter often results from clutter cells at lower surface grazing angles (larger incidence angles). This is the region where Ulaby's "shadow region" is defined. Smith [42] shows that a shadowing function, dependent upon grazing angle, can be used to effectively model observed backscatter from rough surfaces.

4.2 NLS Clutter Testing Methodology

The primary objective of NLS clutter testing is to determine how effective the proposed NLS technique is at suppressing ambiguous clutter and to measure (quantify) the degree of suppression for various coding. In support of this objective, an evaluation model for the hole-punching nonlinearity and various performance metrics were developed to quantify performance. The measured clutter data used for performance evaluation was obtained from actual flight tests and was artificially prepared for NLS performance demonstration and characterization.

4.2.1 NLS Performance Evaluation Model

The evaluation model developed for NLS clutter suppression performance testing is shown in Figure 4-1. For NLS testing, two distinct range intervals of clutter data are coded with unique pulse codes, one of the resulting signals is designated as the ambiguous signal (s_A), and the other is designated as the unambiguous signal (s_U). This particular approach to performance testing is feasible because the ambiguous clutter situation is "artificially" created by uniquely encoding and folding-over measured data from two distinct range intervals – in a real-world situation, the ambiguous and unambiguous signals are completely inseparable.

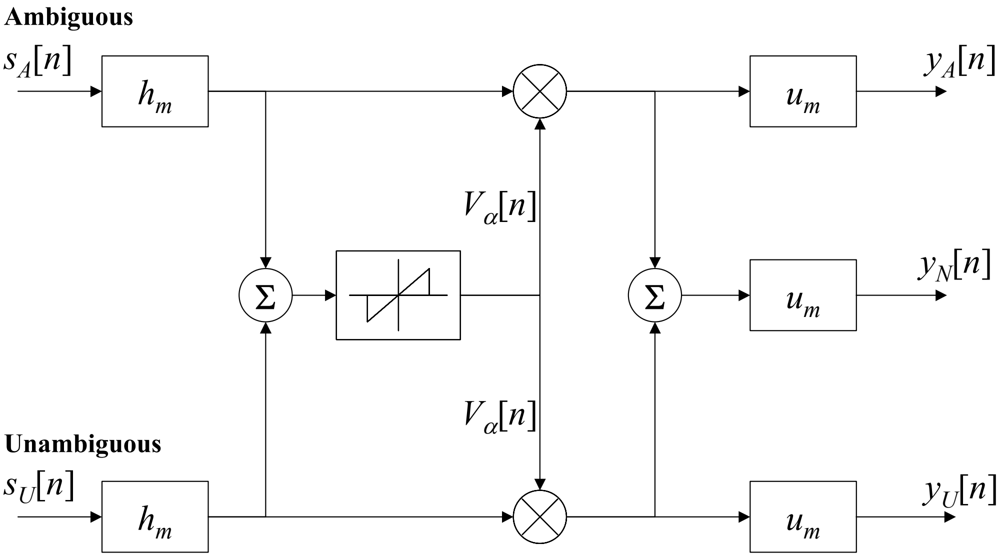

Figure 4-1. NLS Clutter Evaluation Model for Hole-Punching Nonlinearity

As illustrated, the ambiguous and unambiguous signals are applied to matched filter, h_m, which is matched to the ambiguous signal, s_A. Since the unambiguous data signal is known, a "near optimum" threshold is easily computed based solely on the dispersed signal response

$$\alpha[n] = a \cdot \left| s_U[n] * h_m[n] \right| \tag{4.1}$$

where a is a scaling constant. Once threshold $\alpha[n]$ is determined, the hole-punch operation may be independently applied to the unambiguous and ambiguous signals by creating a hole-punch vector, V_α, given by

$$V_\alpha = \begin{cases} 0 & \text{if } \left| s_A[n] + s_U[n] \right| > \alpha[n] \\ 1 & \text{otherwise} \end{cases} \quad . \tag{4.2}$$

Thus, the hole-punch vector V_α is a combination of ones and zeros with each zero location representing a specific signal component to be nulled. Denoting element-by-element multiplication by $\otimes$, the ambiguous output, y_A, and unambiguous output, y_U, are given by

$$y_A[n] = u_m * \left\{ V_\alpha[n] \otimes \left(s_A[n] * h_m[n] \right) \right\} \ . \tag{4.3}$$

$$y_U[n] = u_m * \left\{ V_\alpha[n] \otimes \left(s_U[n] * h_m[n] \right) \right\} \ .$$

The combined output, which is equivalent to an operational NLS channel output (as opposed to the separate data "streams" created in the evaluation model for performance characterization), is given by

$$y_N[n] = u_m * \left\{ V_\alpha[n] \otimes \left(s_A[n] * h_m[n] \right) + V_\alpha[n] \otimes \left(s_U[n] * h_m[n] \right) \right\} \ . \tag{4.4}$$

From the evaluation model, several useful performance evaluation metrics are created. The first metric is a power ratio between the unambiguous output $y_U[n]$ and the ambiguous output $y_A[n]$, given by

$$\frac{P_u}{P_a} = \frac{\sum_{n=0}^{N-1} \left| y_U[n] \right|^2}{\sum_{n=0}^{N-1} \left| y_A[n] \right|^2} \ . \tag{4.5}$$

Additional metrics for NLS performance testing requires implementing the model of Figure 4-1 in two different configurations. The first configuration (normal configuration), as described above, uses the actual computed threshold value, i.e., $T = \alpha$. The second configuration uses an infinite threshold, $T = \infty$, which is equivalent to setting the hole-punch vector to all ones. The infinite threshold configuration is used to produce an output that is "colored" by the filter responses – identical filter coloration as in the first configuration but without any suppression effects. Several additional power ratios and a mean-square error (MSE) metric are computed using both configurations, as shown in Figure 4-2.

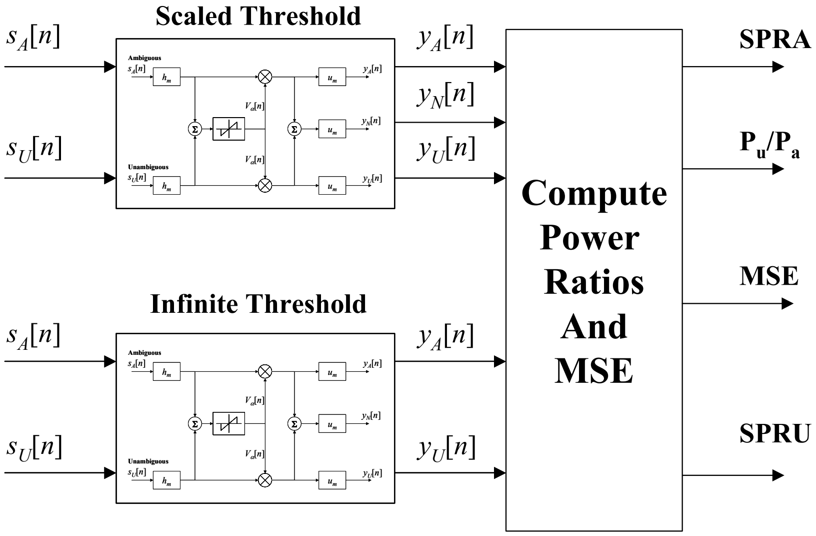

Figure 4-2. Power Ratio and MSE Computations Using Scaled ($T = \alpha$) and Infinite ($T = \infty$) Configurations

The *Suppressed Power Ratio-Ambiguous* (SPRA) is the ratio of ambiguous output power from the normal ($T = \alpha$) configuration to ambiguous output power from the infinite ($T = \infty$) threshold configuration, expressed as

$$\mathrm{SPRA} = \frac{P_a\big|_{T=\alpha}}{P_a\big|_{T=\infty}} = \frac{\sum_{n=0}^{N-1}\left| y_A[n]\big|_{T=\alpha}\right|^2}{\sum_{n=0}^{N-1}\left| y_A[n]\big|_{T=\infty}\right|^2} \quad . \tag{4.6}$$

The SPRA represents the amount of ambiguous (undesired) power suppressed by the NLS operation.

The *Suppressed Power Ratio-Unambiguous* (SPRU) is the ratio of unambiguous output power from the normal ($T = \alpha$) configuration to unambiguous output power from the infinite ($T = \infty$) threshold configuration

$$\mathrm{SPRU} = \frac{P_u\big|_{T=\alpha}}{P_u\big|_{T=\infty}} = \frac{\sum_{n=0}^{N-1}\left| y_U[n]\big|_{T=\alpha}\right|^2}{\sum_{n=0}^{N-1}\left| y_U[n]\big|_{T=\infty}\right|^2} \quad . \tag{4.7}$$

The SPRU represents the amount of unambiguous (desired) power suppressed by the NLS operation.

The MSE metric characterizes how much the suppressed output "looks like" the colored unambiguous output. The error is derived from the combined output from the normal configuration, $y_N[n]|_{T=\alpha}$, and the unambiguous output from the infinite configuration, $y_U[n]|_{T=\infty}$, as

$$MSE = \frac{\frac{1}{N}\sum_{n=0}^{N-1}\left|\beta\, y_N[n]\big|_{T=\alpha} - C_1 - y_U[n]\big|_{T=\infty} + C_2\right|^2}{\frac{1}{N}\sum_{n=0}^{N-1}\left| y_U[n]\big|_{T=\infty}\right|^2} \tag{4.8}$$

where β is a scaling constant and C_1 and C_2 are bias constants.

For analysis, the scaling constant for normal thresholding varies from 0.5 to 3.0 and P_u/P_a is computed. The MSE is also computed as a function of the scaling constant. The "best" scaling constant is determined as the value providing the maximum value of P_u/P_a. The MSE, SPRA, and SPRU metrics are then determined using this value of the scaling constant.

4.2.2 Preparation of Real Clutter Data for NLS Processing

Lacking an existing radar system capable of transmitting diverse-pulse waveforms, a method was sought for converting existing measured clutter data into diversely coded, ambiguous clutter data. The real clutter data used in this work is from the Multi-Channel Airborne Radar Measurement (MCARM) Flight Test program. Table 4-1 lists parameters of the MCARM program, including platform and radar parameters used for testing [43].

Table 4-1. MCARM Parameters

Parameter	Value
Aircraft Altitude	3.49 km
Carrier Frequency	1.29 GHz
Aircraft Ground Speed	100 m/s
Array Type	Side-Looking Linear Array
Number of Elements	44 (11 Azimuth, 4 Elevation)
Azimuth Element Spacing	0.1092 m
Elevation Element Spacing	0.1407 m
Azimuth Beamwidth	7.5 deg
Elevation Beamwidth	23.6 deg
Azimuth Pointing Angle	0.895 deg
Elevation Pointing Angle	5 deg
Number of Range Gates per PRI	630
PRF	1984 Hz
Pulse Width	50.8 μs
Sample Time	0.8 μs
Number of Pulses per CPI	128

The MCARM data is stored in complex MATLAB® format. Each file consists of data collected over one CPI. Since the MCARM data is primarily used for evaluating adaptive beamforming algorithms, the files include output data for 24 receiver channels, each of which corresponds to the output of different array sub-apertures. Before using the data for NLS processing, eleven channels are coherently combined using appropriate steering vectors and Doppler processing is applied using a fast Fourier transform (FFT). Only the zero-Doppler data is used for this research since this case represents the majority of the clutter power received for a side-looking array.

Each PRI of MCARM data consists of 630 complex samples. The zero-Doppler channel output for one PRI of MCARM data is shown in Figure 4-3. The exact nature of the large peak in the data near the beginning of each PRI is uncertain. However, this portion of the data is not processed and it is therefore inconsequential to ignore. The sidelobe clutter response occurs in the first half of each PRI and is over 40 dB greater than the clutter response seen in the second half of the PRI. Therefore, only the second half of each PRI is processed, as shown in Figure 4-4, yielding 315 complex samples for NLS processing and evaluation.

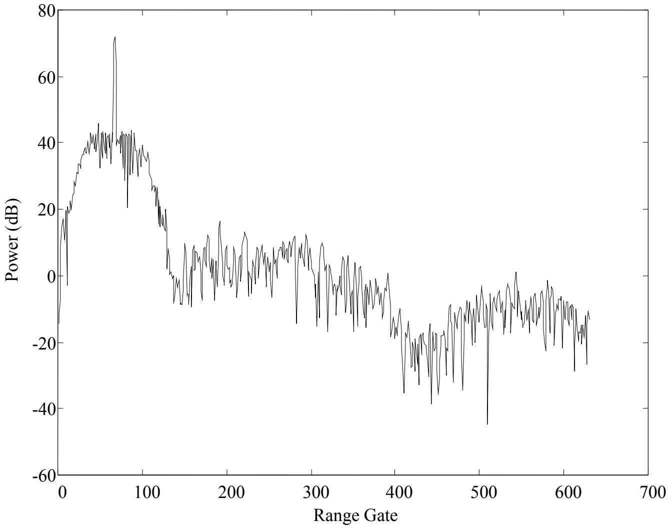

Figure 4-3. Zero-Doppler Power of MCARM Clutter Data, Single PRI

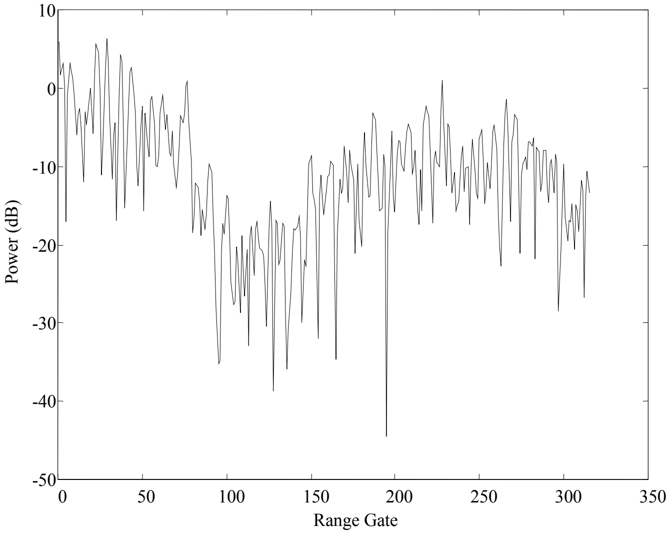

Figure 4-4. Zero-Doppler Power of MCARM Clutter Data, Second Half of PRI

The effect of Doppler processing prior to NLS is to reduce the cross-range resolution of the clutter cells. The range and cross-range resolution of the MCARM data may be determined from the given parameters. The range resolution is the length, in meters, of one range gate and is given by

$$\Delta R = \frac{cT_s}{2} \cong 120 \text{ m} \tag{4.9}$$

where T_s is the sample time (0.8 μs) and c is the speed of light. The cross-range resolution is found according to [44:445] and is given by

$$\Delta R_c = R_k \frac{\lambda}{2vT_{ob}\sin(\beta_k)} \tag{4.10}$$

where R_k and β_k are the range and incidence angle to the k^{th} clutter cell, v is the radar velocity, T_{ob} is the coherent processing time, and λ is the wavelength. The coherent processing interval, as computed from data in Table 4-1, is (128 pulses)/(1984 Hz), or 64.5 ms. The wavelength for a carrier frequency of 1.29 GHz is 0.232 m. The radar velocity is approximately 100 m/s. The first sample in the data used for NLS testing is at $n_1 = 315$ and the last sample is $n_2 = 630$. The ranges corresponding to these sample values (see Figure 4-5) are

$$\begin{aligned} R_1 &= \frac{cT_s n_1}{2} = 37.8 \text{ km} \\ R_2 &= \frac{cT_s n_2}{2} = 75.5 \text{ km} \end{aligned} \tag{4.11}$$

with corresponding incidence angles of

$$\begin{aligned} \beta_1 &= \cos^{-1}\left(\frac{h}{R_1}\right) = 84.7^\circ \\ \beta_2 &= \cos^{-1}\left(\frac{h}{R_2}\right) = 87.3^\circ \end{aligned} \tag{4.12}$$

where h is the radar altitude (3.49 km). Applying these results to Eq (4.10) yields an approximate cross-range resolution of 682.7 m at R_1 and 1359.3 m at R_2. Even with Doppler processing, the clutter cells for this particular data set are very large and the received clutter response consists of reflections from a large number of scatterers.

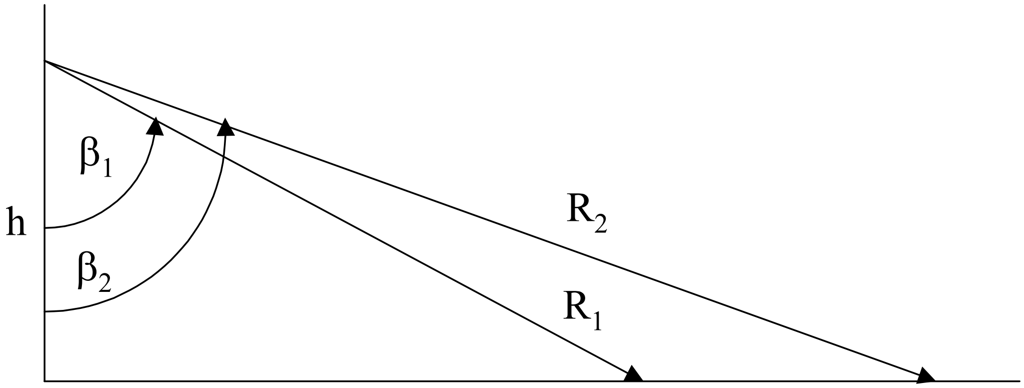

Figure 4-5. Ranges and Incidence Angles Corresponding to the First and Last Sample of the MCARM Data Used for NLS Testing

4.2.3 Pulse Codes Used For NLS Clutter Tests

Due to the small sample size of the MCARM data (315 samples), the codes used to evaluate NLS performance were limited to lengths of 31, 63 and 127. Although a code with a length of 255 was considered, it was experimentally eliminated because it was determined that the edge effects, near the beginning and end of the data block, actually resulted in degraded performance. A sampled LFM waveform was used to provide baseline performance of a "near optimum" (very low ISL levels) coding scheme and SA generated codes were tested for comparison. The PSL, ISL and PCCL properties for all tested codes are provided in Table 4-2.

Table 4-2. Code Properties for Codes used in NLS Clutter Tests

Code Length / Type	PSL (dB)	Max ISL (dB)	PCCL (dB)
31/LFM	-21.3	-9.3	-14.6
63 /LFM	-24.3	-10.9	-17.6
127 / LFM	-27.4	-12.5	-20.6
31/ 16-Phase SA	-18.4	-3.3	-16.6
63/ 16-Phase SA	-21.3	-3.3	-18.9
127/ 16-Phase SA	-22.8	-2.9	-20.3

As illustrated, the LFM codes possess excellent properties, especially very low ISLs for all three code lengths. The LFM codes are actually very much like Frank codes, which are based on sampling the phase of step-chirp waveforms and have peak sidelobe levels near – 30 dB [45:10]. The SA codes were specifically generated for optimum PSL and PCCL levels and thus have relatively poorer ISL levels. The LFM and SA codes have a comparable PCCL.

4.3 NLS Clutter Test Results

Using the six LFM/SA codes described in the previous section, performance testing was conducted for input P_u/P_a ratios of 0.0, -3.0, and –6.0 dB. Threshold scaling parameter a was varied from 0.5 to 3.0 with the maximum value of P_u/P_a used to determine the "best" value of a. The "best" value of a was used for calculating the MSE, the SPRA, and SPRU metrics. Comprehensive performance results are provided in Table B-1 with plots of output P_u/P_a and MSE vs. scaling constant a provided in Figure B-1 through B-36. Representative results for each P_u/P_a case follows.

4.3.1 Representative Performance Results for Input P_u/P_a of 0.0 dB

For this case, the unambiguous and ambiguous input signal powers are equal. Performance metrics are shown in Table 4-3.

Table 4-3. MCARM Test Results for Input P_u/P_a = 0.0 dB

Coding	Input P_u/P_a (dB)	Output P_u/P_a (dB)	Scaling Constant	MSE	SPRA (dB)	SPRU (dB)
31 LFM	0	3.7	1.24	0.659	-6.7	-2.8
63 LFM	0	4.2	1.38	0.571	-6.2	-2.4
127 LFM	0	5.5	0.99	0.702	-9.7	-4.7
31-16 SA	0	4.4	1.41	0.530	-7.8	-2.1
63-16 SA	0	3.0	1.21	0.638	-8.5	-4.2
127-16 SA	0	5.1	1.51	0.410	-8.2	-3.2

For all codes considered, the improvement from input P_u/P_a to output P_u/P_a was at least 3.0 dB. The apparent trend is increasing P_u/P_a for increasing TB, except for the 63-16 SA code, which produced a lower P_u/P_a. The amount of suppressed ambiguous clutter is reflected in the SPRA metric, which varied from –6.2 dB to –9.7 dB. The amount of suppressed unambiguous clutter is reflected in the SPRU metric, which varied from -2.1 dB to -4.7 dB. Effects of varying the scaling constant are clearly apparent;

lowering the threshold value (reducing *a*) resulted in greater suppression of both ambiguous and unambiguous clutter, while increasing *a* reduced the amount of total suppression.

For comparison purposes, metric plots for the 127 LFM and 127-16 SA codes are provided in Figure 4-6 through Figure 4-9. Although the maximum output P_u/P_a occurs for different threshold scaling constants, the resultant improvement is nearly 5.0 dB for both codes. However, the MSE is significantly lower for the 127-SA codes due to the higher scaling constant for which maximum output P_u/P_a occurs.

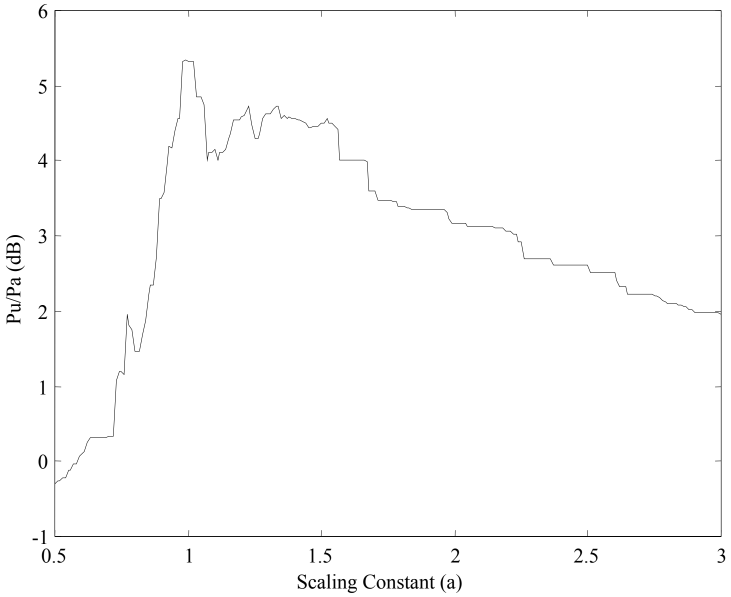

Figure 4-6. Unambiguous/Ambiguous Output Power Ratio vs. Scaling Constant for Sampled LFM, *TB* = 127, Input P_u/P_a = 0.0 dB

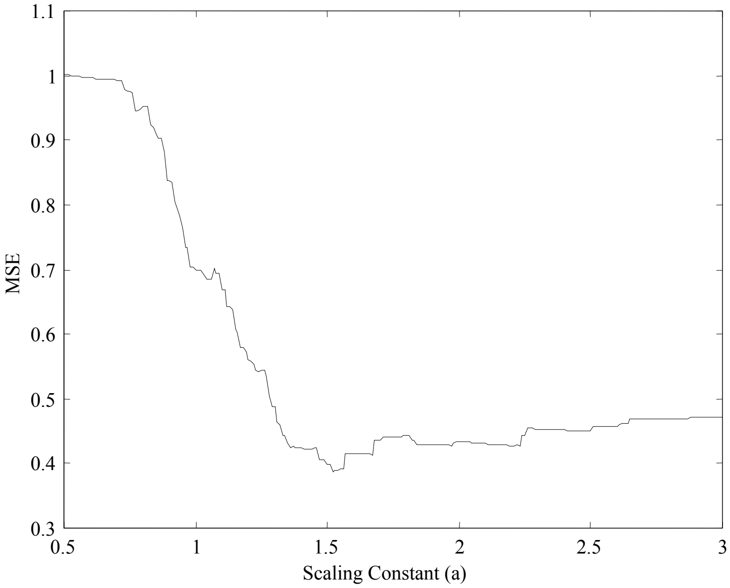

Figure 4-7. MSE between NLS Channel Output and Colored Unambiguous Output vs. Scaling Constant for Sampled LFM, *TB* = 127, Input P_u/P_a = 0.0 dB

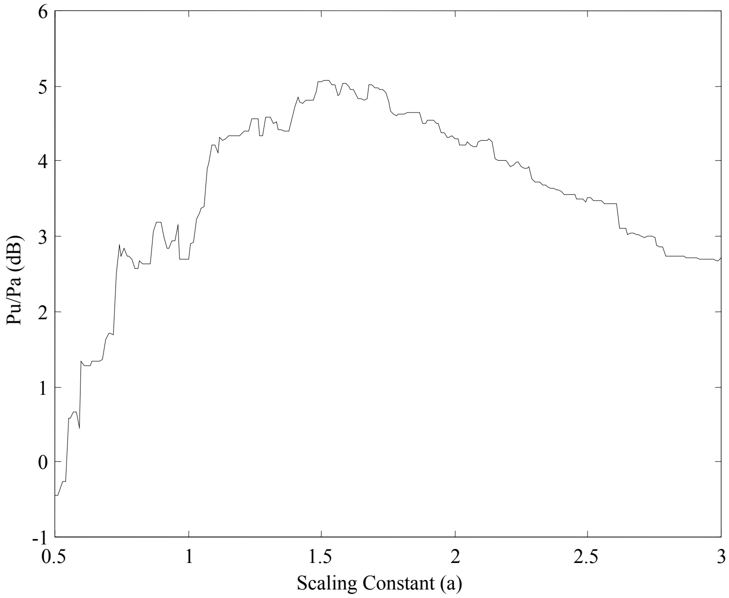

Figure 4-8. Unambiguous/Ambiguous Output Power Ratio vs. Scaling Constant for 16-Phase SA Code, *TB* = 127, Input P_u/P_a = 0.0 dB

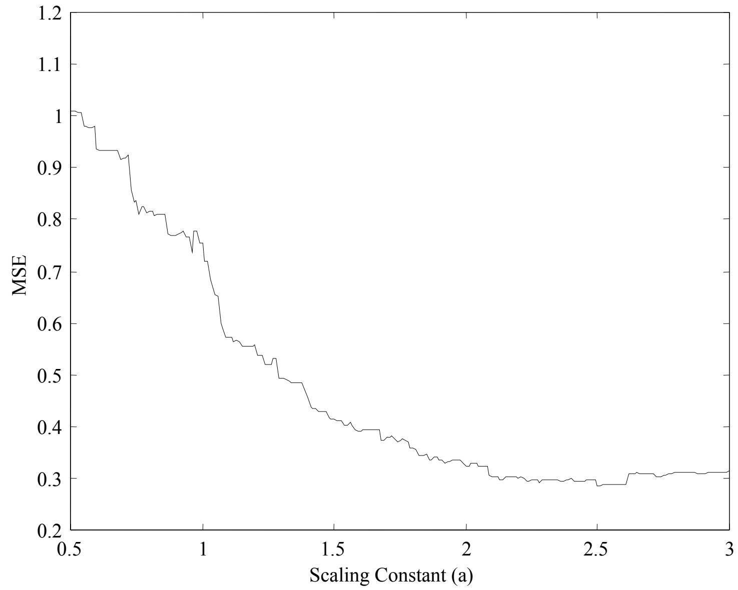

Figure 4-9. MSE between NLS Channel Output and Colored Unambiguous Output vs. Scaling Constant for 16-Phase SA Code, *TB* = 127, Input P_u/P_a = 0.0 dB

4.3.2 Representative Performance Results for Input P_u/P_a of –3.0 dB

For this case, the unambiguous signal power is half of the ambiguous signal power. The results are shown in Table 4-4.

Table 4-4. MCARM Test Results for Input P_u/P_a = -3.0 dB

Coding	Input P_u/P_a (dB)	Output P_u/P_a (dB)	Scaling Constant	MSE	SPRA (dB)	SPRU (dB)
31 LFM	-3	2.1	1.28	0.801	-9.1	-3.8
63 LFM	-3	2.1	1.51	0.700	-7.5	-2.7
127 LFM	-3	4.0	1.27	0.652	-9.9	-3.2
31-16 SA	-3	3.1	1.33	0.676	-11.0	-3.9
63-16 SA	-3	1.8	0.86	0.884	-14.8	-8.7
127-16 SA	-3	3.1	1.2	0.642	-12.2	-6.1

The trends are consistent with the previous case, although the maximum output P_u/P_a is smaller. However, the increase in P_u/P_a from input to output is larger. For example, for the 127 LFM code, P_u/P_a increased from –3.0 dB to 4.0 dB, as opposed to the previous case, where it increased from 0 dB to 5.5 db. Furthermore, the SPRA is nearly the same, while the SPRU is somewhat larger, indicating less loss of unambiguous clutter power. The results for the 127-16 SA code were not as close to the 0 dB case as the 127 LFM code. Both the SPRA and the SPRU are at least –3 dB less than for the 0 dB P_u/P_a case.

For comparison purposes, the plots for the 127 LFM and 127-16 SA codes are shown in Figure 4-10 through Figure 4-13.

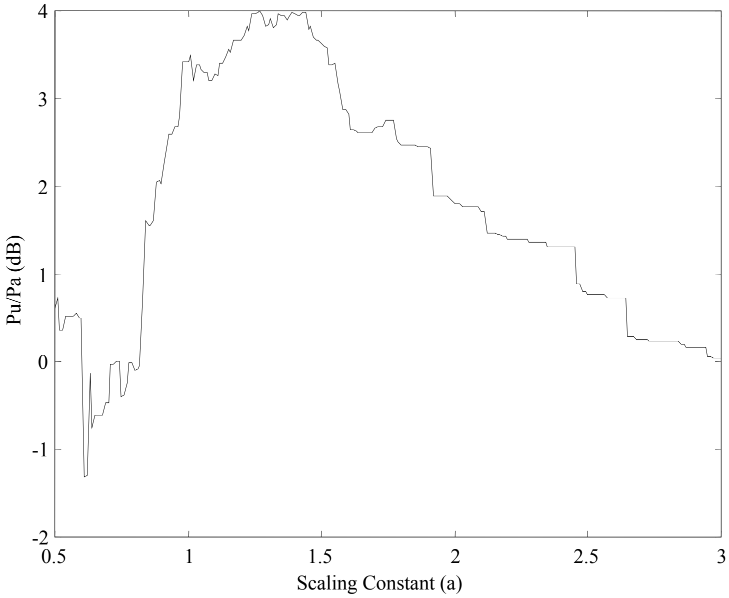

Figure 4-10. Unambiguous/Ambiguous Output Power Ratio vs. Scaling Constant for Sampled LFM, *TB* = 127, Input P_u/P_a = -3.0 dB

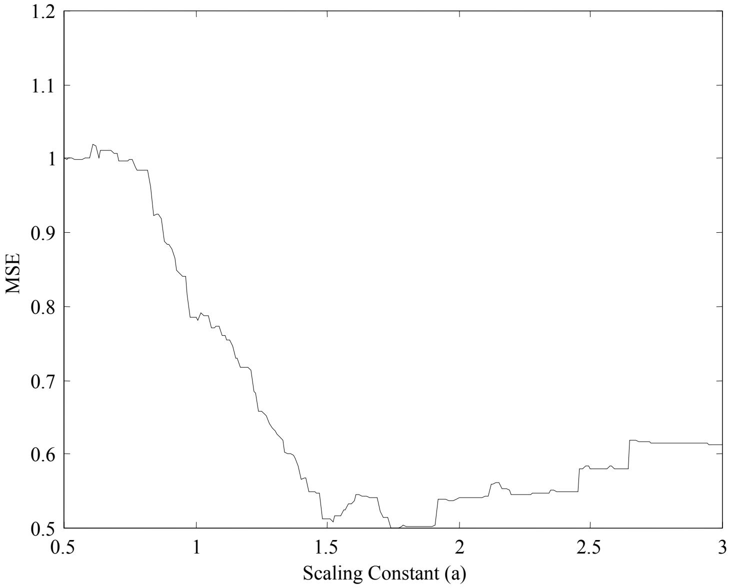

Figure 4-11. MSE between NLS Channel Output and Colored Unambiguous Output vs. Scaling Constant for Sampled LFM, *TB* = 127, Input P_u/P_a = -3.0 dB

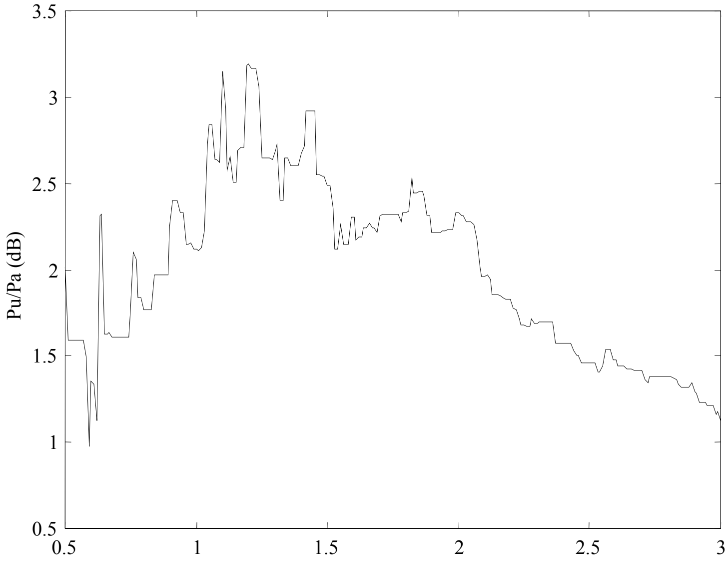

Figure 4-12. Unambiguous/Ambiguous Output Power Ratio vs. Scaling Constant for 16-Phase SA Code, *TB* = 127, Input P_u/P_a = -3.0 dB

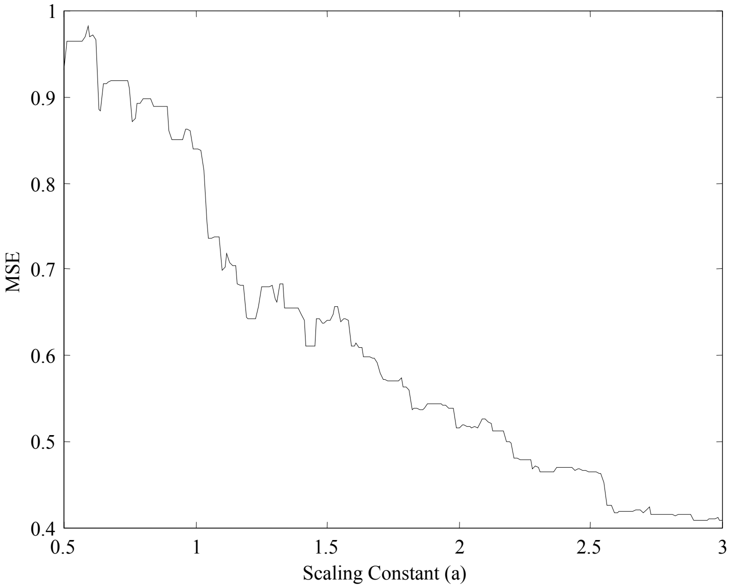

Figure 4-13. MSE between NLS Channel Output and Colored Unambiguous Output vs. Scaling Constant for 16-Phase SA Code, *TB* = 127, Input P_u/P_a = -3.0 dB

4.3.3 Representative Performance Results for Input P_u/P_a of –6.0 dB

For this case, the unambiguous signal power is one-fourth the ambiguous signal power. Performance results are shown in Table 4-5.

Table 4-5. MCARM Test Results for Input P_u/P_a = -6.0 dB

Coding	Input P_u/P_a (dB)	Output P_u/P_a (dB)	Scaling Constant	MSE	SPRA (dB)	SPRU (dB)
31 LFM	-6	1.8	0.69	0.958	-19.4	-11.3
63 LFM	-6	2.8	0.50	0.977	-22.7	-14.1
127 LFM	-6	4.6	1.03	0.775	-16.1	-5.9
31-16 SA	-6	1.5	0.92	0.921	-16.4	-7.8
63-16 SA	-6	-0.2	1.36	0.931	-14.0	-6.7
127-16 SA	-6	1.8	1.32	0.785	-15.35	-7.5

For the 127 LFM code, the P_u/P_a ratio increases from –6.0 dB on the input side to 4.6 dB on the output side using a scaling constant near one, as in previous cases. This particular coding also provided the least amount of unambiguous clutter suppression, as indicated by the SPRU metric. Overall, the SPRA and

SPRU metrics are much lower, indicating a trend that increasing the amount of ambiguous clutter power results in much greater suppression capability. However, it should be noted that the maximum output P_u/P_a ratio does not dramatically decrease, remaining within 4.0 dB of previous cases.

For comparison purposes, the plots for the 127 LFM and 127-16 SA codes are shown in Figure 4-14 through Figure 4-17.

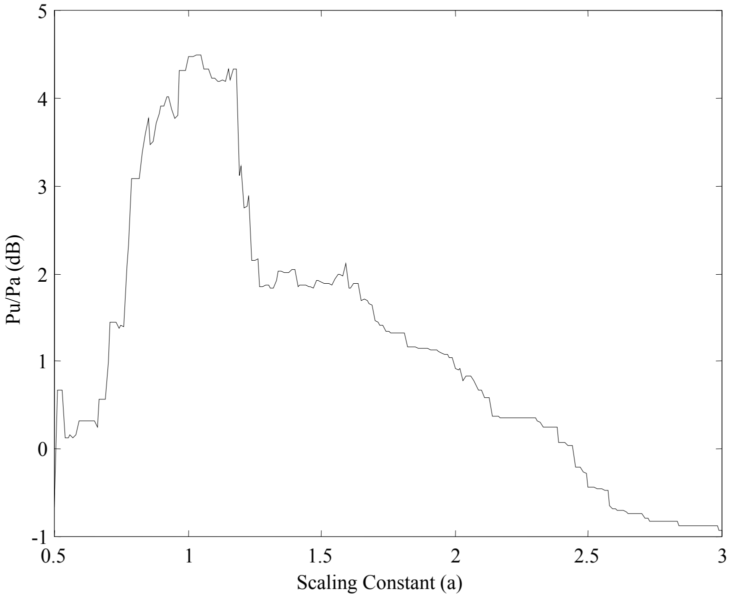

Figure 4-14. Unambiguous/Ambiguous Output Power Ratio vs. Scaling Constant for Sampled LFM, TB = 127, Input P_u/P_a = -6.0 dB

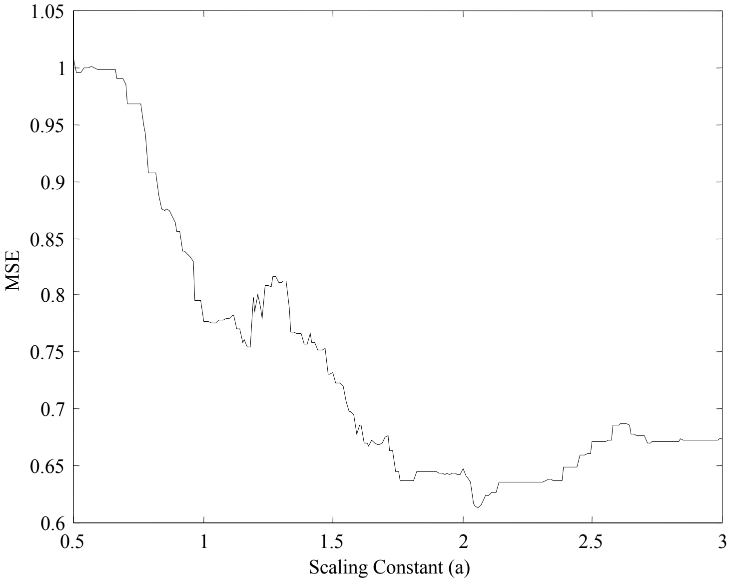

Figure 4-15. MSE between NLS Channel Output and Colored Unambiguous Output vs. Scaling Constant for Sampled LFM, *TB* = 127, Input P_u/P_a = -6.0 dB

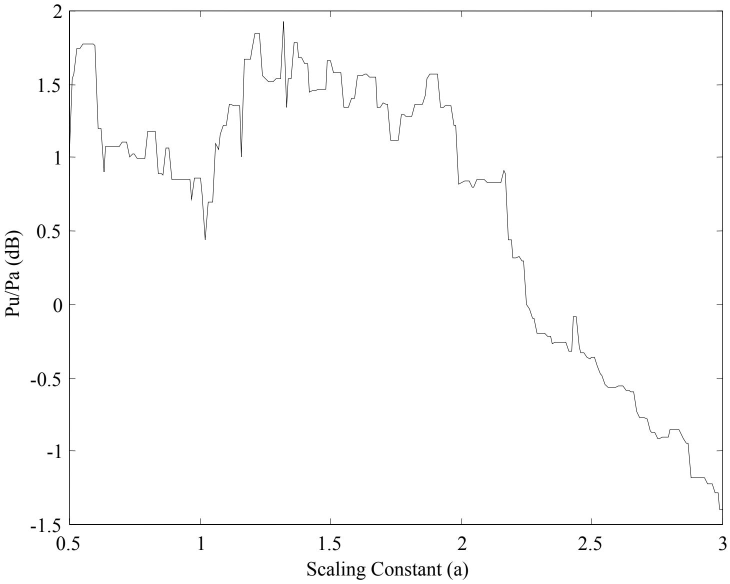

Figure 4-16. Unambiguous/Ambiguous Output Power Ratio vs. Scaling Constant for 16-Phase SA Code, *TB* = 127, Input P_u/P_a = -6.0 dB

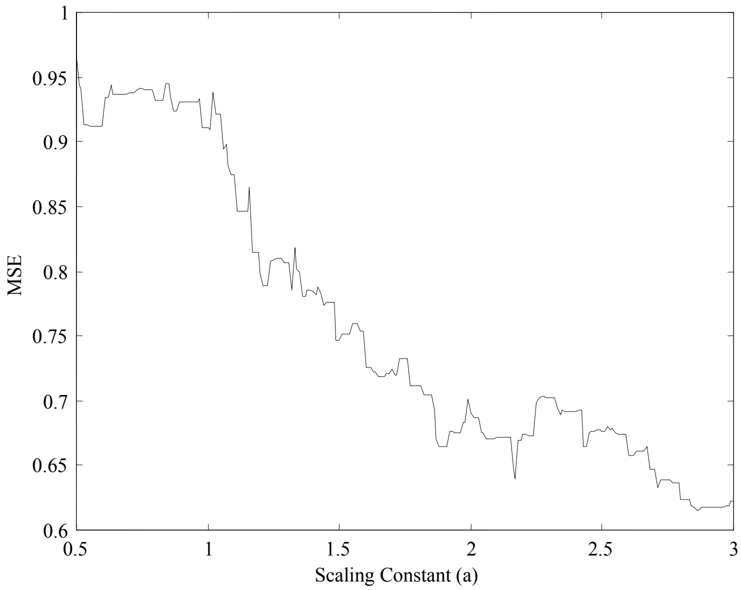

Figure 4-17. MSE between NLS Channel Output and Colored Unambiguous Output vs. Scaling Constant for 16-Phase SA Code, *TB* = 127, Input P_u/P_a = -6.0 dB

In general, even though the cross-range resolution dictated by the MCARM data set is relatively large, resulting in relatively large clutter cell sizes, the proposed NLS technique is effective at suppressing ambiguous clutter for the various input power ratios. Even when the ambiguous clutter power was four times the unambiguous power, an output P_u/P_a of 4.6 dB was achieved (for the 127 LFM code). Although the SA codes did not perform quite as well as the LFM codes, they exhibited the same basic trends and effectively suppressed the ambiguous clutter. The excellent ISL levels provided by the LFM codes and their demonstrated suppression performance, clearly indicates the importance of autocorrelation sidelobe properties on clutter suppression effectiveness.

5. Conclusion and Recommendations

5.1 Summary and Contributions

This work successfully expanded the knowledge base associated with using nonlinear suppression (NLS) techniques to enhance airborne, pulsed Doppler radar performance. Specifically, the research focus was on development and employment of NLS techniques to minimize range/Doppler ambiguity while providing effective clutter suppression. This work extends the NLS concept by focusing on *discrete coding* techniques providing both intrapulse (pulse to pulse) and interpulse (within the pulse) radar waveform modulation – previous work on analog implementations provided the technical foundation and impetus for the research.

The theory of NLS was developed, starting with the pulse diversity work of Guey, Bell, and others. For the common situation when target Doppler and delay are unknown, the ideal suppression operator (ISO) was introduced as a means of exploiting pulse diversity when the diverse codes are not truly orthogonal. Nonlinear suppression (NLS) was defined along with its various elements and the dispersed envelope thresholding (DET) technique introduced. The DET facilitated defining a suppressed correlation function consisting only of autocorrelation function sidelobes. In Theorem 2, it was shown that nonlinear suppression approaches ideal suppression as the integrated sidelobe level (ISL) approaches zero – indicating a primary dependence upon the autocorrelation sidelobe characteristics rather than restricting usable code families to ones containing orthogonal code sets.

Several discrete code families were examined, including m-sequences and Gold codes, and it was concluded that neither are ideally suited for radar NLS application – each exhibited relatively poor aperiodic performance relative to their traditional role in periodic coding applications such as communications. New code families were generated based using a Simulated Annealing (SA) technique. The algorithm developed yields both binary and polyphase codes having highly desirable (lower) peak correlation properties – their demonstrated performance was much closer to the Sarwate bound than either the m-sequences or Gold codes considered.

Two specific thresholding schemes were developed and analyzed, including the reserved code and dispersed code threshold. Most notable, the newly proposed reserved code thresholding technique is a relatively simple and efficient means for estimating the envelope (or shape) of the dispersed signal. Reserved code thresholding involves "reserving" (not transmitting) one code from the available family of codes – the matched filter, dispersed response of this code with the received data (consisting of target/clutter responses from all other codes) is used to establish appropriate threshold characteristics. For point targets, it was demonstrated that the threshold yielding the minimum mean-square error (MMSE) effectively tracks the dispersed envelope.

Finally, NLS performance was characterized using real airborne clutter data. Although the available measured data set was severely limited and not optimal for NLS testing, i.e., the data was of limited duration and not collected using a diverse-pulse radar having both intra-/interpulse modulation, the proposed NLS technique was effective at mitigating ambiguous clutter even though the clutter cells were relatively large – discretely coded NLS results were consistent with baseline analog LFM performance. Performance improvement a result of increasing time-bandwidth product and using codes with better ISL levels was also demonstrated. For "sparse impulsive clutter", resembling a collection of point targets, the degree of suppression may be made arbitrarily large by selecting codes with large time-bandwidth products and mutually dispersive cross-correlation characteristics. It is not clear, from the demonstration using the limited MCARM data set, exactly what the achievable NLS effectiveness is for distributed clutter.

5.2 Directions for Future Research

The first recommendation for future NLS research is to obtain measured clutter data with diverse-pulse radar. Ideally, the data would be collected on an airborne platform and provide various degrees of controllable ambiguity. The test radar should be designed to accommodate large time-bandwidth products and minimal pre-processing prior to data sampling and storage, as necessary to allow various NLS configurations to be effectively tested.

The second recommendation is to develop an implementation model for evaluating several NLS architectures. Examples include applying Doppler pre-processing and independently applying NLS to each Doppler channel. The impact of pulse diversity on Doppler processing needs to be assessed, specifically the ability of the Doppler filter bank to suppress clutter when the pulses are not identical. It has been observed that some additional ambiguity is introduced in Doppler by repeating every m^{th} pulse. The severity and impact of this ambiguity on NLS processing should be determined.

The simulated annealing (SA) technique proved very effective for developing good NLS pulse codes. For shorter code lengths, very good candidate codes were obtained. However, for longer codes the algorithm convergence time to a global minimum becomes excessive, even on fast computers. A potential SA enhancement that has received some attention in the literature is Quantum Annealing (QA). The QA technique incorporates a "tunneling" algorithm into the annealing process and may provide faster convergence times.

Finally, discrete implementation of developmental analog codes, such as Brown codes, may hold the key for providing near optimum codes for NLS applications. A deterministic approach to optimum coding could provide a vital tool for greatly enhancing NLS implementation and transition. Looking beyond the NLS focus of this research, both the discrete SA codes and the analog Brown codes have great potential in multi-user and low probability-of-intercept (LPI) radar applications. Likewise, these codes may be beneficial in communication, navigation, and sensor applications as well.

Appendix A Notations and Conventions

A.1 Symbols for Waveform Parameters

Unless otherwise noted, the following symbols are used consistently throughout the text.

Table A-1: Symbols for Waveform Parameters

Parameter	Notation
Time	t
Frequency	f (Hz) or ω (rad)
Amplitude	A
Power or Probability	P
Time Delay	τ
Doppler Shift	ν
Pulse Repetition Interval (PRI)	T_r
Pulse Repetition Frequency (PRF)	f_r
Pulse Width	T_p
Number of Pulses in CPI	N
Coherent Processing Interval (CPI)	T_{coh}
Wavelength of Carrier	λ
Frequency of Carrier	f_0
Sampling Interval	T_s
Energy	E
General Signal	$s(t)$
Analytic Signal	$\psi(t)$
Complex Envelope	$\mu(t)$
Velocity	v
Phase	ϕ
Range	R

A.2 Complex Envelope Notation

The radars of interest in this analysis are "narrowband", loosely defined as a system where the signal bandwidth is much less than the carrier frequency. The receiver radio frequency (*RF*) section typically down-converts, via mixing, the incoming signal to a much lower intermediate frequency (*IF*), perhaps in several stages. The *IF* signal is then filtered with a bandpass *IF* filter designed to pass all signals of interest. Following *IF* filtering, the signal is converted to baseband *In-phase* (*I*) and *Quadrature* (*Q*) components and sampled. The baseband *I* and *Q* signals represent the *complex envelope* of the received waveform. This complex waveform carries all information of interest to the radar signal processor. The complex envelope is used throughout this text. The *real-valued transmit signal* may be represented by

$$s(t) = a(t)\cos\left[2\pi f_0 \, t + \phi(t)\right] \tag{A.1}$$

where *a*(*t*) is the amplitude modulation function, such as a Gaussian pulse or rectangular pulse train, f_0 is the carrier frequency and $\phi(t)$ is a phase modulation function. The transmit signal spectrum *S*(*f*) is found using the *Fourier Transform* relation

$$s(t) = \int_{-\infty}^{\infty} S(f)\, e^{j2\pi f t}\, df \tag{A.2}$$

$$S(f) = \int_{-\infty}^{\infty} s(t)\, e^{-j2\pi f t}\, dt \ . \tag{A.3}$$

The *complex signal*, often called the *analytic signal*, is given by

$$\psi(t) = s(t) + j\,\hat{s}(t) \tag{A.4}$$

where $s(t)$ and $\hat{s}(t)$ are related by the Hilbert transform

$$s(t) = -\frac{1}{\pi}\int_{=\infty}^{\infty} \frac{\hat{s}(\xi)}{t-\xi}\, d\xi \tag{A.5}$$

$$\hat{s}(t) = \frac{1}{\pi}\int_{=\infty}^{\infty} \frac{s(\xi)}{t-\xi}\, d\xi \ . \tag{A.6}$$

An interesting property of the complex signal is that its spectrum is zero for negative frequencies

$$\Psi(f) = \begin{cases} 2S(f) & f \ge 0 \\ 0 & f < 0 \end{cases} \tag{A.7}$$

The real-valued transmit signal is related to the complex signal by

$$s(t) = \mathrm{Re}\{\, \psi(t) \,\} \ . \tag{A.8}$$

A sinusoidal signal represented by Eq (A.1) has a complex signal given by

$$\psi(t) = a(t)\, e^{j2\pi f_0 t + \phi(t)} \ . \tag{A.9}$$

Equation (A.9) illustrates the utility of working with complex notation, i.e., the convenience of working with exponential notation rather than trigonometric functions. Equation (A.9) may also be represented in terms of its *complex envelope* $\mu(t)$

$$\psi(t) = \mu(t)\,e^{j2\pi f_0 t} \tag{A.10}$$

where
$$\mu(t) = \left|\mu(t)\right| e^{j\varphi(t)} \;. \tag{A.11}$$

For narrowband signals represented by Eq (A.9), it is a valid approximation [20] to let $\left|\mu(t)\right| = a(t)$ and $\varphi(t) = \phi(t)$ so that the complex envelope of the real signal of Eq (A.1) becomes

$$\mu(t) = a(t)\,e^{j\phi(t)} \;. \tag{A.12}$$

The *complex envelope spectrum* of $\mu(t)$ is given by the Fourier Transform

$$\mu(t) = \int_{-\infty}^{\infty} M(f)\,e^{j2\pi f t}\,df \tag{A.13}$$

$$M(f) = \int_{-\infty}^{\infty} \mu(t)\,e^{-j2\pi f t}\,dt \;. \tag{A.14}$$

The complex envelope spectrum may also be represented by

$$M(f) = \left|M(f)\right| e^{j\theta(f)} \;. \tag{A.15}$$

Signal energy (*E*) may be calculated from the real-valued signal, the complex signal, or the time signal, according to the following

$$\begin{aligned} E &= \int_{-\infty}^{\infty} \left[\, s(t) \,\right]^2 dt = \int_{-\infty}^{\infty} \left|S(f)\right|^2 df \\ E &= \frac{1}{2}\int_{-\infty}^{\infty} \left|\psi(t)\right|^2 dt = \frac{1}{2}\int_{-\infty}^{\infty} \left|\Psi(f)\right|^2 df \\ E &= \frac{1}{2}\int_{-\infty}^{\infty} \left|\mu(t)\right|^2 dt = \frac{1}{2}\int_{-\infty}^{\infty} \left|M(f)\right|^2 df \;. \end{aligned} \tag{A.16}$$

A.3 The Radar Range Equation

There are many forms of the radar range equation for calculating the power received from a target. The following form is used here

$$P_r = \frac{P_t\,G\,A_e\,\sigma}{\left(4\pi\right)^2 R^4} \tag{A.17}$$

where

P_r = Received Power
P_t = Transmitted Power
G = Antenna Gain
A_e = Effective Area of Aperture
σ = Radar Cross Section of Target
R = Target Range

The target return amplitude may be found from $A = \sqrt{2P_r}$ so that the return amplitude is

$$A_r = \sqrt{\frac{2 P_t G A_e \sigma}{(4\pi)^2 R^4}} \ . \tag{A.18}$$

A.4 Continuous and Discrete Correlation Functions

Given the diverse definitions of correlation function found in the literature, it is important to establish a definition for use throughout this dissertation.

A.4.1 Fundamental Definitions and Properties

Definition A.1 (Deterministic Cross-Correlation Function). *Let x(t) and y(t) be two complex functions and let t be a real variable. The* ***Deterministic Cross-Correlation Function*** $R_{xy}(\tau)$ *is defined as*

$$R_{xy}(\tau) = \int_{-\infty}^{\infty} x(t) y^*(t+\tau) dt \ . \tag{A.19}$$

From Definition A.1, several important properties may be derived

$$R_{xy}(-\tau) = R_{yx}^*(\tau) \tag{A.20}$$

$$R_{xy}^*(\tau) = R_{yx}(-\tau) \tag{A.21}$$

$$R_{xy}^*(-\tau) = R_{yx}(\tau) \ . \tag{A.22}$$

The ***Deterministic Autocorrelation Function***, $R_{xx}(\tau)$, is simply the cross-correlation of $x(t)$ with itself per Eq (A.19).

For pulsed radar applications, the primary interest is in the correlation characteristics of rectangular pulse functions. Let $u_n(t)$ be a pulse function with amplitude modulation $a(t)$, phase modulation $\phi_n(t)$, and duration T_p. Then

$$u_n(t) = a(t)e^{j\phi_n(t)} \tag{A.23}$$

where

$$a(t) = \begin{cases} 1 & 0 \le t \le T_p \\ 0 & \text{otherwise} \end{cases} . \tag{A.24}$$

From Eq (A.19), the ***Cross-Correlation Function*** $R_{01}(\tau)$ of two pulses, $u_0(t)$ and $u_1(t)$ is

$$\begin{aligned} R_{01}(\tau) &= \int_{-\infty}^{\infty} u_0(t)u_1^*(t+\tau)dt \\ &= \int_0^{T_p+\tau} u_0(t-\tau)u_1^*(t)dt \qquad \text{for } \tau < 0 \\ &= \int_0^{T_p-\tau} u_0(t)u_1^*(t+\tau)dt \qquad \text{for } \tau \ge 0 \ . \end{aligned} \tag{A.25}$$

A.4.2 Discrete Correlation Functions

When pulse functions are discrete, they may be represented as a sequence of elemental pulses and expressed as

$$u_n(t) = \sum_{j=0}^{N-1} a_j\, \varphi(t - jT_c) \tag{A.26}$$

where a_j is a complex number, T_c is the elemental pulse duration, N is the number of elemental pulses ("chips") in $u_n(t)$, and the elemental pulse function is defined as

$$\varphi(t) = \begin{cases} 1 & 0 \le t \le T_c \\ 0 & \text{otherwise} \end{cases} . \tag{A.27}$$

Representing two sequences $u_n(t)$ and $u_m(t)$ using Eq (A.26), with $u_m(t)$ given by,

$$u_m(t) = \sum_{j=0}^{N-1} b_j\, \varphi(t - jT_c) \tag{A.28}$$

and assuming delay τ is an integer multiple of T_c, $\tau = l \cdot T_c$, results in a ***Cross-Correlation Function*** for $u_n(t)$ and $u_m(t)$ of the form

$$R_{nm}(\tau) = \int_{-\infty}^{\infty} u_n(t)u_m^*(t + l \cdot T_c)dt \ . \tag{A.29}$$

Suppose that $\tau < 0$, which implies that $1 - N \leq l < 0$. Then

$$\begin{aligned} R_{nm}(\tau) &= \int_0^{T_p+\tau} u_n(t-\tau)u_m^*(t)dt \\ &= \int_0^{l\cdot T_c+T_p} u_n(t-lT_c)u_m^*(t)dt \\ &= \int_0^{l\cdot T_c+T_p} \sum_{j=0}^{N-1} a_j\varphi(t-jT_c-lT_c)\sum_{k=0}^{N-1} b_k\varphi(t-kT_c)dt \ . \end{aligned} \tag{A.30}$$

Using the change of variables, $t' = t - kT_c$, Eq (A.30) becomes

$$R_{nm}(\tau) = \sum_{j=0}^{N-1}\sum_{k=0}^{N-1} a_j b_k^* \int_{-kT_c}^{lT_c+T_p-kT_c} \varphi\left(t' - [l + j - k]T_c\right) \cdot \varphi\left(t'\right)dt' \ . \tag{A.31}$$

Equation (A.31) is nonzero only when the elemental pulses in the integral overlap, i.e., for $j = k - l$, and may be rewritten as

$$R_{nm}(\tau) = \sum_{k=0}^{N-1} a_{k-l}b_k^* \int_{-kT_c}^{T_p-(k-l)T_c} \varphi^2(t)dt \ . \tag{A.32}$$

Since $\tau < 0$ and $1 - N \leq l < 0$, then $a_{m-l} = 0$ for $k > N - 1 + l$. As written, the integral term in Eq (A.32) is the elemental pulse energy which can be assumed, without loss of generality, to be unity. By applying the same procedure for $\tau \geq 0$, the ***Cross-Correlation Function*** for ***Discretely-Coded Pulses*** becomes

$$R_{nm}(\tau) = \sum_{k=0}^{N-1+l} a_{k-l}b_k^* \qquad \tau < 0, \ \tau = l \cdot T_c \tag{A.33}$$

$$R_{nm}(\tau) = \sum_{k=0}^{N-1-l} a_k b_{k+l}^* \qquad \tau > 0, \ \tau = l \cdot T_c \ . \tag{A.34}$$

From Eq (A.33) and Eq (A.34) results, it is possible to specify the correlation properties of any two discrete codes x and y by defining the *Discrete Aperiodic Crosscorrelation Function*, $C_{xy}(l)$.

Definition A.2 (Discrete Aperiodic Crosscorrelation Function) [28:610]. *Let x and y be two complex sequences of length N. The* ***Discrete Aperiodic Crosscorrelation Function*** $C_{xy}(l)$ *is defined by*

$$C_{xy}(l) = \begin{cases} \sum_{k=0}^{N-1-l} x_k y_{k+l}^* & 0 \le l \le N-1 \\ \sum_{k=0}^{N-1+l} x_{k-l} y_k^* & 1-N \le l < 0 \\ 0 & |l| \ge N \end{cases} \tag{A.35}$$

Some fundamental properties of discrete aperiodic cross-correlation functions include

$$C_{xy}(-l) = C_{yx}^*(l) \tag{A.36}$$

$$C_{xy}^*(l) = C_{yx}(-l) \tag{A.37}$$

$$C_{xy}^*(-l) = C_{yx}(l) \quad . \tag{A.38}$$

These parallel the deterministic cross-correlation properties of Eqs (A.20) thru (A.22). The importance of discrete aperiodic cross-correlation functions is readily apparent when $\tau = lT_c$, since the cross-correlation of any two pulses is determined from the discrete aperiodic correlation of complex sequences forming the pulse codes. For an arbitrary delay, i.e., $\tau \neq lT_c$, the cross-correlation function $R_{xy}(\tau)$ may still be determined from $C_{xy}(l)$ [28:594]. For this research, it is assumed that $\tau = lT_c$ for all cases. Unless otherwise specified, the discrete aperiodic cross-correlation function is referred to as the *aperiodic correlation function* and the discrete case is assumed.

The Normalized Aperiodic Correlation Function is often used in analysis. It is merely the aperiodic correlation function divided by the code length *N*.

Definition A.3 (Normalized Discrete Aperiodic Crosscorrelation Function). *Let x and y be two complex sequences of length N. The* ***Normalized Discrete Aperiodic Cross-Correlation Function*** $\theta_{xy}(l)$ *is defined by*

$$\theta_{xy}(l) = \begin{cases} \frac{1}{N}\sum_{k=0}^{N-1-l} x_k y_{k+l}^* & 0 \le l \le N-1 \\ \frac{1}{N}\sum_{k=0}^{N-1+l} x_{k-l} y_k^* & 1-N \le l < 0 \\ 0 & |l| \ge N \end{cases} \tag{A.39}$$

The *aperiodic* correlation function is useful when evaluating pulse diverse radar performance. Much research has been accomplished on code families yielding good *periodic* (full-period) cross-correlation properties. However, these same code families often possess poor *aperiodic* cross-correlation characteristics. Although the distinction between *periodic* and *aperiodic* cross-correlation may appear unimportant at first, it is important for this work because, unlike many communication system applications which rely on favorable *aperiodic* cross-correlation performance, each coded radar pulse normally contains a single code period. Thus, radar receiver performance is generally based on *aperiodic* correlation results.

A.5 Matched Filtering

A *Matched Filter*, also known as the *North Filter*, is a well-known "optimal" filter for signals operating over a white noise channel under several criteria [46].

Definition A.3 (Matched Filter) [46:353]. *Let s(t) be a complex signal and let t be a real variable. The* ***Matched Filter, h,*** *is defined as the filter with impulse response*

$$h(t) = ks^*(T-t) \tag{A.40}$$

where k and T are arbitrary real constants. The transfer function for matched filter h(t) is given by

$$H(f) = kS^*(f)e^{-j2\pi fT} \tag{A.41}$$

where S(f) is the Fourier Transform of s(t).

Constants *k* and *T* simply represent scaling and delay, respectively, and may be conveniently ignored. An important matched filter property involves its relationship to the correlation function. Let $y(t) = s(t) * h(t)$ where $*$ denotes convolution and $h(t)$ is a matched filter for $s(t)$. The matched filter output is

$$\begin{aligned} y(t) &= s(t) * h(t) = s(t) * s^*(-t) \\ &= \int_{-\infty}^{\infty} s(\lambda)s^*(\lambda - t)d\lambda = \int_{-\infty}^{\infty} s(\lambda + t)s^*(\lambda)d\lambda \\ &= R_{ss}^*(t) = R_{ss}(-t) \ . \end{aligned} \tag{A.42}$$

Thus, matched filtering performance can be directly obtained through correlation. Consider two pulse functions $u_0(t)$ and $u_1(t)$ and let $s(t) = u_0(t) + u_1(t)$. By applying $s(t)$ to matched filters $h_0(t)$ and $h_1(t)$, and utilizing appropriate convolution properties, the filter outputs can be expressed as

$$\begin{aligned} y_0(t) &= s(t) * h_0(t) = \left[u_0(t) + u_1(t)\right] * h_0(t) \\ &= u_0(t) * u_0^*(-t) + u_1(t) * u_0^*(-t) \\ &= R_{00}^*(t) + R_{10}^*(t) \end{aligned} \tag{A.43}$$

$$\begin{aligned} y_1(t) &= s(t) * h_1(t) = \left[u_0(t) + u_1(t)\right] * h_1(t) \\ &= u_0(t) * u_1^*(-t) + u_1(t) * u_1^*(-t) \\ &= R_{01}^*(t) + R_{11}^*(t) \quad . \end{aligned} \tag{A.44}$$

Sequential application of multiple matched filters is important for NLS analysis. Figure A-1 shows a sequential matched filtering process. The second filter is not a matched filter but has a transfer function equal to the previous filter's conjugate.

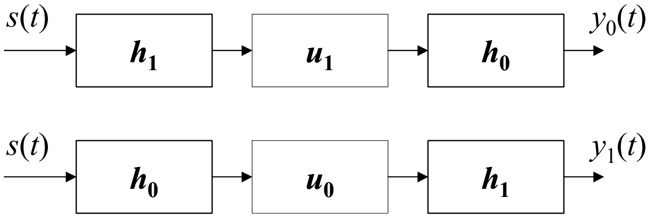

Figure A-1. Sequential Matched Filter Processing

Using $s(t)$ from the previous example, outputs y_0 and y_1 are found from

$$\begin{aligned} y_0(t) &= s(t) * h_1(t) * u_1(t) * h_0(t) \\ &= \left[u_0(t) + u_1(t)\right] * h_1(t) * u_1(t) * h_0(t) \\ &= u_0(t) * u_1^*(-t) * u_1(t) * u_0^*(-t) + u_1(t) * u_1^*(-t) * u_1(t) * u_0^*(-t) \\ &= R_{01}^*(t) * R_{10}^*(t) + R_{10}^*(t) * R_{11}^*(t) \\ &= R_{00}^*(t) * R_{11}^*(t) + R_{10}^*(t) * R_{11}^*(t) \\ &= \left[R_{00}^*(t) + R_{10}^*(t)\right] * R_{11}^*(t) \\ &= \left[R_{11}^*(t) + R_{01}^*(t)\right] * R_{10}^*(t) \end{aligned} \tag{A.45}$$

$$
\begin{aligned}
y_1(t) &= s(t) * h_0(t) * u_0(t) * h_1(t) \\
&= \left[u_0(t) + u_1(t)\right] * h_0(t) * u_0(t) * h_1(t) \\
&= u_0(t) * u_0^*(-t) * u_0(t) * u_1^*(-t) \; + \; u_1(t) * u_0^*(-t) * u_0(t) * u_1^*(-t) \\
&= R_{00}^*(t) * R_{01}^*(t) \; + \; R_{10}^*(t) * R_{01}^*(t) \\
&= R_{00}^*(t) * R_{01}^*(t) \; + \; R_{11}^*(t) * R_{00}^*(t) \\
&= \left[R_{11}^*(t) \; + \; R_{01}^*(t)\right] * R_{00}^*(t) \\
&= \left[R_{00}^*(t) \; + \; R_{10}^*(t)\right] * R_{01}^*(t) \quad .
\end{aligned}
\tag{A.46}
$$

Due to the fundamental relationship between matched filtering and correlation, the cross-correlation and autocorrelation properties are sufficient for determining performance of any pulse codes. For radar applications involving discrete codes, the aperiodic correlation function is used.

Appendix B MCARM Clutter Test Results

For conciseness and clarity, only the P_u/P_a and MSE metric plots for code lengths of 127 were presented in Chapter 4. This appendix provides metric plots for all tested code lengths. Table B-1 lists the basic metrics corresponding to the maximum P_u/P_a.

Table B-1. MCARM Clutter Test Results

Coding	Input P_u/P_a (dB)	Output P_u/P_a (dB)	Scaling Constant	MSE	SPRA (dB)	SPRU (dB)
31 LFM	0.0	3.7	1.24	0.659	-6.7	-2.8
63 LFM	0.0	4.2	1.38	0.571	-6.2	-2.4
127 LFM	0.0	5.5	0.99	0.702	-9.7	-4.7
31-16 SA	0.0	4.4	1.41	0.530	-7.8	-2.1
63-16 SA	0.0	3.0	1.21	0.638	-8.5	-4.2
127-16 SA	0.0	5.1	1.51	0.410	-8.2	-3.2
31 LFM	0.0	2.1	1.28	0.801	-9.1	-3.8
63 LFM	-3.0	2.1	1.51	0.700	-7.5	-2.7
127 LFM	-3.0	4.0	1.27	0.652	-9.9	-3.2
31-16 SA	-3.0	3.1	1.33	0.676	-11.0	-3.9
63-16 SA	-3.0	1.8	0.86	0.884	-14.8	-8.7
127-16 SA	-3.0	3.1	1.2	0.642	-12.2	-6.1
31 LFM	-6.0	1.8	0.69	0.958	-19.4	-11.3
63 LFM	-6.0	2.8	0.50	0.977	-22.7	-14.1
127 LFM	-6.0	4.6	1.03	0.775	-16.1	-5.9
31-16 SA	-6.0	1.5	0.92	0.921	-16.4	-7.8
63-16 SA	-6.0	-0.2	1.36	0.931	-14.0	-6.7
127-16 SA	-6.0	1.8	1.32	0.785	-15.35	-7.5

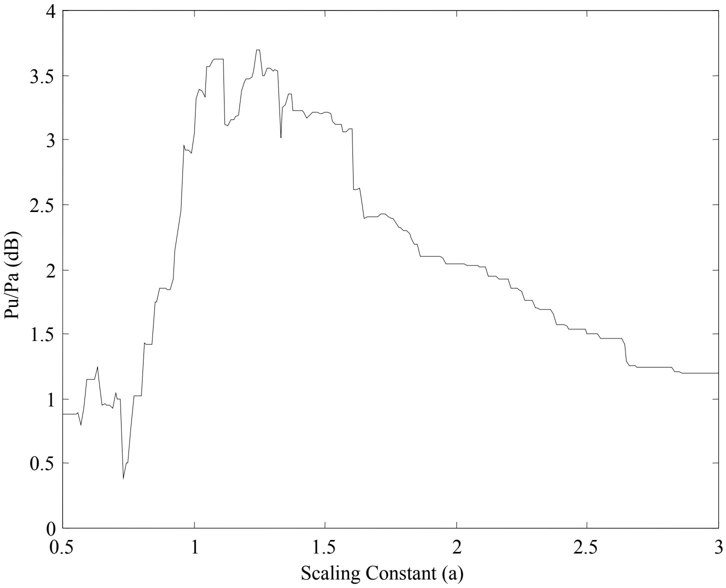

Figure B-1. Unambiguous/Ambiguous Output Power Ratio vs. Scaling Constant for Sampled LFM, *TB* = 31, Input P_u/P_a = 0.0 dB

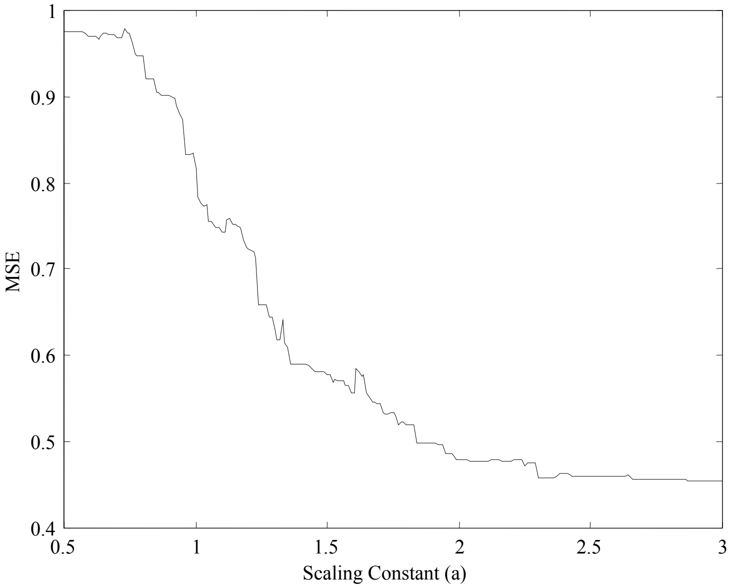

Figure B-2. MSE between NLS Channel Output and Colored Unambiguous Output vs. Scaling Constant for Sampled LFM, *TB* = 31, Input P_u/P_a = 0.0 dB

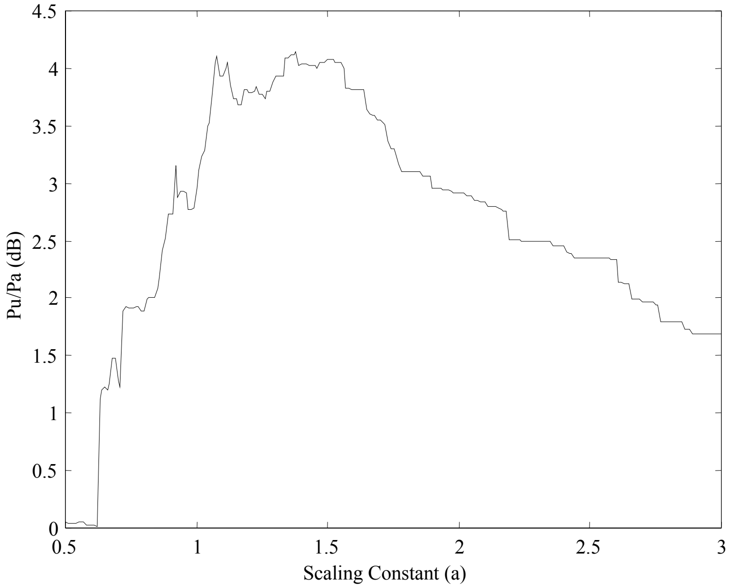

Figure B-3. Unambiguous/Ambiguous Output Power Ratio vs. Scaling Constant for Sampled LFM, *TB* = 63, Input P_u/P_a = 0.0 dB

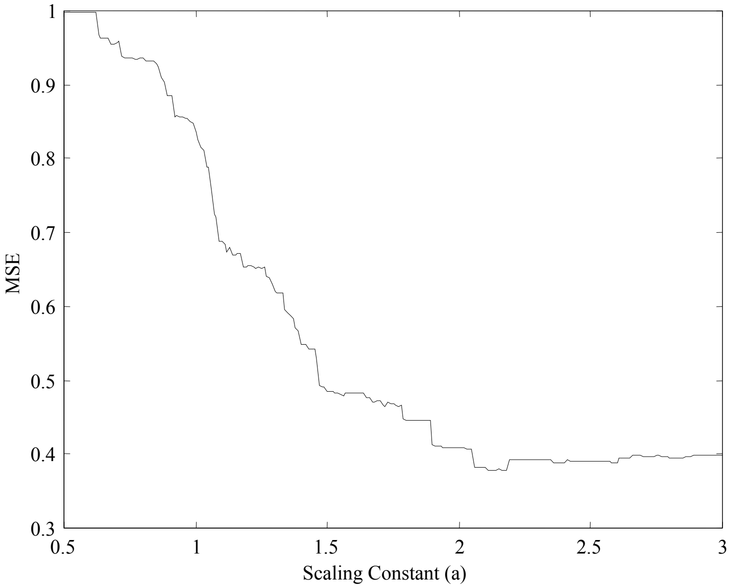

Figure B-4. MSE between NLS Channel Output and Colored Unambiguous Output vs. Scaling Constant for Sampled LFM, *TB* = 63, Input P_u/P_a = 0.0 dB

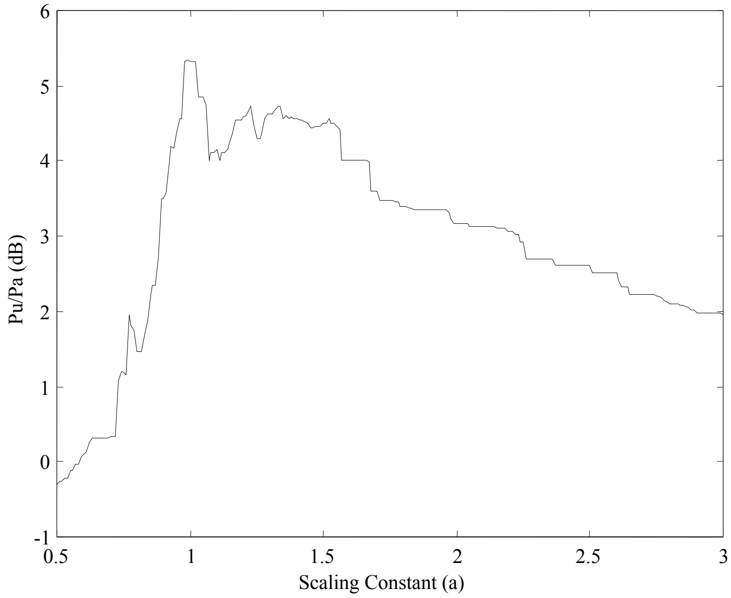

Figure B-5. Unambiguous/Ambiguous Output Power Ratio vs. Scaling Constant for Sampled LFM, *TB* = 127, Input P_u/Pa = 0.0 dB

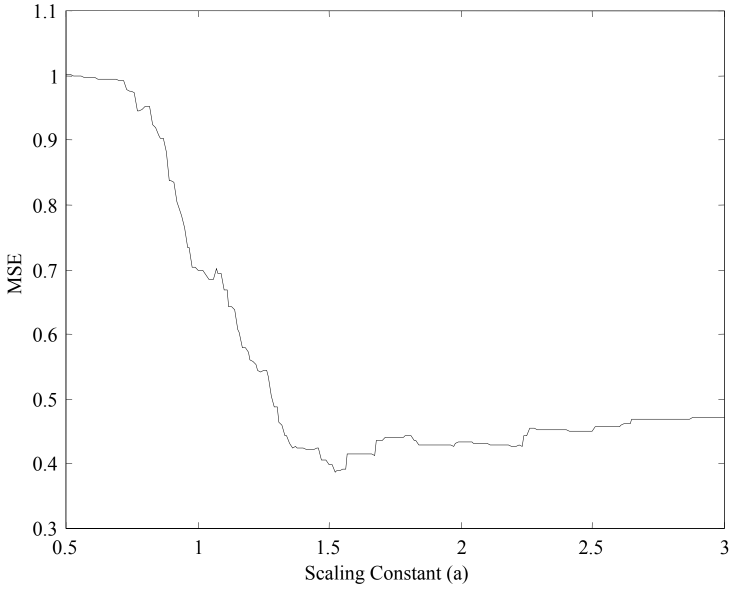

Figure B-6. MSE between NLS Channel Output and Colored Unambiguous Output vs. Scaling Constant for Sampled LFM, *TB* = 127, Input P_u/P_a = 0.0 dB

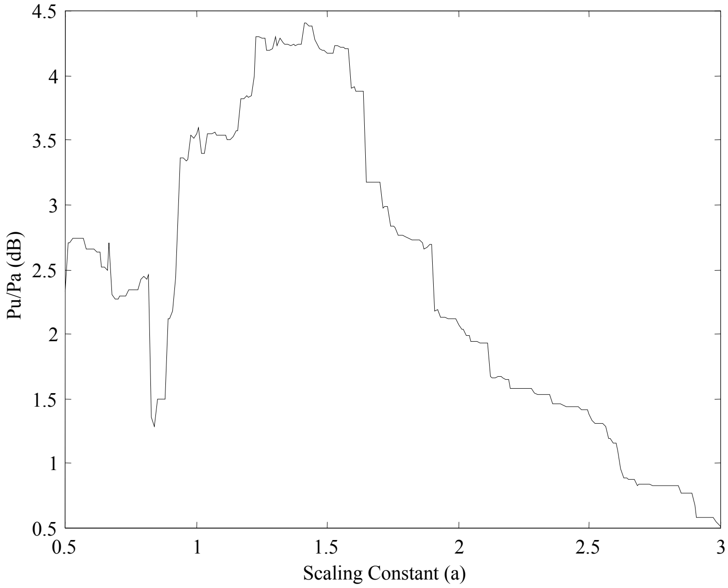

Figure B-7. Unambiguous/Ambiguous Output Power Ratio vs. Scaling Constant for 16-Phase SA Code, *TB* = 31, Input P_u/P_a = 0.0 dB

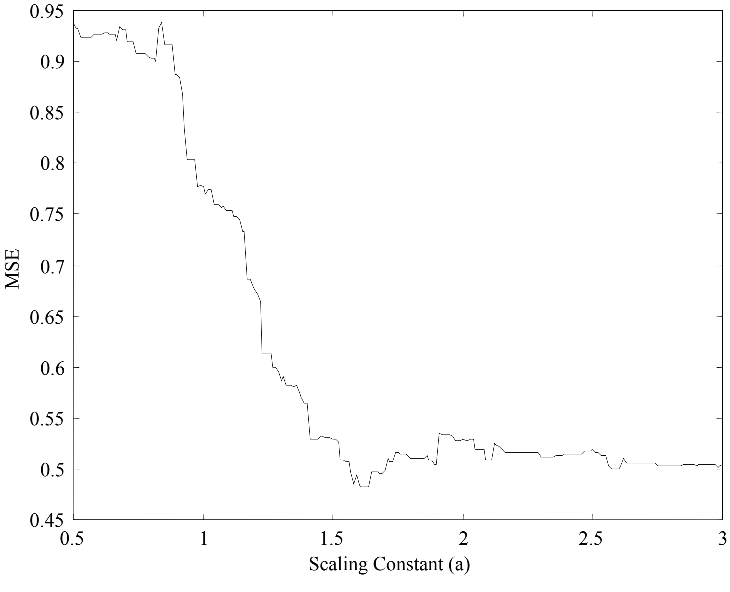

Figure B-8. MSE between NLS Channel Output and Colored Unambiguous Output vs. Scaling Constant for 16-Phase SA Code, *TB* = 31, Input P_u/P_a = 0.0 dB

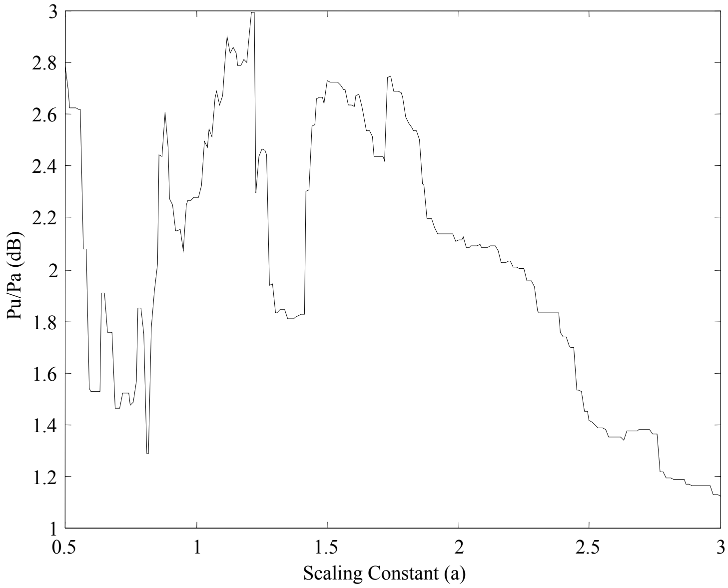

Figure B-9. Unambiguous/Ambiguous Output Power Ratio vs. Scaling Constant for 16-Phase SA Code, *TB* = 63, Input P_u/P_a = 0.0 dB

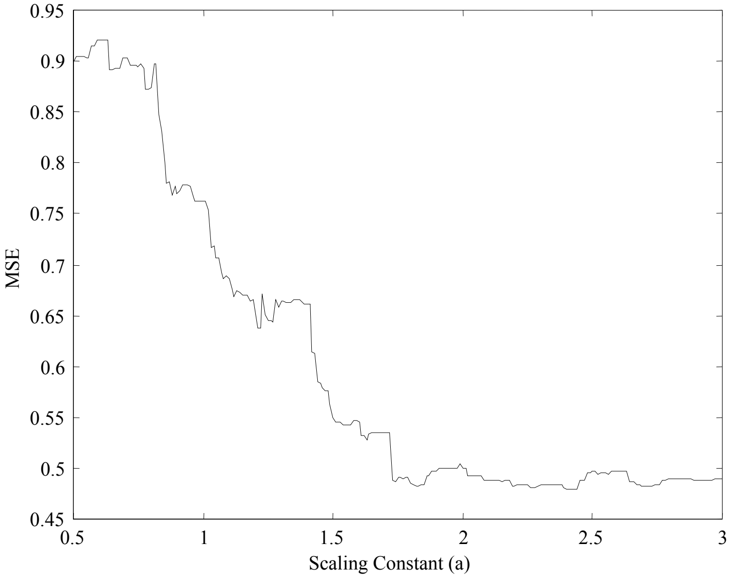

Figure B-10. MSE between NLS Channel Output and Colored Unambiguous Output vs. Scaling Constant for 16-Phase SA Code, *TB* = 63, Input P_u/P_a = 0.0 dB

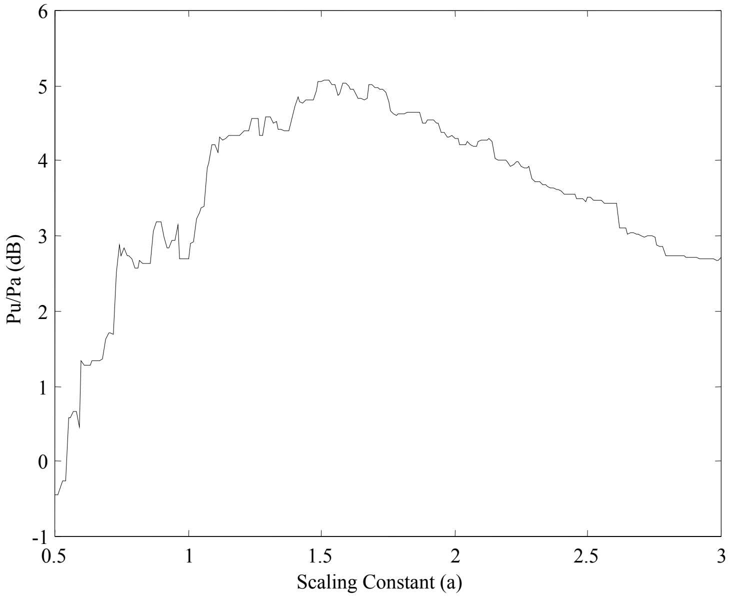

Figure B-11. Unambiguous/Ambiguous Output Power Ratio vs. Scaling Constant for 16-Phase SA Code, *TB* = 127, Input P_u/P_a = 0.0 dB

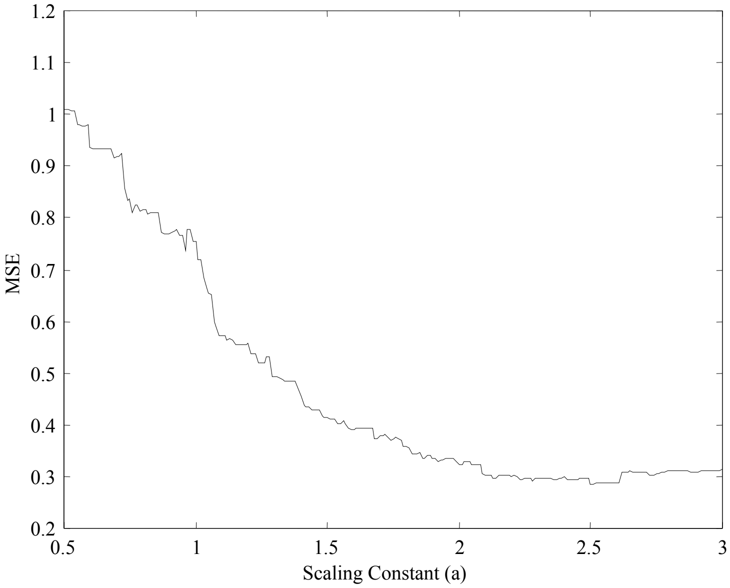

Figure B-12. MSE between NLS Channel Output and Colored Unambiguous Output vs. Scaling Constant for 16-Phase SA Code, *TB* = 127, Input P_u/P_a = 0.0 dB

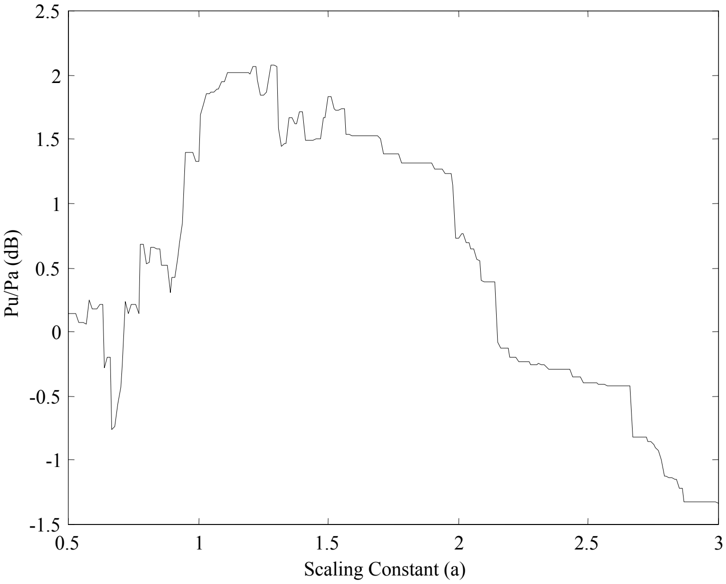

Figure B-13. Unambiguous/Ambiguous Output Power Ratio vs. Scaling Constant for Sampled LFM, TB = 31, Input P_u/P_a = -3.0 dB

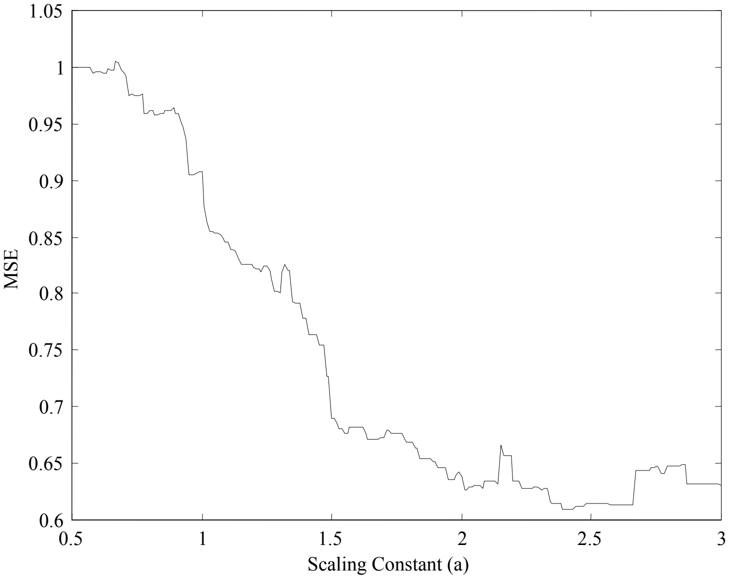

Figure B-14. MSE between NLS Channel Output and Colored Unambiguous Output vs. Scaling Constant Sampled LFM, TB = 31, Input P_u/P_a = -3.0 dB

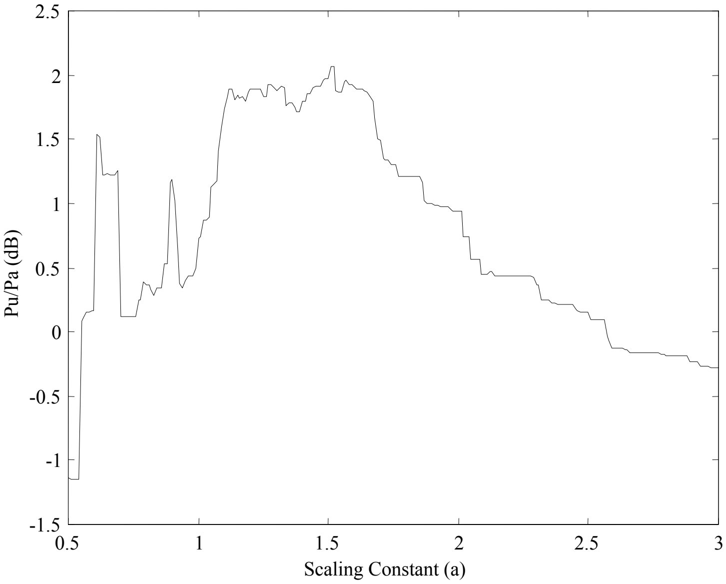

Figure B-15. Unambiguous/Ambiguous Output Power Ratio vs. Scaling Constant for Sampled LFM, *TB* = 63, Input P_u/P_a = -3.0 dB

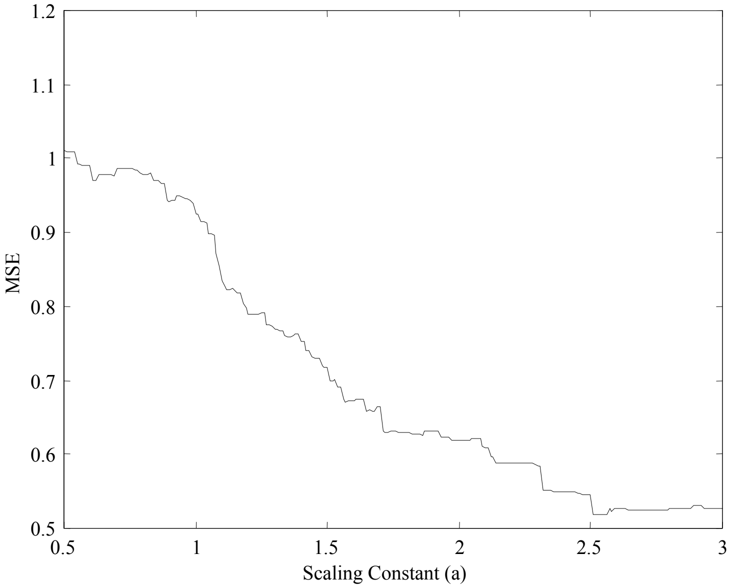

Figure B-16. MSE between NLS Channel Output and Colored Unambiguous Output vs. Scaling Constant Sampled LFM, *TB* = 63, Input P_u/P_a = -3.0 dB

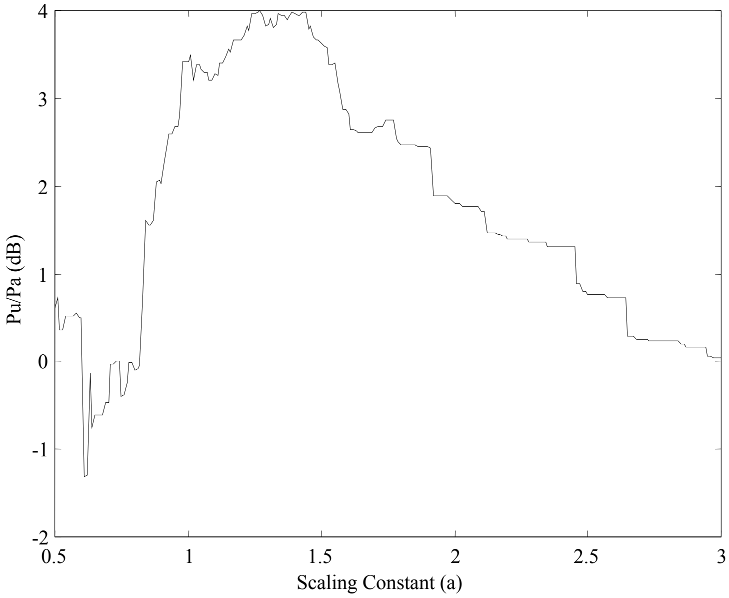

Figure B-17. Unambiguous/Ambiguous Output Power Ratio vs. Scaling Constant for Sampled LFM, *TB* = 127, Input P_u/P_a = -3.0 dB

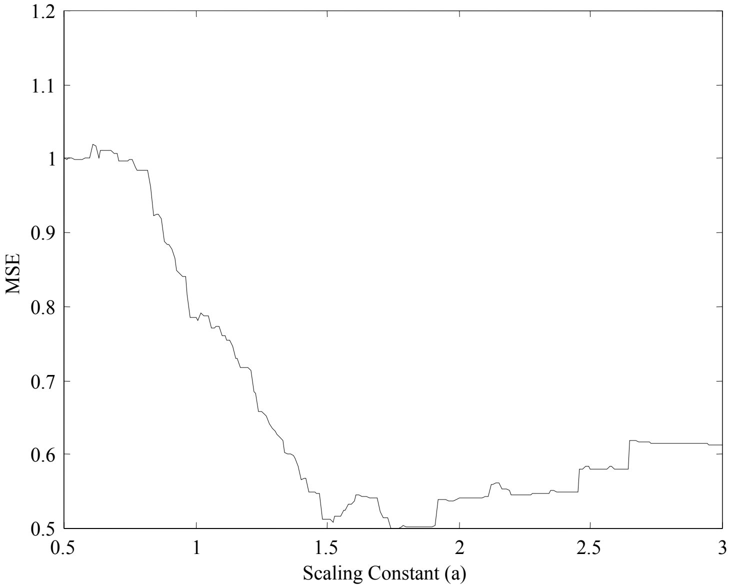

Figure B-18. MSE between NLS Channel Output and Colored Unambiguous Output vs. Scaling Constant for Sampled LFM, *TB* = 127, Input P_u/P_a = -3.0 dB

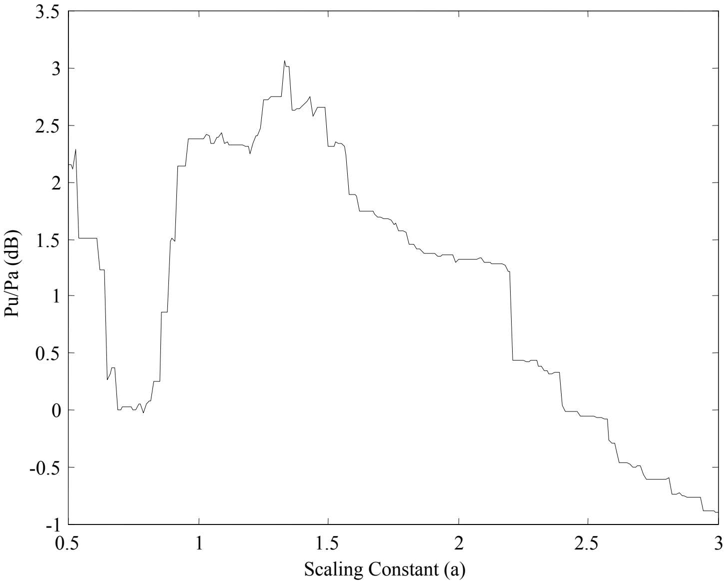

Figure B-19. Unambiguous/Ambiguous Output Power Ratio vs. Scaling Constant for 16-Phase SA Code, *TB* = 31, Input P_u/P_a = -3.0 dB

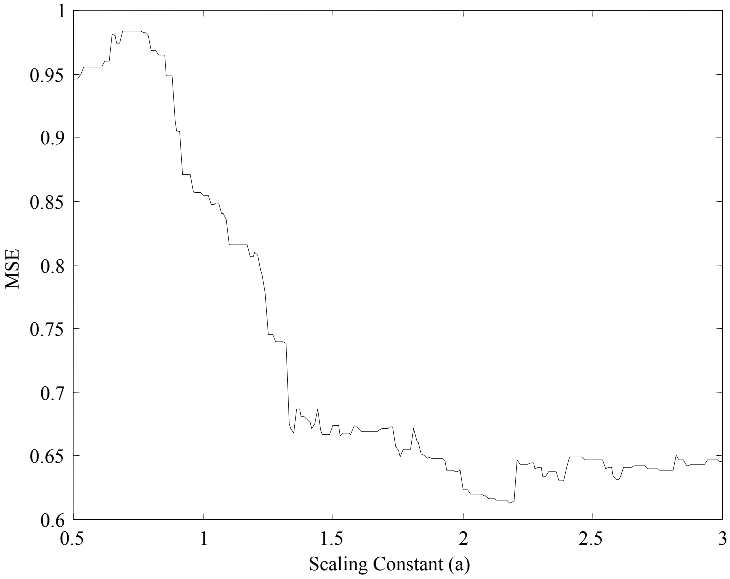

Figure B-20. MSE between NLS Channel Output and Colored Unambiguous Output vs. Scaling Constant for 16-Phase SA Code, *TB* = 31, Input P_u/P_a = -3.0 dB

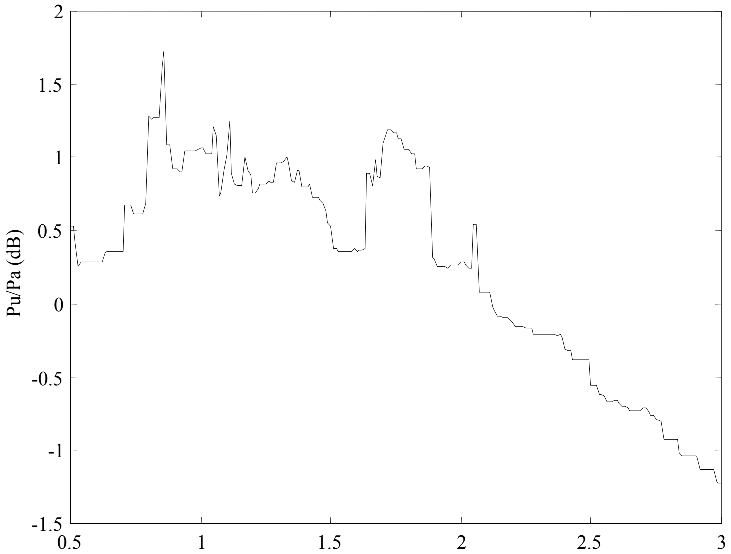

Figure B-21. Unambiguous/Ambiguous Output Power Ratio vs. Scaling Constant for 16-Phase SA Code, *TB* = 63, Input P_u/P_a = -3.0 dB

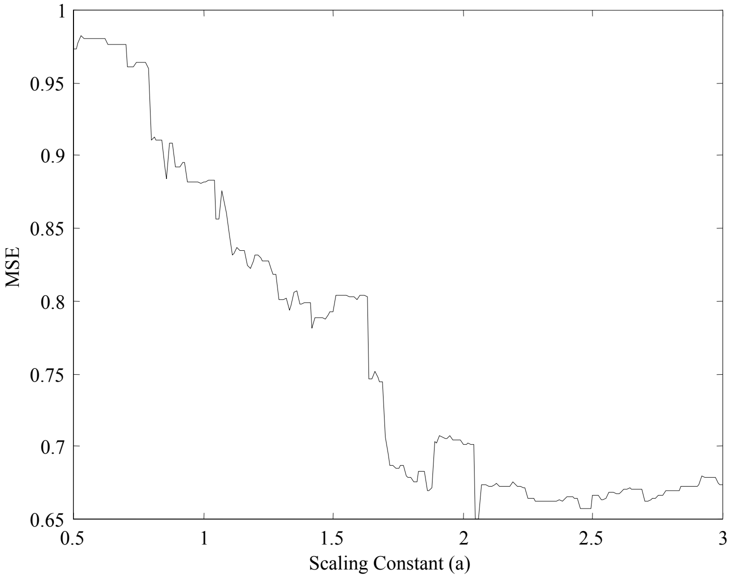

Figure B-22. MSE between NLS Channel Output and Colored Unambiguous Output vs. Scaling Constant for 16-Phase SA Code, *TB* = 63, Input P_u/P_a = -3.0 dB

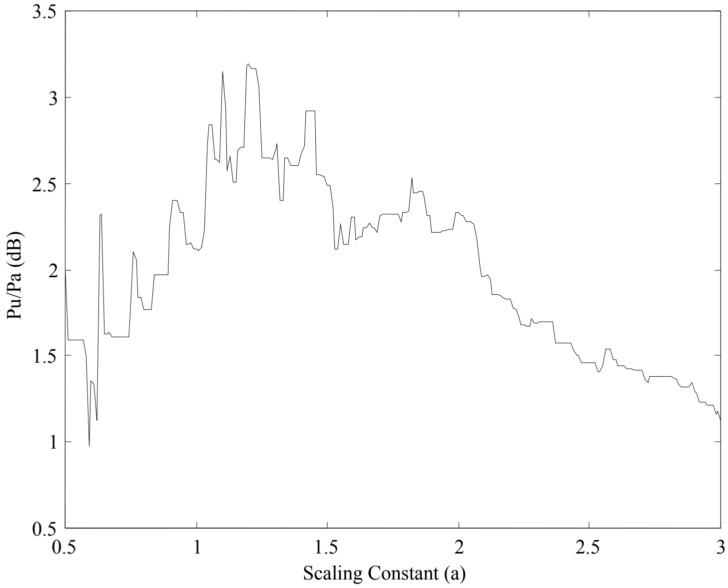

Figure B-23. Unambiguous/Ambiguous Output Power Ratio vs. Scaling Constant for 16-Phase SA Code, $TB = 127$, Input $P_u/P_a = -3.0$ dB

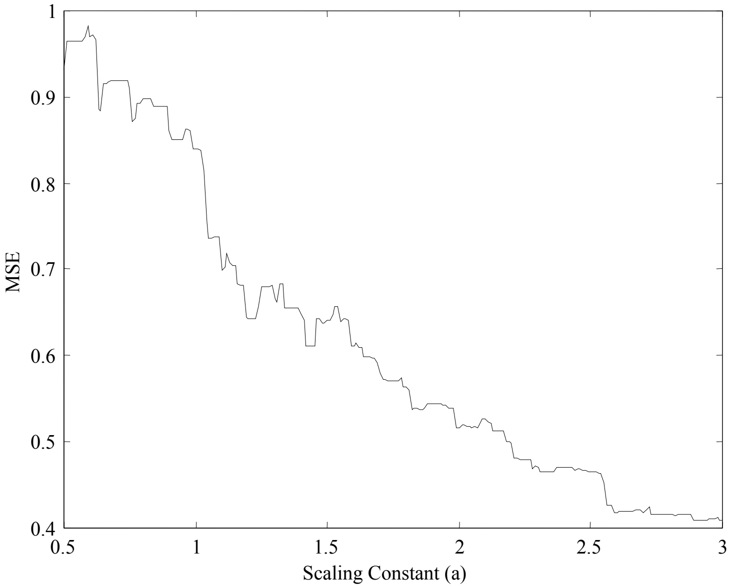

Figure B-24. MSE between NLS Channel Output and Colored Unambiguous Output vs. Scaling Constant for 16-Phase SA Code, $TB = 127$, Input $P_u/P_a = -3.0$ dB

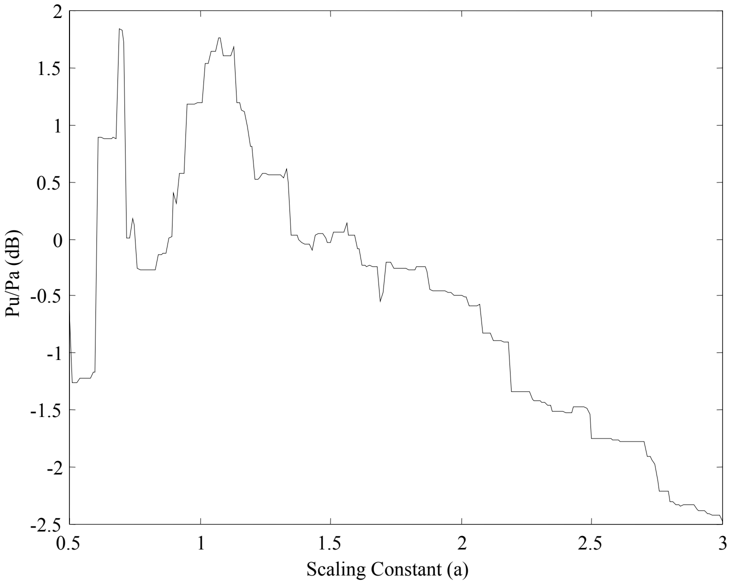

Figure B-25. Unambiguous/Ambiguous Output Power Ratio vs. Scaling Constant for Sampled LFM, TB = 31, Input P_u/P_a = -6.0 dB

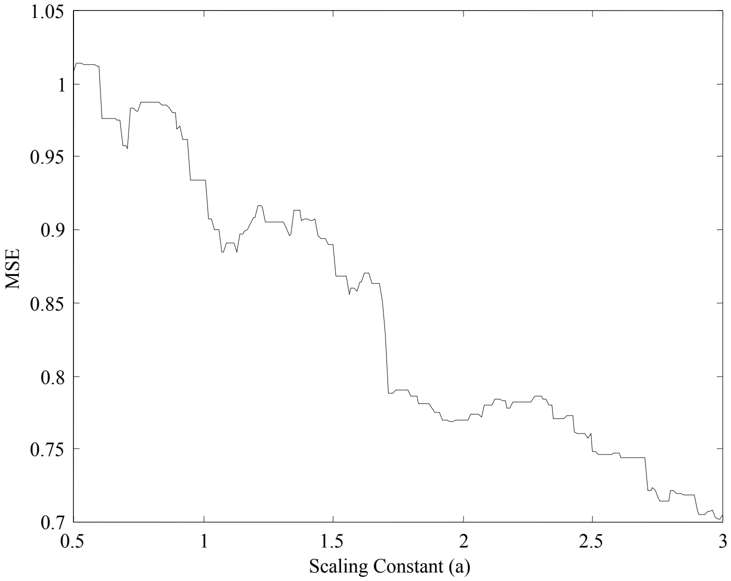

Figure B-26. MSE between NLS Channel Output and Colored Unambiguous Output vs. Scaling Constant for Sampled LFM, TB = 31, Input P_u/P_a = -6.0 dB

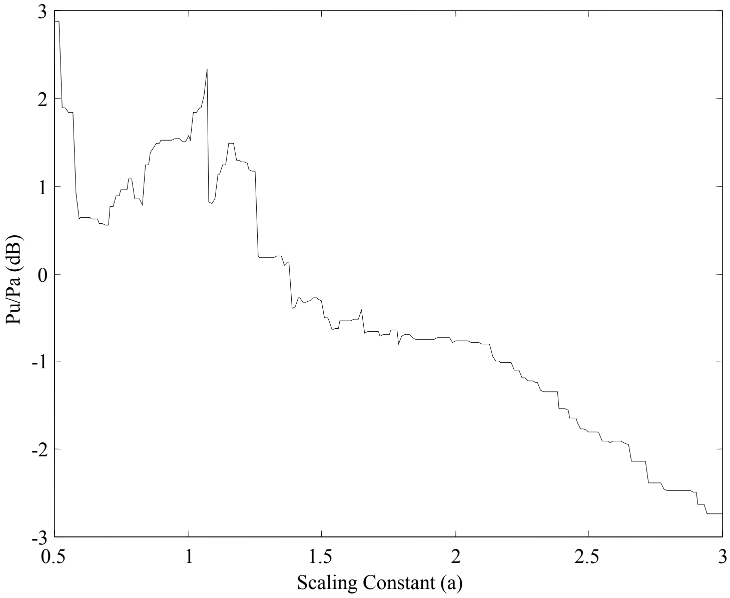

Figure B-27. Unambiguous/Ambiguous Output Power Ratio vs. Scaling Constant for Sampled LFM, TB = 63, Input P_u/P_a = -6.0 dB

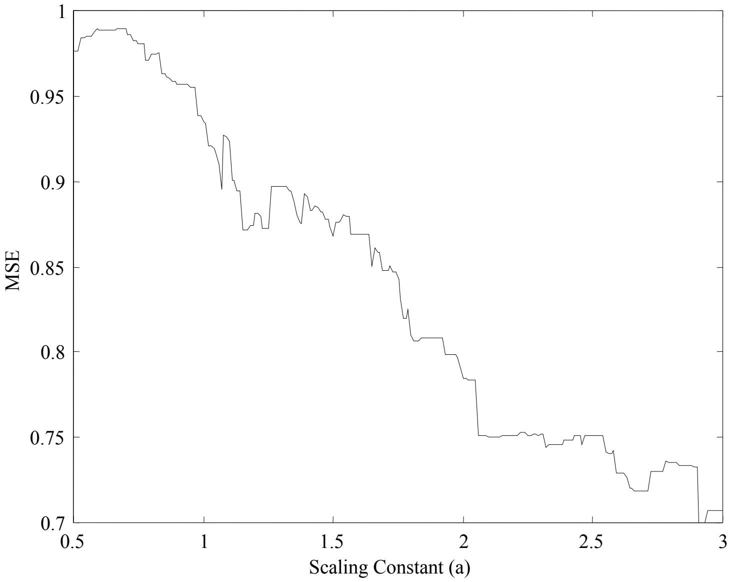

Figure B-28. MSE between NLS Channel Output and Colored Unambiguous Output vs. Scaling Constant for Sampled LFM, TB = 63, Input P_u/P_a = -6.0 dB

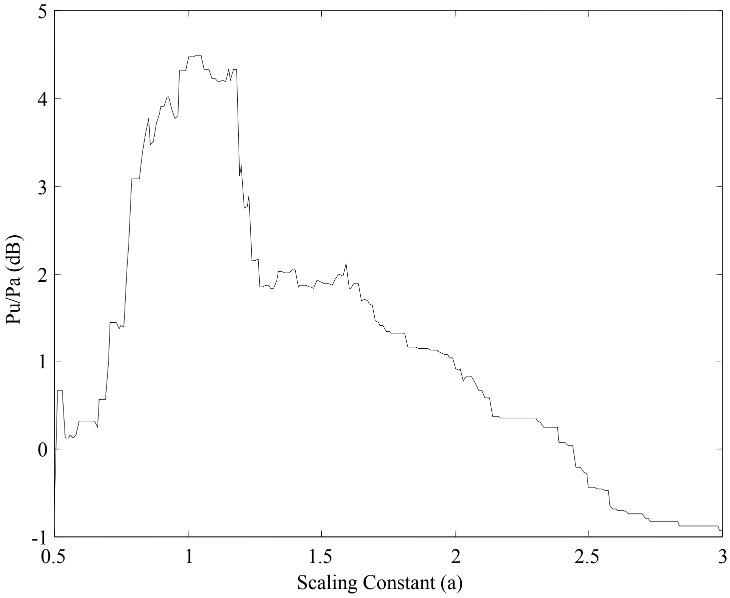

Figure B-29. Unambiguous/Ambiguous Output Power Ratio vs. Scaling Constant for Sampled LFM, *TB* = 127, Input P_u/P_a = -6.0 dB

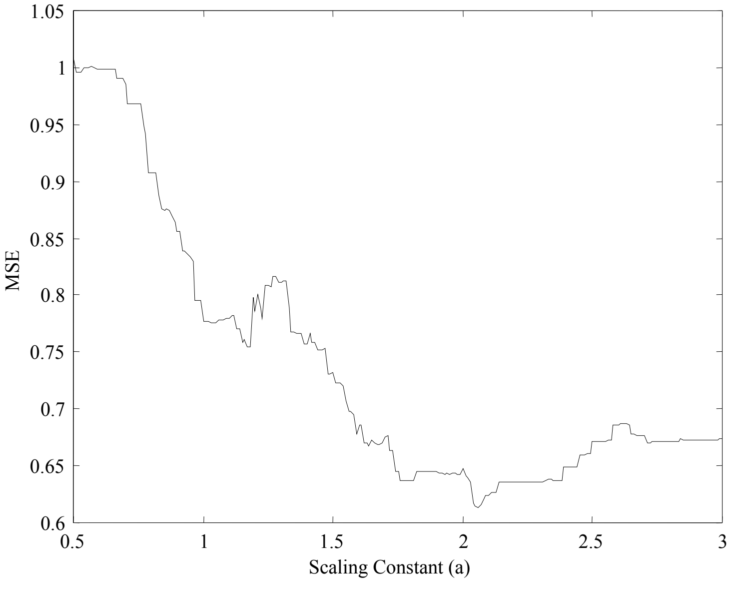

Figure B-30. MSE between NLS Channel Output and Colored Unambiguous Output vs. Scaling Constant for Sampled LFM, *TB* = 127, Input P_u/P_a = -6.0 dB

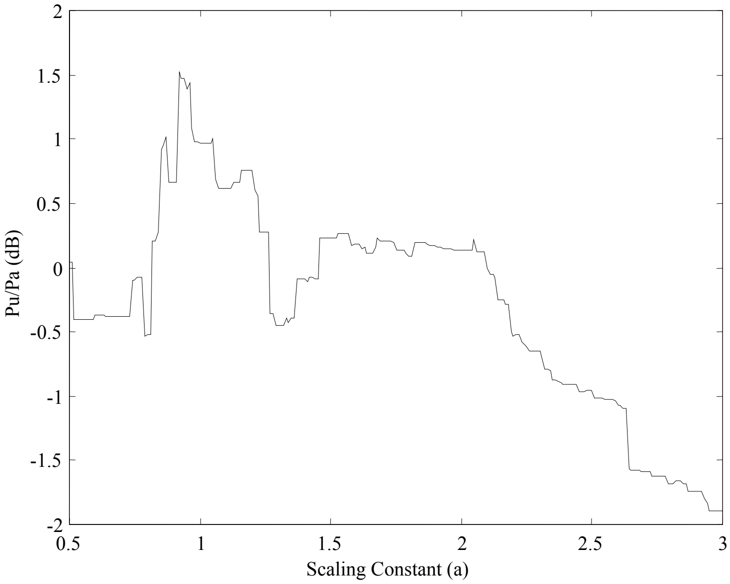

Figure B-31. Unambiguous/Ambiguous Output Power Ratio vs. Scaling Constant for 16-Phase SA Code, *TB* = 31, Input P_u/P_a = -6.0 dB

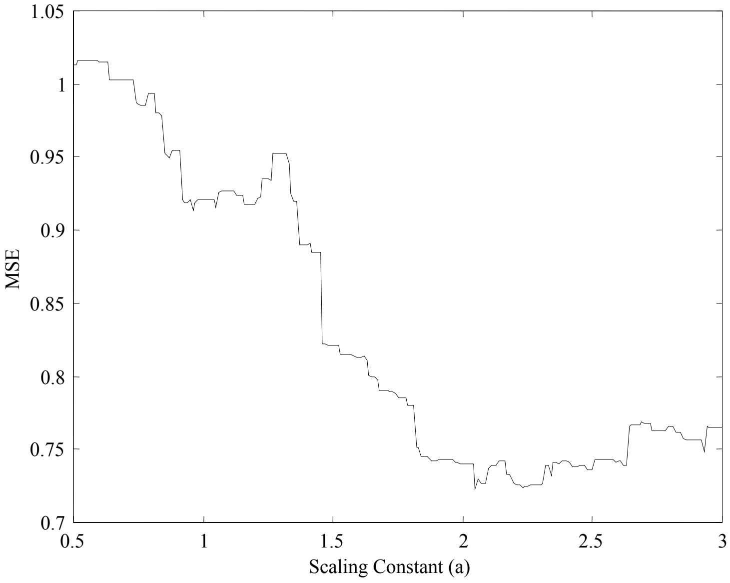

Figure B-32. MSE between NLS Channel Output and Colored Unambiguous Output vs. Scaling Constant for 16-Phase SA Code, *TB* = 31, Input P_u/P_a = -6.0 dB

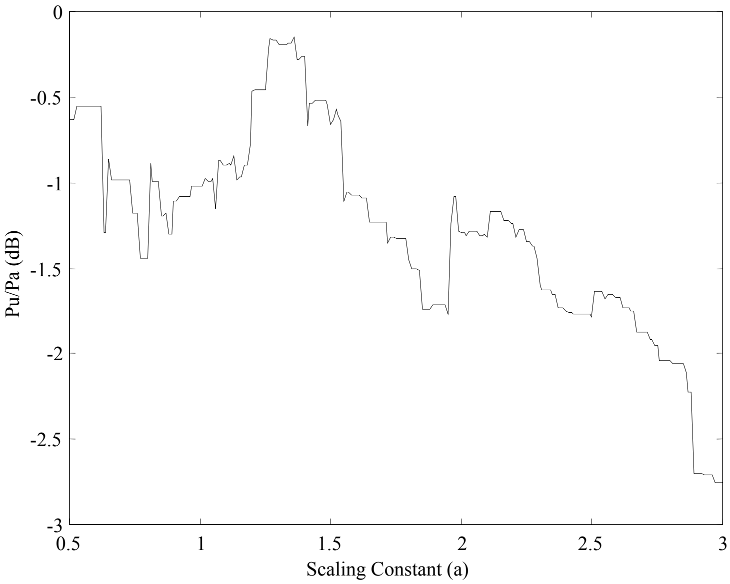

Figure B-33. Unambiguous/Ambiguous Output Power Ratio vs. Scaling Constant for 16-Phase SA Code, *TB* = 63, Input P_u/P_a = -6.0 dB

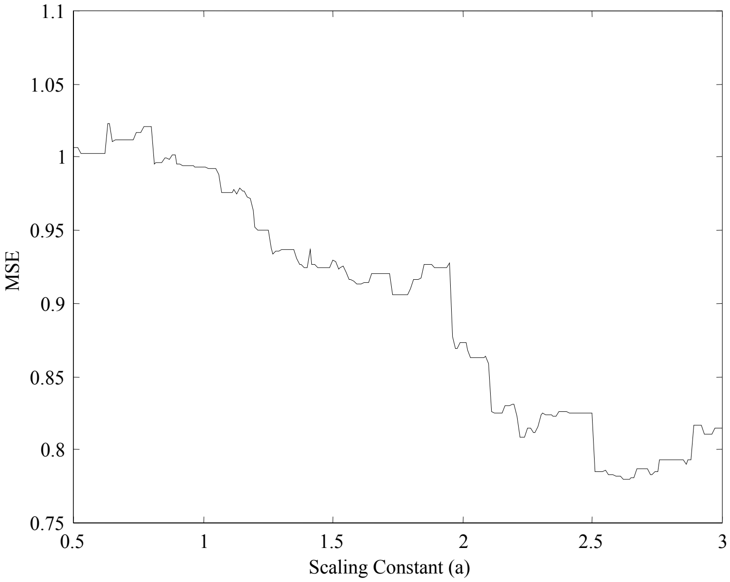

Figure B-34. MSE between NLS Channel Output and Colored Unambiguous Output vs. Scaling Constant for 16-Phase SA Code, *TB* = 63, Input P_u/P_a = -6.0 dB

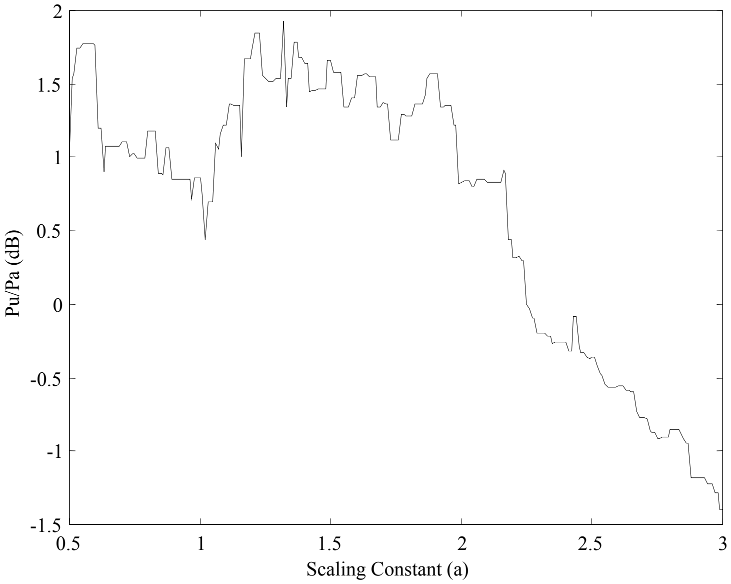

Figure B-35. Unambiguous/Ambiguous Output Power Ratio vs. Scaling Constant for 16-Phase SA Code, *TB* = 127, Input P_u/P_a = -6.0 dB

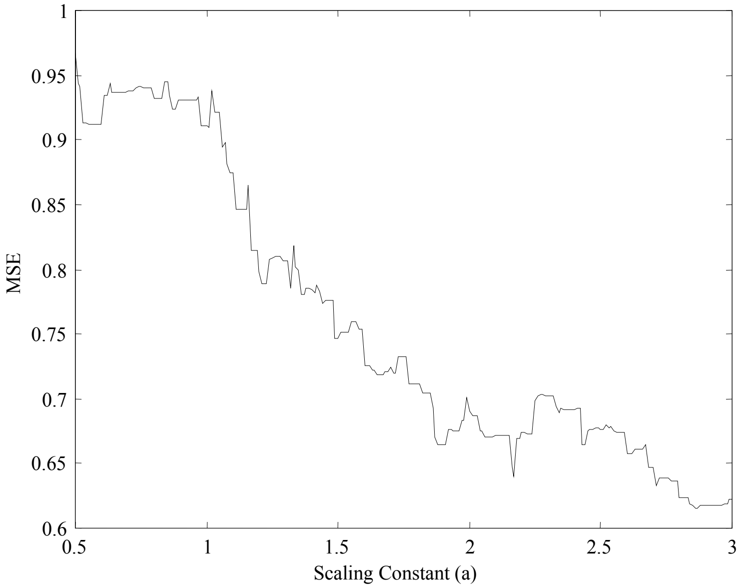

Figure B-36. MSE between NLS Channel Output and Colored Unambiguous Output vs. Scaling Constant for 16-Phase SA Code, *TB* = 127, Input P_u/P_a = -6.0 dB

Bibliography

1. Barton, D.K., *Modern Radar System Analysis*, Artech House, 1988.

2. Morris, G., Harkness, L., *Airborne Pulsed Doppler Radar*, 2nd Edition, Artech House, 1996.

3. Skolnik, M.L., *Introduction to Radar Systems*, 2nd Edition, McGraw-Hill, 1980.

4. Brown, W.M., Palermo, C.J*., Random Processes, Communications, and Radar*, McGraw-Hill, 1969.

5. Betz, J.W., Sousa, M.J., *Inverting a Partial Ambiguity Function*, MITRE Technical Report MTR96B0000012, May 1996.

6. Hlawatsch, F., *Time-Frequency Analysis and Synthesis of Linear Signal Spaces*, Kluwer Academic Publishers, 1998.

7. Wilson, K.S., *Effects of Clutter Height Distribution on Adaptive Clutter Erasure Performance*, PhD Dissertation, AFIT/DS/ENG/98-05, Air Force Institute of Technology (AU), Wright-Patterson AFB OH, June 1998.

8 . Skolnik, M., *Radar Handbook*, 2nd Ed., New York: McGraw-Hill, 1990.

9. Lei, W., Long, T., Han, W., *Resolution of Range and Velocity Ambiguity for a Medium Pulse Doppler Radar*, Record of the IEEE 2000 International Radar Conference, IEEE AESS, 2000.

10. Sachidananda, M., Zrnic, D., *Systematic Phase Codes for Resolving Range Overlaid Signals in a Doppler Weather Radar*, Journal of Atmospheric and Oceanic Technology, Vol 16, October 1999.

11. Palermo, Leith, and Horgen, *Ambiguity Suppression By Nonlinear Processing*, Eighth Annual Radar Symposium Record, June 1962.

12. Anderson, J.M., Temple, M.A., Brown, W.M., and Crossley, B.L., "A Nonlinear Suppression Technique for Range Ambiguity Resolution in Pulse Doppler Radars," *Proceedings of the 2001 IEEE Radar Conference, Atlanta, Georgia*, May 2001, pp 141-146.

13. Golay, M.J., "Complementary Series," *IRE Transactions on Information Theory, 7*: 82-87 (April 1961).

14. Sivaswamy, R., "Self-Clutter Cancellation and Ambiguity Properties of Subcomplementary Sequences," *IEEE Transactions on Aerospace and Electronic Systems, 18*(2): 163-181 (March 1982).

15. Zeoli, G.W., "Comment on 'Self-Clutter Cancellation and Ambiguity Properties of Subcomplementary Sequences'," *IEEE Transactions on Aerospace and Electronic Systems, 19*(5): 780-781 (September 1983).

16. Kretschmer, F.E., and Gerlach, K., "Low Sidelobe Radar Waveforms Derived From Orthogonal Matrices," *IEEE Transactions on Aerospace and Electronic Systems, 27*(1): 92-101 (January 1991).

17. Gerlach, K., and Kretschmer, F.E., "General Forms and Properties of Zero Cross-Correlation Radar Waveforms," *IEEE Transactions on Aerospace and Electronic Systems, 28*(1): 98-103 (January 1992).

18. Guey, J., and Bell, M.R., "Diversity Waveform Sets for Delay-Doppler Imaging," *IEEE Transactions on Information Theory, 44*(4): 1504-1522 (July 1998).

19. Peterson, R.L., Ziemer, R.E., and Borth, D.E., *Introduction to Spread Spectrum Communications*, Englewood Cliffs, NJ: Prentice Hall, 1995.

20. Rihaczek, A.W., *Principles of High-Resolution Radar*, New York: McGraw-Hill, 1969.

21. Anderson, J.M., Temple, M.A., and Oxley, M.E., "Nonlinear Suppression of Range Ambiguities in Pulse-Diverse Radar," *IEE Electronic Letters, 37*(20): 1252-1253 (27 Sept 2001).

22. Nathanson, F.E., *Radar Design Principles*, Mendham, NJ: SciTech, 1999.

23. Oppenheim, A.V., and Willsky, A.S., *Signals and Systems*, 2nd Ed., Upper Saddle River, NJ: Prentice Hall, 1997.

24. Klauder, J.R., Price, A.C., Darlington, S., and Albersheim, W.J., "The Theory and Design of Chirp Radars," *The Bell System Technical Journal, XXXIX* (4): 745-809 (July 1960).

25. Cook, C.E., and Bernfeld, M., *Radar Signals: An Introduction to Theory and Application*, Orlando: Academic Press, 1967.

26. Cook, C.E., "Pulse Compression – Key to More Efficient Radar Transmission," *Proceedings of the IRE, IRE 48* (3): 310-316 (March 1960).

27. Coxson, G.E., Hirschel, A., and Cohen, M.N., "New Results on Minimum-PSL Binary Codes," *Proceedings of the 2001 IEEE Radar Conference*, Atlanta, GA, May 2001, pp. 153-156.

28. Sarwate, D.V., and Pursley, M.B., "Crosscorrelation Properties of Pseudorandom and Related Sequences," *Proc. IEEE*, Vol. 68, pp. 593-619, May 1980.

29. Mow, W.H., and Li, S.Y.R., "Aperiodic Autocorrelation and Crosscorrelation of Polyphase Sequences," *IEEE Transactions on Information Theor*y, *IT-43* (3): 1000-1007, (May 1997).

30. Welch, L.R., "Lower Bounds on the Maximum Cross Correlation of Signals," *IEEE Transactions on Information Theor*y, *IT-20*: 397-399, (May 1974).

31. Sarwate, D.V., "Bounds on Crosscorrelation and Autocorrelation of Sequences," *IEEE Transactions on Information Theory, IT-25* (6): 720-724 (November 1979).

32. Griep, K.R., Ritcey, J.A., and Burlingame, J.J., "Poly-Phase Codes and Optimal Filters for Multiple User Ranging," *IEEE Transactions on Aerospace and Electronic Systems, AES-31* (2): 751-767 (April 1995).

33. Deng, H., "Synthesis of Binary Sequences with Good Autocorrelation and Crosscorrelation Properties by Simulated Annealing," *IEEE Transactions on Aerospace and Electronic Systems, AES-32* (1): 98-107 (January 1996).

34. El Gamal, A.A., Hemachandra, L.A., Shperling, I., and Wei, V.K., “Using Simulated Annealing to Design Good Codes,” *IEEE Transactions on Information Theory, IT-33* (1): 116-123 (January 1987).

35. Sahr, J.D., and Grannan, E.R., “Simulated Annealing Searches For Long Binary Phase Codes With Application to Remote Sensing*,” Radio Science, 28* (5): 1053-1055 (November-December 1993).

36. Kirkpatrick, S., Gelatt, C.D., and Vecchi, M.P., “Optimization by Simulated Annealing,” *Science, 220* (4598): 671-680 (13 May 1983).

37. Press, W.H., Teukolsky, S.A., Vetterling, W.T., and Flannery, B.P., *Numerical Recipes in C*, Cambridge, U.K.: Cambridge University Press, 1992.

38. Brown, W.M., “Mutually Dispersive Codes for Nonlinear Suppression of Ambiguities,” Unpublished Correspondence, September 2001.

39. Ulaby, F.T., and Dobson, M.C., *Radar Scattering Statistics for Terrain*, Boston: Artech House, 1989.

40. Ayasli, S., “Propagation Effects On Radar Ground Clutter,” *Proceedings of the 1986 IEEE National Radar Conference*, Los Angeles, CA, March12-13, 1986, p. 127.

41. Long, M.W., *Radar Reflectivity of Land and Sea*, Boston: Artech House, 2001.

42. Smith, B.G., “Geometric Shadowing of a Random Rough Surface,” *IEEE Transactions on Antennas and Propagation*, *AP-15*(5): 668-671 (September 1967).

43. Sloper, D., Fenner, D., Arntz, J., and Fogle, E., *Final Technical Report: Multi-Channel Airborne Radar Measurement (MCARM), MCARM Flight Test, Vol 1*, Rome Laboratory, AFMC, RL-TR-96-49.

44. Mahafza, B.R., *Radar Systems Analysis and Design Using MATLAB*, Boca Raton: Chapman & Hall/CRC, 2000.

45. Lewis, B.L., Kretschmer, F.F., and Shelton, W.W., *Aspects of Radar Signal Processing*, Norwood, MA: Artech House, 1986.

46. Turin, G.L., “An Introduction to Matched Filters,” *IRE Transactions on Information Theory*, IT-6: 353-371 (June 1960).

REPORT DOCUMENTATION PAGE	*Form Approved* *OMB No. 0704-0188*

1. AGENCY USE ONLY *(Leave blank)*	**2. REPORT DATE** December 2001	**3. REPORT TYPE AND DATES COVERED** PhD Dissertation

4. TITLE AND SUBTITLE NONLINEAR SUPPRESSION OF RANGE AMBIGUITY IN PULSE DOPPLER RADAR	**5. FUNDING NUMBERS** EN
6. AUTHOR(S) Jon M. Anderson, Major, USAF	
7. PERFORMING ORGANIZATION NAME(S) AND ADDRESS(ES) Air Force Institute of Technology Graduate School of Engineering and Management 2950 P Street, Building 640 WPAFB OH 45433-7765	**8. PERFORMING ORGANIZATION REPORT NUMBER** AFIT/DS/ENG/01-05
9. SPONSORING/MONITORING AGENCY NAME(S) AND ADDRESS(ES) AFRL/SN Attn: Dr. William M. Brown WPAFB OH 45433	**10. SPONSORING/MONITORING AGENCY REPORT NUMBER**

11. SUPPLEMENTARY NOTES

Dr. Michael Temple, ENG, DSN: 785-3636, ext. 4703

12a. DISTRIBUTION AVAILABILITY STATEMENT APPROVED FOR PUBLIC RELEASE; DISTRIBUTION UNLIMITED	**12b. DISTRIBUTION CODE**

13. ABSTRACT *(Maximum 200 words)*

Coherent pulse train processing is most commonly used in airborne pulse Doppler radar, achieving adequate transmitter/receiver isolation and excellent resolution properties while inherently inducing ambiguities in Doppler and range. First introduced by Palermo in 1962 using two conjugate LFM pulses, the primary nonlinear suppression (NLS) objective involves reducing range ambiguity, given the waveform is nominally unambiguous in Doppler, by using interpulse and intrapulse coding (pulse compression) to discriminate received ambiguous pulse responses. By introducing a nonlinear operation on compressed (undesired) pulse responses within individual channels, ambiguous energy levels are reduced in channel outputs. This research expands the NLS concept using discrete coding and processing. A general theory is developed showing how NLS accomplishes ambiguity surface volume removal without requiring orthogonal coding. Useful NLS code sets are generated using combinatorial, simulated annealing optimization techniques - a general algorithm is developed to extended family size, code length, and number of phases (polyphase coding). An adaptive reserved code thresholding scheme is introduced to efficiently and effectively track the matched filter response of a target field over a wide dynamic range, such as normally experienced in airborne radar systems. An evaluation model for characterizing NLS clutter suppression performance is developed - NLS performance is characterized using measured clutter data with analysis indicating the proposed technique performs relatively well even when large clutter cells exist.

14. SUBJECT TERMS Radar, Pulse Compression, Radar Waveforms, Nonlinear Signal Processing, Radar Signal Processing, Radar Coding	**15. NUMBER OF PAGES** 146
	16. PRICE CODE

17. SECURITY CLASSIFICATION OF REPORT UNCLASSIFIED	**18. SECURITY CLASSIFICATION OF THIS PAGE** UNCLASSIFIED	**19. SECURITY CLASSIFICATION OF ABSTRACT** UNCLASSIFIED	**20. LIMITATION OF ABSTRACT** UL